ALMA MATER STUDIOURUM UNIVERSITÀ DI BOLOGNA

FACOLTÀ DI SCIENZE MATEMATICHE, FISICHE E NATURALI
DIPARTIMENTO DI ASTRONOMIA

A HIGH ENERGY PERSPECTIVE OF THE CO-EVOLUTION OF BLACK HOLES AND THEIR HOST GALAXIES

TESI DI DOTTORATO
DI
FRANCESCA MARIA CIVANO

RELATORE: **PROF. G. PALUMBO**

CO-RELATORE: **DR. A. COMASTRI**

COORDINATORE: **PROF. L. MOSCARDINI**

SCUOLA DI DOTTORATO IN SCIENZE MATEMATICHE, FISICHE E ASTRONOMICHE
DOTTORATO DI RICERCA IN ASTRONOMIA, XIX CICLO (2003–2006)

SETTORE SCIENTIFICO DISCIPLINARE: AREA 02 - SCIENZE FISICHE
FIS/05 ASTRONOMIA E ASTROFISICA

*Alla mia Famiglia
e al mio piatto tibiale*

Contents

Executive summary

Thanks to the *Chandra* and XMM–*Newton* surveys, the hard X-ray sky is now probed down to a flux limit where the bulk of the X-ray background is almost completely resolved into discrete sources, at least in the 2–8 keV band. Extensive programs of multiwavelength follow-up observations showed that the large majority of hard X–ray selected sources are identified with Active Galactic Nuclei (AGN) spanning a broad range of redshifts, luminosities and optical properties. A sizable fraction of relatively luminous X-ray sources hosting an active, presumably obscured, nucleus would not have been easily recognized as such on the basis of optical observations because characterized by "peculiar" optical properties. In my PhD thesis, I will focus the attention on the nature of two classes of hard X-ray selected "elusive" sources: those characterized by high X-ray-to-optical flux ratios and red optical-to-near-infrared colors, a fraction of which associated with Type 2 quasars, and the X-ray bright optically normal galaxies, also known as *XBONGs*. In order to characterize the properties of these classes of elusive AGN, the datasets of several deep and large-area surveys have been fully exploited.

The first class of "elusive" sources is characterized by X-ray-to-optical flux ratios (X/O) significantly higher than what is generally observed from unobscured quasars and Seyfert galaxies. The properties of well defined samples of high X/O sources detected at bright X–ray fluxes suggest that X/O selection is highly efficient in sampling high–redshift obscured quasars. At the limits of deep *Chandra* surveys ($\sim 10^{-16}$ erg cm^{-2} s^{-1}), high X/O sources are generally characterized by extremely faint optical magnitudes, hence their spectroscopic identification is hardly feasible even with the largest telescopes. In this framework, a detailed investigation of their X-ray properties may provide useful information on the nature of this important component of the X-ray source population. The X-ray data of the deepest X-ray observations ever performed, the *Chandra* deep fields, allows us to characterize the average X-ray properties of the high X/O population. The results of spectral analysis clearly indicate that the high X/O sources represent the most obscured component of the X–ray background. Their spectra are harder ($\Gamma \sim 1$)

1

than any other class of sources in the deep fields and also of the XRB spectrum ($\Gamma \approx 1.4$).

In order to better understand the AGN physics and evolution, a much better knowledge of the redshift, luminosity and spectral energy distributions (SEDs) of elusive AGN is of paramount importance. The recent COSMOS survey provides the necessary multiwavelength database to characterize the SEDs of a statistically robust sample of obscured sources. The combination of high X/O and red-colors offers a powerful tool to select obscured luminous objects at high redshift. A large sample of X-ray emitting extremely red objects ($R - K$ >5) has been collected and their optical-infrared properties have been studied. In particular, using an appropriate SED fitting procedure, the nuclear and the host galaxy components have been deconvolved over a large range of wavelengths and ptical nuclear extinctions, black hole masses and Eddington ratios have been estimated. It is important to remark that the combination of hard X-ray selection and extreme red colors is highly efficient in picking up highly obscured, luminous sources at high redshift.

Although the *XBONGs* do not present a new source population, the interest on the nature of these sources has gained a renewed attention after the discovery of several examples from recent *Chandra* and XMM–*Newton* surveys. Even though several possibilities were proposed in recent literature to explain why a relatively luminous ($L_X = 10^{42} - 10^{43} erg\ s^{-1}$) hard X-ray source does not leave any significant signature of its presence in terms of optical emission lines, the very nature of *XBONGs* is still subject of debate. Good-quality photometric near-infrared data (ISAAC/VLT) of 4 low-redshift *XBONGs* from the HELLAS2XMM survey have been used to search for the presence of the putative nucleus, applying the surface-brightness decomposition technique. In two out of the four sources, the presence of a nuclear weak component hosted by a bright galaxy has been revealed. The results indicate that moderate amounts of gas and dust, covering a large solid angle (possibly 4π) at the nuclear source, may explain the lack of optical emission lines. A weak nucleus not able to produce suffcient UV photons may provide an alternative or additional explanation. On the basis of an admittedly small sample, we conclude that *XBONGs* constitute a mixed bag rather than a new source population. When the presence of a nucleus is revealed, it turns out to be mildly absorbed and hosted by a bright galaxy.

Chapter 1

Introduction

T he detailed study of the nature of the X–ray source population is being pursued by complementing deep pencil–beam observations with shallower, larger area surveys. Over the last few years, multiwavelength follow–up observations of X–ray sources have been performed to characterize their optical to radio properties. A broad diversity of source types is found: at variance with optically selected quasars, X-ray selected AGN are characterized by a much larger spread in their optical properties. A sizable fraction of relatively luminous X–ray sources hosting an active, presumably obscured nucleus would not have been easily recognized as such on the basis of optical observations (the so called "elusive" AGN) either because associated with very faint counterparts or due to the lack of AGN emission features in their optical spectra.

1.1   The joint evolution of SMBHs and their host galaxies

It is now widely accepted that supermassive black holes (SMBH, $M_{BH} > 10^6$ $M_\odot$) reside at the centers of most, if not all, nearby galaxies (Kormendy & Richstone, 1995; Richstone et al. 1998; Kormendy & Gebhardt 2001). Moreover, observations show that the mass of the central black hole (BH) is tightly correlated both with the luminosity (Magorrian et al. 1998; McLure & Dunlop 2002; Marconi & Hunt 2003) and with the velocity dispersion (i.e., the M_{BH}-σ relation; Ferrarese & Merrit 2000; Gebhardt et al. 2000; Tremaine et al. 2002) of spheroids.

These observational evidences support the direct link between the origin and evolution of SMBHs and their host galaxies. The ubiquity of supermassive BHs in galaxies suggest that most or all galaxies experienced the AGN phase during their cosmic history. Following the "cosmic cycle" proposed by Hopkins et al. (2006), the formation of spheroids and the growth of SMBHs represent connected phases in the galaxy life. At high redshift, mergers between galaxies rich of gas drive nuclear inflows, triggering

starbursts and fueling the growth of central BHs. During most of this phase, quasar activity is obscured by large amount of gas and dust. When the central BH dominates the source energetics, quasar feedback expels gas and dust, making the nuclear source visible, probably for a short period, as a bright quasar. Eventually, as the gas is further heated and expelled, quasar activity can no longer be maintained and the system relaxes to a spheroid with a quiescent SMBH. The remnant will then evolve passively and would be available as seed to repeat this "cosmic cycle". The physics behind all these process is still not clear, however numerical simulation and semi-analitical models support the scenario described above (e.g., Menci et al. 2004; Di Matteo et al. 2005).

An observational approach to understand the coupling of galaxies and SMBHs is to trace the history of the observed correlations, measuring the growth rates of BHs and stellar bulges at earlier epochs. In order to constrain the M_{BH}-L_{bulge} relation at high redshift, both quantities have to be measured independently.

At present, the only class of objects for which it is possible to estimate BH masses at high redshift, with the reverberation mapping technique, is that of Type 1 AGN although with large uncertainties (Vestergaard 2002, 2006), while similar approach cannot be used for obscured AGN, which are known to be more numerous (see Section 1.2).

The host galaxy luminosity is harder to measure but in the last few years substantial progresses have been made in separating the nuclear from the host galaxy component in Type 1 AGN thanks to the HST capabilities, using either non-parametric PSF subtraction or 2-dimensional modeling (Peng et al. 2002; Jahnke et al. 2004; Sanchez et al. 2004; Peng et al. 2006). In Type 2 AGN, the bulge component dominates over the nuclear light and its luminosity should be easier to measure.

Even if several attempts have been performed, it is very challenging to measure high redshift BH masses, mostly of Type 2 AGN, and host galaxy luminosity independently; indeed, the behaviour of the M_{BH}-luminosity relation is still matter of debate. Several authors have found significant evolution of this relation (Woo et al. 2006; Peng et al. 2006), while other authors found marginal or no evolution up to z∼ 2 (Shields et al. 2006; Hopkins et al. 2006).

To trace back the growth and the evolution of the SMBHs needs a detailed census and characterization of AGN activity, especially for the obscured ones. The X-ray band is by far the cleanest one for studying the accretion onto BHs in the Universe at high redshift in the quasar phase (obscured and unobscured). It is the only band in which the emission due to the accretion processes clearly dominates the background cosmic radiation and moreover it is relatively insensitive to obscuration, at least at high energies.

1.2 The X-ray background

The X-ray background (XRB) was serendipitously discovered by Giacconi and his collaborators (Giacconi et al. 1962), during the first successful rocket flight launched
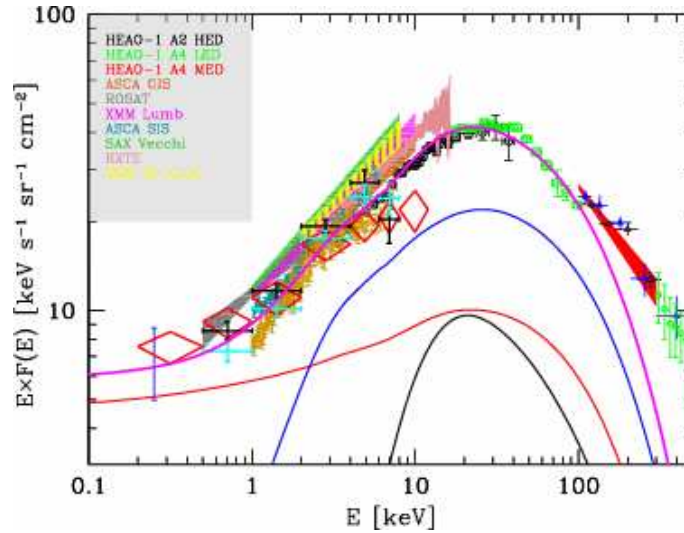
Figure 1.1: The cosmic XRB spectrum and predicted contribution from the population of Compton-thin and Compton-thick AGN. The different XRB measurements are explained on the top left: different instruments on board HEAO-1 (Gruber 1992, Gruber et al. 1999); ASCA GIS (Kushino et al. 2002); ROSAT PSPC (Georgantopoulos et al. 1996); two different measurements by XMM (Lumb et al. 2002, De Luca & Molendi 2004); ASCA SIS (Gendreau et al. 1995); BeppoSAX (Vecchi et al. 1999); RXTE (Revnivtsev et al. 2003). At $E > 100$ keV, the plotted data points are from HEAO-1 A4 MED (red triangles: Gruber 1992, Gruber et al. 1999; shaded area: Kinzer et al. 1997); balloon experiments (blue triangles, Fukada et al. 1975); SMM (green circles, Watanabe et al. 1997). The blue errorbar at 0.25 keV is from shadowing experiments by Warwick & Roberts (1998). Also shown are the XRB fractions resolved by Worsley et al. (2005) in the Lockman Hole (red diamonds), CDFS (cyan crosses) and CDFN (black crosses). The resolved fraction in the CDFS as measured by Tozzi et al. (2001a) is also shown (gold datapoints). Solid lines refer to the contribution of different AGN classes according to the model m2 from Gilli et al. (2007). Unobscured AGN, obscured Compton-thin and Compton-thick AGN, total AGN plus galaxy cluster are shown with a red, blue, black and magenta curve, respectively.

to study the X-ray emission from the Moon. The lack of any correlation with the Galactic latitude, and a dipole anisotropy consistent with that of the dipole component of the Cosmic Microwave Background, strongly argued, since the beginning, for a cosmological origin of this extragalactic background radiation.

Since the discovery, a great deal of efforts has been made to understand the nature of the XRB. Although the spectrum of the XRB resembles, in the 3–60 keV energy range, that of a hot plasma ($kT \sim 40$ keV; Marshall et al. 1980), the possibility that a hot IGM is responsible for the XRB has been discarded since the hot gas should produce detectable high-frequency distortions in the cosmic microwave background radiation (CMB) through inverse-Compton scattering, which have not been observed by the COBE satellite (Mather et al. 1990). As a consequence, the only alternative is that the XRB is due to superposition of extragalactic discrete sources.

After more than 40 years since its discovery, it is by now clear that the cosmic XRB is mostly produced by the integrated emission of obscured and unobscured Active Galactic Nuclei (AGN). The summed contributions of the sources detected in the deepest X-ray surveys account for virtually the entire XRB emission around a few keV and for about
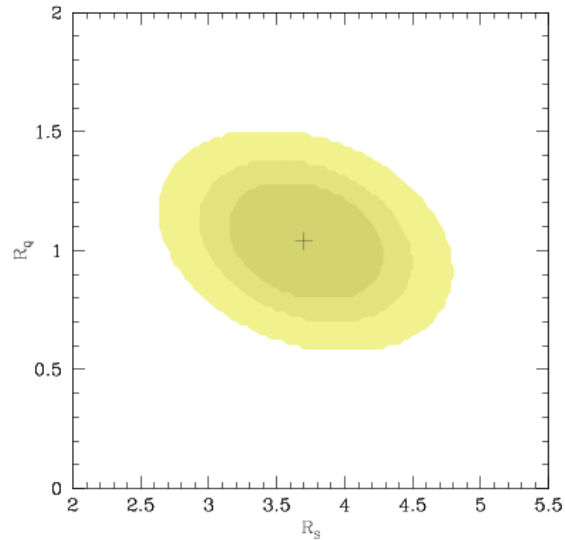
Figure 1.2: The 68,90,99% confidence contours on the best fit R_S and R_Q ratios computed for two interesting parameters ($\Delta\chi^2 = 2.3, 4.61, 9.21$, respectively) in the "m2" model of Gilli et al. (2007). R_S is the ratio between obscured Compton-thin AGN and unobscured AGN (i.e. the number ratio between sources with $21 < logN_H < 24$ and with $logN_H < 21$) in the Seyfert luminosity regime, while R_Q is the ratio in the QSO luminosity regime (from Gilli et al. 2007).

half of that at higher (7-10 keV) energies (Worsley et al. 2005). The exact fraction depends on the absolute XRB flux normalization which is still affected by rather large uncertainties.

For this reason, the XRB intensity measurement is a matter of great interest. A compilation of XRB measurements in different energy bands is shown in Fig. 1.1 (from Gilli et al. 2007). The only broad-band (3-100 keV) measurement of the XRB spectrum has been performed by the HEAO1-A2 experiment (Marshall et al. 1980) and has the lowest normalization. More recent values, obtained below 10 keV with imaging instruments, were found to be always higher, the highest one having been measured by BeppoSAX (Vecchi et al. 1999). The most recent determinations by RXTE (Revnivtsev et al. 2003), XMM–*Newton* (Lumb et al. 2002; De Luca & Molendi 2004) and *Chandra* (Hickox & Markevitch 2006), as well as a re-analysis of the HEAO1-A2 data (Revnivtsev et al. 2005), have been found to lay in between the original HEAO1- A2 measurement and the BeppoSAX one, comparable to those obtained a few years ago by ASCA (Gendreau et al. 1995; Kushino et al. 2002).

Having established that the XRB is due to the emission of extragalactic sources, several models were proposed to explain its shape. The model proposed by Setti & Woltjer (1989) was the first able to solve the so-called "spectral paradox", i.e. the discrepancy between the slope of the XRB spectrum ($\Gamma=1.4$) and that of bright AGN ($\Gamma=1.7$–1.9; Nandra & Pounds 1994) and is by now widely accepted as the explanation of the XRB spectrum. They showed that, within the AGN Unified Model (Antonucci 1993), the flat

power-law spectral index of the XRB is due to a superposition of spectra with different amount of obscuring matter. Following this indication, several authors have developed and refined population synthesis models in order to reproduce not only the spectral shape and the intesity of the XRB but also other observational constraints such as the number counts, the redshift and the absorption distributions (Madau et al. 1994; Comastri et al. 1995, 2001; Gilli et al. 2001, 2007). In Figure 1.1, the contribution of unobscured (red), obscured Compton-thin ($N_H = 10^{21}$ - 10^{24} cm^{-2}, blue), Compton-thick AGN ($N_H > 10^{24}$ cm^{-2}, black) and total AGN plus galaxy clusters ($\sim 7\%$, magenta), expected by the Gilli et al. (2007) model, are reported. The authors show that the best-fit model includes a different evolution for obscured and unobscured sources. They conclude that the ratio between moderately obscured and unobscured AGN is found to decrease from about 4 at $\log L_x \lesssim 42$ to about 1 at $\log L_x \gtrsim 45$ (Fig. 1.2) and that, although the fraction of obscured AGN is found to decrease with luminosity, a non-negligible population of obscured QSOs is still required.

Since the origin of the XRB emission is now understood, many efforts are currently dedicated to a better understanding of the AGN populations, whose cosmic accretion history is recorded into the XRB spectrum. In particular, subjects of intense research activity are the demography and the evolution of the XRB sources, with the aim to test the models of formation and joint evolution of BHs and host galaxies (see previous Section).

In order to properly address all these topics, the most efficient approach is to combine deep pencil-beam and shallower X-ray surveys over much larger sky areas with multiwavelength follow-up observations, to collect statistically significant samples of objects as a function of luminosity, redshift and obscuration. Moreover, high-resolution optical/near-infrared images are needed to study the properties of the host galaxies.

1.3 Extragalactic Surveys

Since their launch, the two cornerstone X-ray satellites, the NASA's Chandra X-ray observatory (*Chandra*) and the ESA's X-ray Multi-Mirror Newton (XMM–*Newton*), are surveying the X-ray sky over a wide range of fluxes and solid angles. Deep surveys are able to unveil intrinsically less luminous and/or obscured objects than wide-field surveys that, on the contrary, are not biased against rare objects. The combination of both deep and shallow surveys is necessary for a complete census of the X-ray background sources in the 0.5–10 keV range. Multiwavelength (from radio frequencies to UV) follow-up observations of serendipitously detected X-ray sources are crucial to understand the properties of the observed objects. Redshifts and luminosities are provided by spectroscopic identification campaigns, which constitute some of the most expensive and time consuming observational follow-ups. A list of recent and ongoing *Chandra* and XMM–*Newton* X-ray surveys is available at the web site
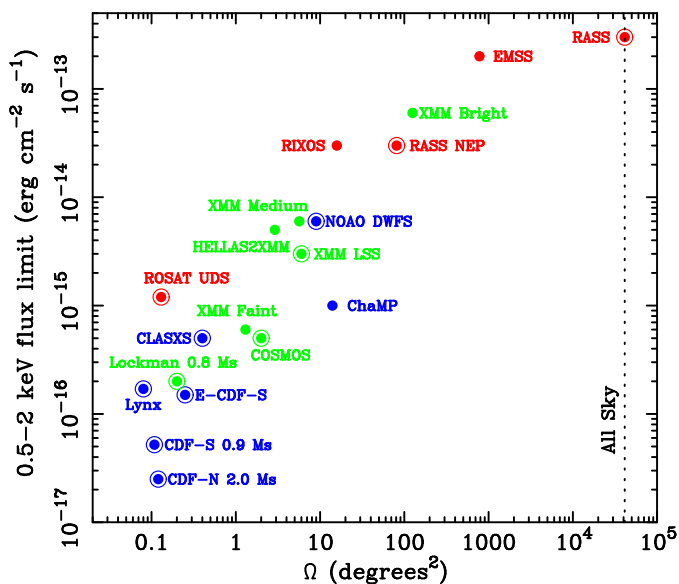
Figure 1.3: Distribution of some well-known extragalactic surveys performed by *Chandra* (blue) and XMM–*Newton* (green) and earlier mission (magenta) in the 0.5-2 keV flux limit versus solid angle plane. Circled dotes denote surveys that are contiguous. The vertical dashed line shows the solid angle of the whole sky (from Brandt & Hasinger 2005).

http://cxc.harvard.edu/xraysurveys/. In Figure 1.3 a compilation of surveys is reported as function of the flux limit (in the soft band) and the covered area. In the following, I will focus the attention on four different hard X-ray surveys whose data I have used during my PhD: the two deepest *Chandra* X-ray surveys ever performed and two shallower large-area XMM–*Newton* X-ray surveys.

1.3.1 The Chandra Deep Fields

The *Chandra* Deep Fields (the *Chandra* Deep Field North and the *Chandra* Deep Field South, hereafter *CDFN* and *CDFS*) are two of the most studied fields in X-ray astronomy, because of the very low Galactic absorbing column densities in their directions (N_H(Gal)=1.6×10^{20}cm^{-2} and N_H(Gal)$\sim 8 \times 10^{19}$cm^{-2}, respectively; Stark et al. 1992).

The *CDFN* (Alexander et al. 2003) is centered in one of the most studied region of the sky, the Hubble Deep Field North. This is the deepest 0.5-8.0 keV survey ever made, and nearly 550 X-ray sources have been detected. The survey is made of 20 individual exposure of the Chandra ACIS-I instruments, for a total exposure time of 2 Megaseconds. The covered area is almost 450 sq. arcmin. The limiting flux is $\sim 2.5 \times 10^{-17}$ erg cm^{-2} s^{-1} in the soft band (0.5-2 keV) and $\sim 1.4 \times 10^{-16}$ erg cm^{-2} s^{-1} in the hard band (0.5-8 keV).

The *CDFS* (Giacconi et al. 2002) is the result of the co-addition of 11 individual ACIS-I exposures for a total of 1 Megasecond over an area of almost 400 sq. arcmin. The limiting flux is $\sim 5.5 \times 10^{-17}$ erg cm^{-2} s^{-1} in the soft band (0.5-2 keV) and

Figure 1.4: The composite 2 Ms image of the *Chandra* Deep Field North. The image was obtained combining three energy bands 0.5-2 keV (red), 2-4 keV (green), 4-8 keV (blue; Alexander et al. 2003). The dimension of the figure is $\approx 24 \times 24$ arcmin.
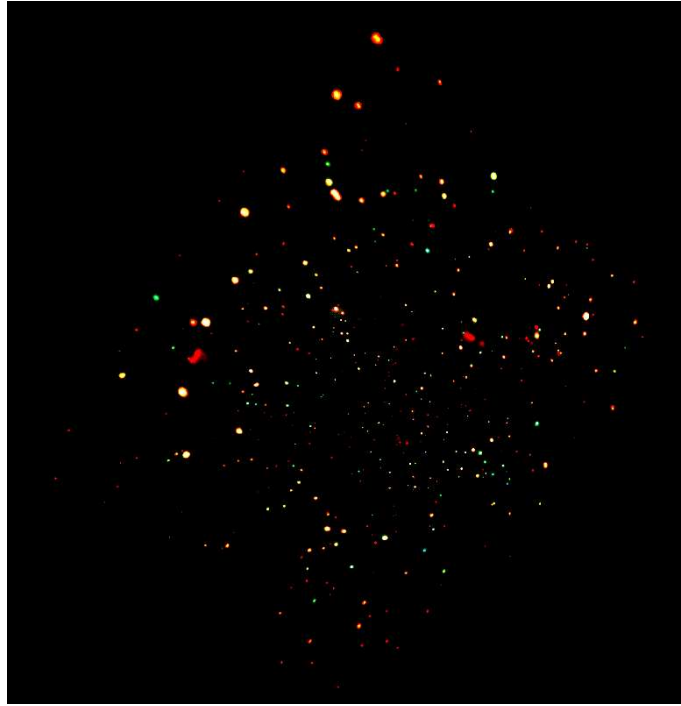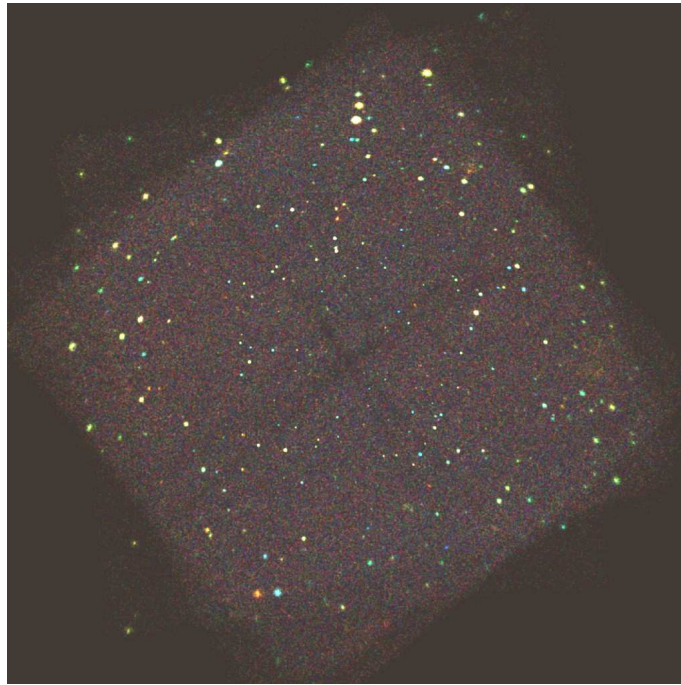

Figure 1.5: The composite 1 Ms image of the *Chandra* Deep Field South. The image was obtained combining three energy bands 0.3-1 keV (red), 1-2 keV (green), 2-7 keV (blue; Rosati et al. 2001). The dimension of the figure is $\approx 24 \times 24$ arcmin.

(a) *CDFN*

(b) *CDFS*

(c) HELLAS2XMM

(d) XMM-COSMOS
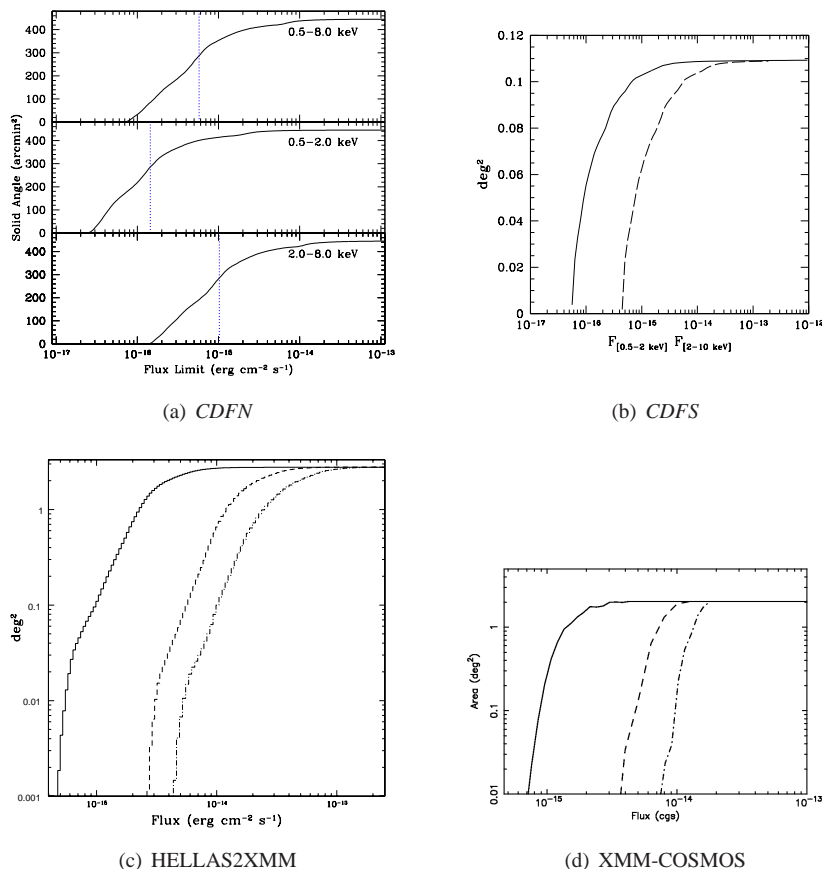
Figure 1.6: a: Solid angle versus flux limit (S/N= 3) for the full (top), soft (middle), and hard (bottom) bands. The vertical dotted lines indicate the flux limits for an area of ≈ 285 arcmin^2, equivalent to a single ACIS-I field of view (Alexander et al. 2003); b: The sky coverage for the soft-band image (solid line) and the hard-band image (dashed line; Giacconi et al. 2001); c: The total sky coverage of the survey in the 0.5-2 keV (solid line), 2-10 keV (dashed line) and 4.5-10 keV band (dot-dashed line; Baldi et al. 2002); d: The sky coverage vs. flux relation in the 0.5-2, 2-10 and 5-10 keV energy bands (continuous, dashed and dash-dotted lines, respectively; Cappelluti et al. 2007).

4.5×10^{-16} erg cm^{-2} s^{-1} in the hard band (2-7 keV). A total of $\sim$350 sources have been detected.

  The true color images of the deep fields are presented in Fig. 1.4 and 1.5. The sky coverage (covered area vs. flux limit) plots of the CDFs and of the surveys described below in the main bands are reported in Fig. 1.6 in order to compare their flux limits and the surveyed area.

1.3.2   The HELLAS2XMM survey

The XMM–*Newton* High Energy Large Area Survey (hereafter HELLAS2XMM) has been originally conceived as the natural extension of the *BeppoSAX* HELLAS[1] survey

---

[1]High Energy Large Area Survey: a very hard (5-10 keV) shallow ($\gtrsim 10^{-13}$ erg cm^{-2} s^{-1}) survey covering several tens of deg^2 of the sky (see, i.e., Vignali 2001, PhD thesis).
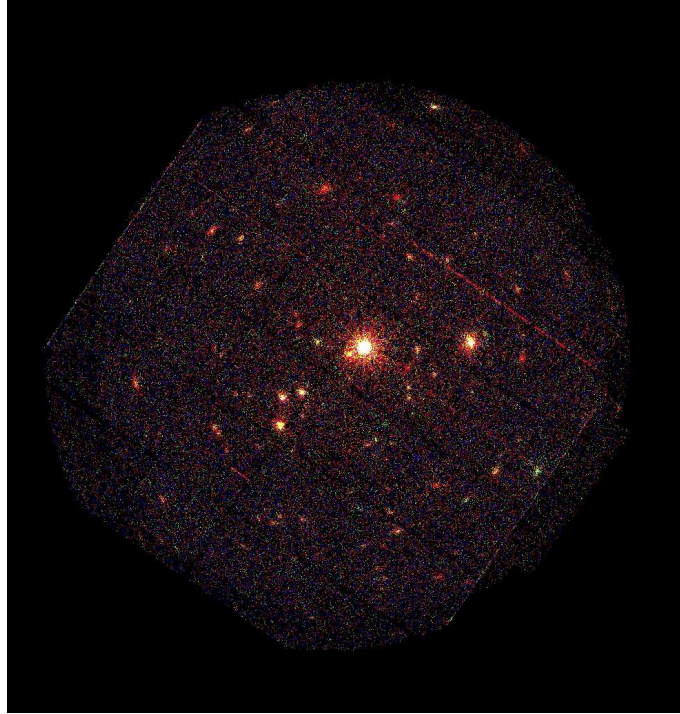
Figure 1.7: (The image of the PKS 0312-77 field, belonging to the HELLAS2XMM. The image has been accumulated in three different energy bands 0.5-2 keV (red), 2-4 keV (green), 4-8 keV (blue); courtesy of C. Vignali. The dimension of the figure is $\approx 30 \times 30$ arcmin.

to the XMM–*Newton* capabilities, in order to fully exploit the larger throughput, effective area and better spectral and angular resolution. At present, the HELLAS2XMM survey sample is made by 232 X-ray sources detected over 10 XMM–*Newton* fields ($\sim$1.4 square degrees) at fluxes in the range of $10^{-15} - 10^{-13}$ erg cm^{-2} s^{-1}. Optical counterparts have been found for 214 sources (Fiore et al. 2003; Cocchia et al. 2007). Medium-deep optical and near-infrared photometry, along with high signal-to-noise optical spectra and *Spitzer* coverage have been obtained for most of the objects. The HELLAS2XMM complement the deep *Chandra* fields by sampling brighter fluxes over a larger area. The analysis and interpretation of the multiwavelength observations (radio, infrared, optical and X-ray) is presented in several papers (Comastri et al. 2002; Brusa et al. 2003; Mignoli et al. 2004; Perola et al. 2004; La Franca et al. 2005; Maiolino et al. 2006; Pozzi et al. 2007). The image of the best studied field of this survey (around the bright quasar PKS 0312-77) is shown in Fig. 1.7. The sky coverage of the whole survey (Baldi et al. 2002) is presented in Fig. 1.6.

1.3.3 The COSMOS survey

The Cosmic Evolution Survey (COSMOS; Scoville et al. 2007) is based on a "Treasury project" of HST that observed a contiguous 2 square degrees area with ACS, bounded by $9^h57.5^m <$R.A.$< 10^h03.5^m$; $1^d27.5^m <$DEC$< 2^d57.5^m$. A comprehensive
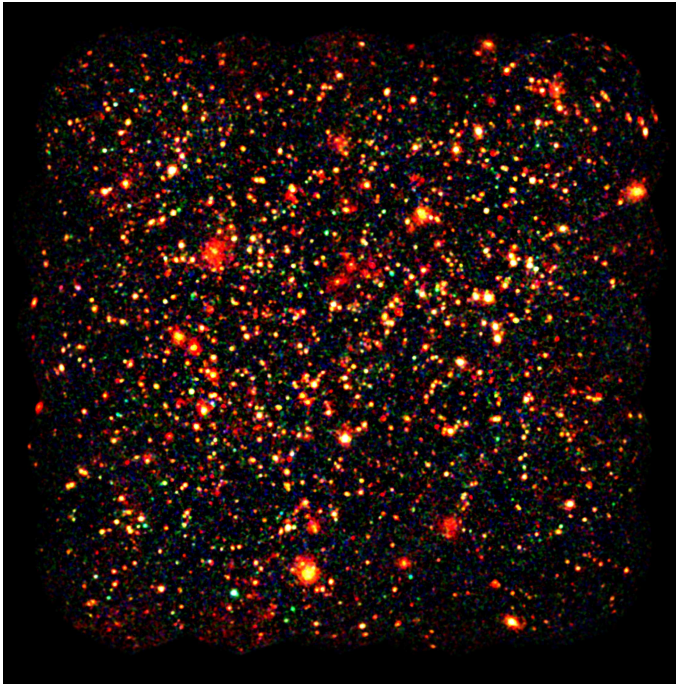
Figure 1.8: The composite image of the XMM-COSMOS survey (first 23 fields). For each of the first 23 individual pointings, the images have been accumulated in three different energy bands: 0.5-2 keV (red), 2-4.5 keV (green) and 4.5-10 keV (blue), then combined into a mosaic (Hasinger et al. 2007). The dimension of the figure is $\approx$ 2×2 deg.

multiwavelength program is underway to observe the COSMOS field with current (VLA, *Spitzer*, Subaru, Galex, XMM–*Newton*) and future (ALMA) observatories from the radio to the X-ray and is complemented by a dedicated redshift survey carried on with the VIMOS/VLT (Lilly et al. 2007) and IMACS/Magellan (Impey et al. 2007) instruments. The strength of the COSMOS survey is the unprecedented combination of a large solid angle and sensitivity over a broad-band frequency range. The high-resolution images allow measurements of galaxy morphologies and relate these to the large-scale structure, probing the evolution of the galaxies in the Universe and the co-evolution with their active nuclei. Once completed, the database of the COSMOS survey will be unique in the observational cosmology scenario to study the evolution of the Universe in the redshift range z=0.5-4.

The **XMM-COSMOS** survey (Hasinger et al. 2007) provides the coverage of all the COSMOS field in the 0.5-10 keV band with the XMM–*Newton* X-ray telescope (see Fig. 1.8). The main scientific goals are to study the AGN source population at 0.5-2 keV fluxes larger than 10^{-15}erg cm^{-2} s^{-1}, in particular the properties of X-ray selected AGN as a function of the environment and the properties of X-ray selected clusters and groups. The field has been covered by 25 pointings repeated twice, each of about 30 ksec, for a total exposure of 1.4 Msec. The sky coverage of the survey in the 0.5-2, 2-10 and 5-10 keV energy bands is presented in Fig. 1.6. The results obtained using the first half of the

observations are reported in several papers in press in a dedicated ApJ Supplement issue and available at the website http://www.mpe.mpg.de/XMMCosmos/PAPERS. Recently, the COSMOS field has been awarded 1.8 Ms of *Chandra* time, the largest *Chandra* program ever approved. The **Chandra-COSMOS** project (PI: M. Elvis) will cover the inner area (0.7 deg^2) of the field to 200 ksec depth. The *Chandra* survey will reach 4-5 times deeper fluxes than XMM-COSMOS in both soft and hard band. The dense tiling strategy will produce a uniform sensitivity and maximize the high-resolution area to resolve sources with a sub-arcsecond position accuracy.

1.4 The content of X-ray surveys

A broad diversity of source types is found in deep and shallow surveys. Extensive programs of multiwavelength follow-up observations showed that the majority of the hard X-ray selected sources are identified with AGN spanning a broad range of redshifts and luminosities. At variance with optically selected quasars, X-ray selected AGN are characterized by a much larger spread in their optical properties.

It is well known that various classes of X-ray emitters are characterized by different values of the X-ray-to-optical flux ratio (hereinafter X/O) and the observed X/O could provide a first, rough indication of the source classification (Maccacaro et al. 1988). The X/O is defined as

$$X/O = \log \frac{f_X}{f_R} = \log f_X + C + \frac{R}{2.5} \qquad (1.1)$$

where f_X is the X-ray flux (erg cm^{-2} s^{-1}) in a given energy range, f_R is the R-band flux computed by converting the R-band magnitudes into monochromatic fluxes (at λ=6500Å) and then multiplying them by the width of the R filter (Zombeck 1990), C is a constant which depends on the specific filter used in the optical observations. The majority of spectroscopically identified AGN in previous soft surveys (ROSAT, Hasinger et al. 1998, Lehman et al. 2001; ASCA, Akiyama et al. 2000) are characterized by $-1 < X/O < 1$. The optical identification of the 50-70% of the sources revealed in deep and medium surveys confirms this trend to fainter fluxes but shows also a very large scatter around the median value mostly in the hard band (Fig. 1.9). It is interesting to note that over three decades of X-ray flux, the hard X-ray sources, plotted in Fig. 1.9, span up to 5 decade of optical flux, hence of optical properties.

The various source types detected in X-ray surveys can be roughly divided using the X/O diagnostic as follows:

- $-1 < X/O < 1$: These values are typical for optically bright unobscured quasars and Seyfert galaxies with broad emission lines superimposed on a blue continuum, therefore the easiest to be spectroscopically identified up to $z \simeq 5$, and for optically and X-ray selected Type 2 AGN at relative low redshift ($z < 1.5$).
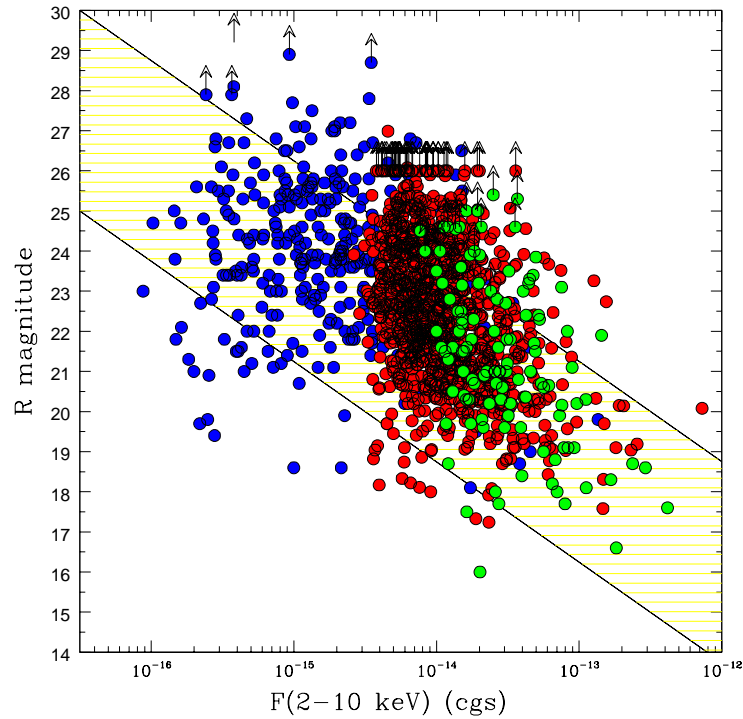
Figure 1.9: The R-band magnitude vs. the 2-10 keV flux for the hard source samples from HELLAS2XMM (green), XMM-COSMOS (red), *CDFN* and *CDFS* (blue). The dashed area represents the locus occupied by known AGN (e.g. quasars, Seyferts, emission-line galaxies) along the correlation $\log(f_X/f_R) = X/O = 0 \pm 1$ (courtesy of M. Brusa).

- $X/O > 1$: Relatively bright X-ray sources with optically faint counterparts lie in the upper part of the diagram; being characterized by optical faint magnitudes are thus unaccessible to optical spectroscopy; photometric redshifts place this sources at high redshift ($z > 1$). This class of sources will be extensively discussed in Chapters 2 and 3.

- $X/O < -1$: Starburst and normal galaxies at relatively low redshift ($z = 0.1 - 0.5$; Hornschemeier et al. 2003) emerge at the faintest X-ray soft fluxes mostly in the deep surveys. They constitute a significant fraction (up to 30%) of the source population detected in the soft band and thus less numerous in the hard band (see Fig. 1.9).

- $X/O \sim -1$: Most X-ray bright Optically Normal Galaxies, i.e., luminous X-ray sources without any signature of AGN activity in their optical spectrum (extensively discussed in Chapter 4).

1.4.1   High X-ray to optical flux ratio sources

The sources with high X/O values (> 1) are, on average, characterized by optically faint magnitudes, hence their spectroscopic classification is challenging, if not impossible. The fraction of high X/O in hard X-ray samples is about 20%, approximately constant over the entire range of X-ray fluxes sampled by deep and shallow surveys. Under the assumption that a high X/O ratio is a proxy of high redshift or high absorption or both, the study of the sources detected at relatively bright X-ray fluxes and bright optical magnitudes (R$\simeq$24) could give important constraints on the entire class. A well defined sample of high X/O sources detected in the *HELLAS2XMM* surveys at X-ray fluxes brighter than $\sim 10^{-14}$ erg cm^{-2} s^{-1} has been the subject of massive FORS/VLT optical spectroscopy (Fiore et al. 2003) and near-infrared K_s ISAAC/VLT photometry (Mignoli et al. 2004). The results clearly indicate that most of the targets are high-redshift ($z > 1$), luminous ($> 10^{44}$ erg s^{-1}) X-ray obscured (N$_H = 10^{22}$–10^{24} cm^{-2}) AGN (Perola et al. 2004). When the X-ray and multiwavelength properties of the faint tail of this class are considered (Alexander et al. 2001; Barger et al. 2003; Fiore et al. 2003; Mignoli et al. 2004; Civano et al. 2005; Mainieri et al. 2005; Pozzi et al. 2007), the findings at bright fluxes are confirmed. The X/O selection is thus highly efficient in sampling high-redshift, obscured quasars.

 A further argument which suggests that obscured accretion at high redshifts is a likely explanation of high X/O ratios, has been discussed by Comastri, Brusa and Mignoli (2003). Moving (Fig. 1.10) the spectral energy distribution (SED) of an X-ray absorbed AGN to progressively higher redshifts, the K-corrections in the optical and X-ray band work in the opposite direction. The shape of the hard X-ray spectrum is responsible for the strong positive K-correction which increases the X-ray flux and favours the detection of high-redshift sources. Conversely, the weak rest-frame UV emission is shifted in the R band and the observed faint magnitudes are mainly due to starlight in the host galaxies. The observed high values of the X/O are therefore at least qualitatively consistent with those expected for a population of high-redshift, absorbed AGN with X-ray column densities in the range N$_H = 10^{22}$-10^{24} cm^{-2}.

 Some extreme objects have no optical detections at all, even in deep optical images, and are termed EXOs (i.e., extremely X-ray objects; Koekemoer et al. 2004). A few objects have been detected in the *CDFN*, but a larger-area and medium-deep survey, as COSMOS, is the best suited for the search of these rare objects. EXOs can be plausibly explained as high-redshift AGN in dusty evolved hosts, and a minority of them may lie at $z > 7$, where the intragalactic medium absorbs essentially all of the observed-frame optical emission.

1.4.2   X-ray emitting EROs

Extremely Red Objects (EROs, $R - K > 5$, Elston et al. 1988) have the colors expected for high-redshift passive elliptical galaxies. They can be used as tracers of distant and old spheroids, in order to understand if the massive ellipticals in the local Universe formed
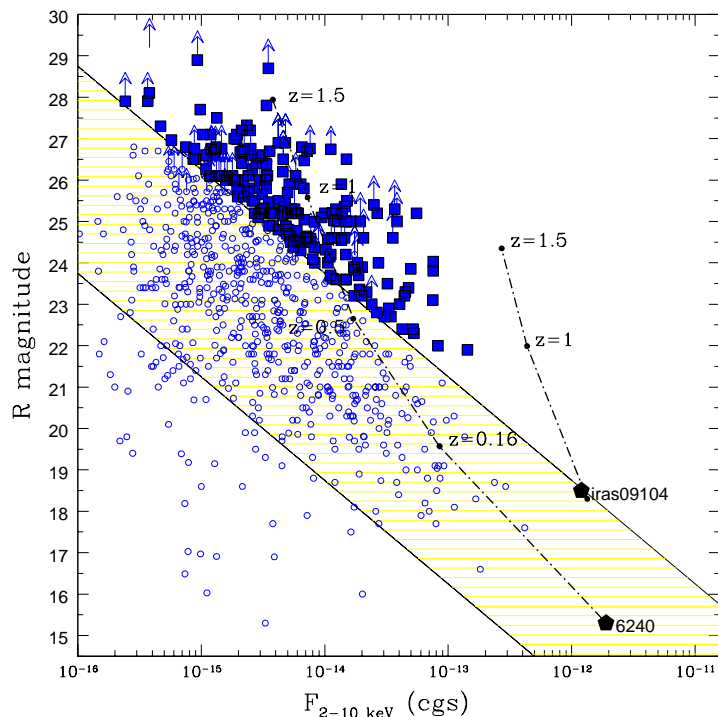
Figure 1.10: The 2-10 keV versus the R band magnitude for the hard X-ray sources detected in the HELLAS2XMM survey and in the *Chandra* deep fields. Filled squares represent high X/O sources. The dash-dotted lines represent the redshift tracks (from z=0 to z=1.5) computed for the SED of an absorbed object normalized to the observed X-ray flux and optical magnitude of NGC 6240 and IRAS 091104+4109, two well known Compton-thick objects (M. Brusa, PhD Thesis).

at early cosmological epochs through a relatively short episode of intense star formation or, conversely, if they built up more recently through hierarchical merging of pre-existing disk galaxies. However, several evidence have shown that EROs constitute a heterogenous class of extragalactic sources, therefore the understanding of the different subclasses is a key parameter in the study of the galaxy evolution and of the link between massive ellipticals and AGN activity (Menci et al. 2006). Some studies have shown that the ERO population is equally made by old passively evolving systems and dusty star-forming galaxies over the same redshift range (Cimatti et al. 2002). A significant fraction may also be constituted by AGN strongly reddened by dust extinction (Pierre et al. 2001; Mignoli et al. 2004; Maiolino et al. 2006). Other results suggested that the AGN population among EROs, although not dominant, share the same X-ray properties of high-luminosity, highly-obscured AGN at high redshift (Mainieri et al. 2002; Alexander et al. 2002; Brusa et al. 2005; Severgnini et al. 2005). Moreover, among the X-ray detected EROs, a significant fraction of sources show a high X/O. This confirms that a selection on the basis of the high X/O ratio is a powerful tool to detect highly-obscured quasars and is even stronger when coupled with the selection on the basis of extremely red colors (Brusa et al. 2005).

1.4.3 X-ray Bright Optically Normal Galaxies

This class of sources is variously termed as "optically-dull", "optically normal" or *XBONGs* (X-ray Bright Optically Normal Galaxies; Comastri et al. 2002). The common meaning of these definitions is that they lack evidence of accretion-driven activity in optical spectroscopy in contrast with "normal" Seyfert galaxies and quasars. The X-ray luminosities ($\approx 10^{42} - 10^{43}$ erg cm^{-2} s^{-1}), X-ray spectral shape and X/O ratio ~ -1 suggest AGN activity of moderate strength. Originally discovered in early *Einstein* observations (Elvis et al. 1981) and named optically dull galaxies, the interest on the nature of these sources has gained a renewed attention after the discovery of several examples in XMM-*Newton* and *Chandra* surveys (Fiore et al. 2000; Comastri et al. 2002a,b; Georgantopoulos et al. 2005; Kim et al. 2005). Several possibilities were proposed in the literature in order to explain why a relatively luminous, hard X-ray source does not leave any significant signature of its presence in the form of emission lines.

An appealing and simple explanation, put forward by Moran et al. (2002) for faint sources in the *Chandra* deep fields (see also Severgnini et al. 2003 for brighter nearby XMM–*Newton* sources), is dilution by the host galaxy starlight. The combination of optical faintness and lack of strong lines in the observed range for distant *Chandra* sources or the inadequate observing set-up among brighter nearby objects (Severgnini et al. 2003) may account for the *XBONG* properties. However, it has been shown that this is not the case for a significant fraction of "local" *XBONGs* on the basis of the upper limits on the O[III]$_{5007\AA}$ luminosity (Cocchia et al. 2007) as well as for more distant z $\sim$ 1 sources, for which the optical-to-X-ray luminosity ratio is fully consistent with that of "normal" Seyferts and quasars (Rigby et al. 2006).

For those sources for which the dilution hypothesis can be safely ruled out, the alternative possibilities could be grouped in two classes: *obscured* and *exotic*.

The first one is that *XBONGs* are merely obscured AGN:

• In order to explain the multiwavelength properties of the *XBONG* prototype PKS 0312017, also known as P3, Comastri et al. (2002) suggest heavy obscuration by Compton-thick gas covering almost 4π at the nuclear X-ray sources. In this way no ionizing photons can escape to produce the narrow emission lines which are observed in "normal" Type 2 AGN (NLAGN, narrow-line AGN) which are thought to have a lower covering fraction in the AGN Unified scheme. See Chapter 4 for a recent re-analysis of the X-ray data of P3.

• According to a detailed multiwavelength analysis of "optically-dull" galaxies in the *Chandra* deep fields, Rigby et al. (2006) conclude that extranuclear dust in the host galaxy plays an important role in hiding the emission lines.

More intriguingly, *XBONGs* may be members of a class, or classes, of *exotic* objects:

• Radiatively Inefficient Accretion Flows (RIAFs) are expected at accretion rates well below those inferred for Seyferts and quasars. A distinctive property of low accretion-rate

flows is that the standard Shakura-Sunyaev accretion disk is truncated at a relatively large inner radius. As a consequence, it cannot generate the "big blue bump" and enough UV photons to photoionize the line-emitting circumnuclear gas. The infalling gas is heated to high temperatures and emits a hard X-ray power-law by upscattering of low-energy seed photons. According to Yuan & Narayan (2004), the SED of source P3 could be fitted by a RIAF model.

• *XBONGs* could be extreme BL Lac objects in which the featureless non-thermal continuum is much weaker than the host galaxy starlight. Following Fossati at al. (1998), *XBONGs* could belong to the low-luminosity tail of the blazar spectral sequence based on the anti-correlation between luminosity and frequency of the synchrotron peak.

• A highly speculative possibility is that of a transient AGN in the process of tidally disrupting a star. If this were the case, the X-ray emission should be witnessing the transient accretion phenomenon (see Komossa et al. 2004 for extreme variability events in ROSAT observations; se also Gezari et al. 2006 for a luminous flare observed in the GALEX Deep Imaging Survey). The transient is most likely over in subsequent follow up optical observations.

It should also be noted that diffuse emission from a galaxy group, whose X-ray extended emission may have escaped detection in low signal-to-noise X-ray observations, is also possible and indeed observed in a few cases (Georgantopoulos et al. 2005).

Although some of the explanations mentioned above provide a good description of the observed properties for a few objects, the very nature of *XBONGs* is still subject of debate.

Chapter 2

X–ray spectral analysis of optically faint sources

At the limits of deep *Chandra* surveys, high X/O sources are characterized by extremely faint optical magnitudes and spectroscopic identification is not feasible even with the largest telescopes. In this framework a detailed investigation of their X–ray properties may provide useful information on the nature of this important component of the X–ray source population. In the following are presented the results of detailed X–ray spectral analysis combined with the available multiwavelength information for a large sample of high X/O sources in the *Chandra* Deep Field North (Alexander et al. 2003) and *Chandra* Deep Field South (Giacconi et al. 2002).

2.1 Sample selection

We have selected 127 hard X–ray sources in the *Chandra* Deep Fields (63 in the *CDFN* and 64 in the *CDFS*) with an X–ray to optical flux ratio $\log{(f_X/f_R)} > 1$ defined as in equation 1.1. In order to be consistent with the published optical catalogues for the costant in equation 1.1, we used C=5.5 for the *CDFN* and C=5.71 for the *CDFS*. The hard band (2–8 keV) fluxes and the basic X–ray source properties (positions, counts, exposure times) have been compiled from the Alexander et al. (2003) X–ray source catalogue for *CDFN* and *CDFS*. The R–band magnitudes, along with optical identification and classification (when available), have been retrieved from Barger et al. (2003) for the *CDFN*, Giacconi et al. (2002), Szokoly et al. (2004) and Zheng et al. (2004) for the *CDFS*. Figure 2.1 shows the R–band magnitude versus the 2–8 keV flux for the 127 high X/O sources discussed in this work.

For each source we report in Table 2.1 and 2.2 the X–ray identification number (col. 1), the X–ray coordinates (col. 2 and 3), the hard X–ray flux (col. 4), the optical R–band
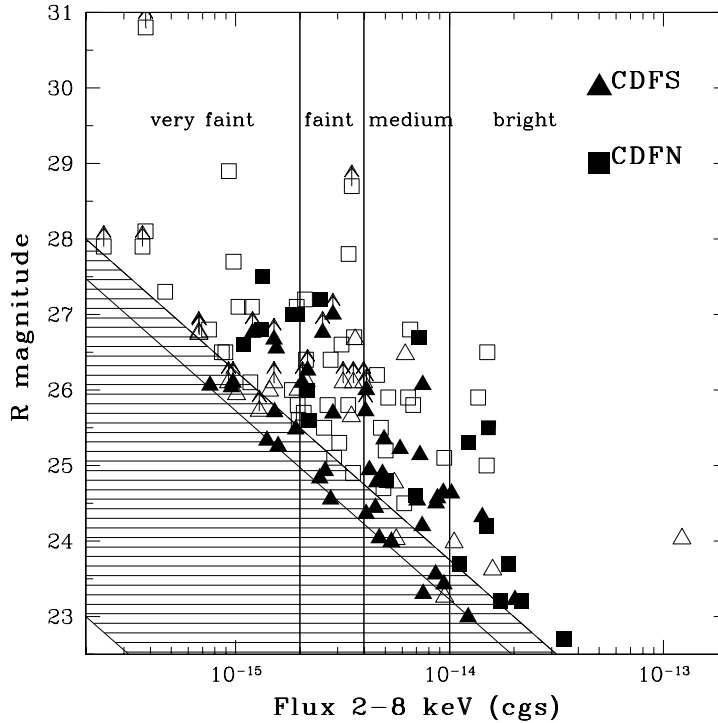
Figure 2.1: The R–band magnitude vs. the 2–8 keV flux for the 127 high X/O sources selected from the *CDFN* (squares) and *CDFS* (triangles) samples. Filled symbols are objects with redshift identification. The dashed area represents the locus occupied by known AGN (e.g. quasars, Seyferts, emission–line galaxies) along the correlation X/O=0±1. Two upper boundaries at X/O=1 are reported as we used two different constants for the *CDFN* and the *CDFS* (see Sect. 2 for details). The vertical lines are the boundaries of the 4 flux bins discussed in Section 2.3.1.

magnitude in the Vega sistem (col. 5), the magnitude reference for *CDFS* (col. 6) and the X/O from equation 1.1 (col. 7 and 6, respectively). Sources undetected in the R band are reported as lower limits in Tables 2.1 and 2.2 and in these cases the X/O ratio has to be considered a lower limit. All the high X/O objects represent $\sim 23\%$ of the hard X–ray sources revealed in both deep fields.

2.2 Data reduction

The *CDFS* 1 Megasecond dataset is the result of the co-addition of 11 individual *Chandra* ACIS–I exposures whose aimpoints are at a few arcsec from each other. The total area covered is $\sim$392 arcmin^2; this field was selected in a patch of the southern sky (nominal aim point $\alpha_{2000} = 03^h32^m28^s.0$ e $\delta_{2000} = -27°48'30''$) characterized by a very low Galactic neutral hydrogen column density (8×10^{19} cm^{-2}) and by the lack of bright stars (Rosati et al. 2002).

The *CDFN* has been observed by about 2 Megaseconds over a period of 27 month, and is the result of the co-addition of 20 individual *Chandra* ACIS-I exposures centered

Table 2.1: Properties of high X/O sources in the *CDFS*.

XID	RA	DEC	f_X [a]	R	Ref. [b]	X/O	z	z type [c]
3	3:33:05.85	-27:46:50.2	3.18	>26.10	G	>1.65	...	+
8	3:33:01.44	-27:41:42.0	9.40	23.43	S	1.06	0.99	phot (0.9)
20a	3:32:44.47	-27:49:40.2	5.34	23.99	S	1.03	1.016	spec
23	3:32:41.85	-27:43:59.9	2.62	24.93	S	1.10	0.73	phot (0.5)
25	3:32:40.84	-27:55:46.6	9.34	24.64	S	1.54	2.26	phot (0.5)
26	3:32:39.73	-27:46:11.2	2.78	24.55	S	0.97[†]	1.624	phot (0.5)
27	3:32:39.68	-27:48:50.7	7.06	24.54	S	1.37	3.064	spec
31	3:32:37.77	-27:52:12.4	8.78	24.57	S	1.48	1.603	spec
35	3:32:34.37	-27:39:13.1	14.2	24.32	S	1.59	1.51	spec
45	3:32:25.68	-27:43:05.8	4.94	25.35	S	1.54	2.291	spec
48	3:32:24.84	-27:56:00.0	4.86	24.89	G	1.35	0.841	phot[d]
51a	3:32:17.18	-27:52:20.9	20.2	23.22	S	1.30	1.097	spec
54	3:32:14.57	-27:54:21.6	2.85	25.69	S	1.44	2.561	spec
57	3:32:12.95	-27:52:36.7	4.69	24.04	S	1.00	2.562	spec
58	3:32:11.77	-27:46:28.2	1.96	26.00	S	1.40	...	*
59	3:32:11.41	-27:52:13.5	6.21	26.47	S	2.09	...	++
61	3:32:10.50	-27:43:09.0	10.5	23.98	S	1.32	...	*
64	3:32:08.00	-27:46:57.2	5.52	24.77	S	1.36	...	+
65	3:32:03.90	-27:53:28.9	2.17	>26.26	S	>1.55	1.10	phot (0.5)
67	3:32:02.46	-27:46:00.3	8.61	23.56	S	1.07	1.616	spec
69a	3:32:01.43	-27:41:38.6	5.63	24.02	S	1.07	...	+
70a	3:32:01.42	-27:46:47.1	15.9	23.62	S	1.36	...	+
72a	3:31:58.29	-27:50:41.6	7.48	26.07	S	2.01	1.99	phot (0.5)
76	3:31:52.50	-27:50:17.5	8.64	24.50	S	1.45	2.394	spec
79	3:32:38.03	-27:46:26.2	1.55	26.55	S	1.52	1.91	phot (0.5)
81	3:32:25.96	-27:45:14.3	0.95	26.04	S	1.11	2.59	phot (0.5)
82a	3:32:14.87	-27:51:03.8	1.51	>26.1	S	>1.33	...	*
99	3:32:05.17	-27:53:54.7	5.87	25.22	S	1.57	0.79	phot (0.5)
108a	3:32:05.77	-27:44:46.6	1.01	25.94	S	1.09	...	*
112	3:31:51.98	-27:53:26.7	2.47	24.83	S	1.03	2.942	spec
133	3:32:02.52	-27:44:29.8	0.67	>26.74	G	>1.23	...	++
145	3:32:22.54	-27:46:03.9	4.56	24.78	S	1.28	1.50	phot (0.5)
146	3:32:47.05	-27:53:33.3	2.55	>26.76	G	>1.82	2.67	phot (0.5)
147	3:32:46.35	-27:46:31.9	7.26	25.14	S	1.63	0.99	phot (0.5)
148	3:32:35.23	-27:53:17.8	2.85	>27	S	>1.96	1.74	phot (0.5)
153	3:32:18.34	-27:50:55.2	7.45	24.20	S	1.26	1.536	spec
159	3:32:50.23	-27:52:51.7	7.53	23.30	S	0.90[†]	3.3	phot (0.5)
179	3:31:49.49	-27:50:34.0	0.97	>26.10	G	>1.14	2.73	phot (0.5)
201a	3:32:39.06	-27:44:39.1	2.14	26.11	S	1.48	...	*
205a	3:32:17.11	-27:41:36.6	1.44	25.99	S	1.26	...	++
207a	3:32:07.96	-27:37:35.1	122.0	24.03	S	2.41	...	+
209	3:31:47.30	-27:53:13.3	10.2	24.63	S	1.57	1.32	phot (0.5)
213a	3:32:00.56	-27:53:53.0	3.47	25.65	S	1.51	...	++
219	3:31:50.43	-27:51:51.8	3.96	>26.10	G	>1.75	...	*
227	3:32:05.35	-27:46:44.1	3.62	26.67	S	1.94	...	*
243	3:32:08.39	-27:40:47.0	4.05	>25.72	G	>1.61	2.50[e]	phot (0.3)
253	3:32:20.07	-27:44:47.0	4.22	24.94	S	1.31	1.89	spec
256	3:32:43.05	-27:48:45.0	4.07	24.36	S	1.06	1.53	phot (0.5)
259	3:32:06.13	-27:49:27.7	4.50	24.44	S	1.14	1.76	phot (0.5)
261	3:31:57.03	-27:51:08.6	3.55	>26.10	G	>1.70	...	**
263b	3:32:18.89	-27:51:35.4	1.40	25.33	S	0.99[†]	3.66	spec
265	3:32:33.27	-27:42:36.1	4.08	>26.00	G	>1.72	1.16	phot (0.5)
501	3:33:10.18	-27:48:41.8	12.2	22.99	S	0.99[†]	0.81	phot (0.6)
503	3:33:07.61	-27:51:26.6	9.48	23.26	S	0.99[†]	...	+
505a	3:33:04.83	-27:47:31.9	1.91	25.48	S	1.18	0.981	phot[d]
506	3:33:02.97	-27:51:46.4	0.93	>26.10	G	>1.12	...	*
508	3:32:51.64	-27:52:12.8	1.20	>26.76	G	>1.49	2.5	phot (0.5)
513a	3:32:34.03	-27:48:59.9	0.76	26.06	S	1.01	3.53	phot (0.5)
515	3:32:32.17	-27:46:51.4	1.51	>26.67	G	>1.56	2.19	phot (0.5)
518	3:32:26.75	-27:46:04.3	0.67	>26.76	G	>1.21	...	++
524	3:32:19.96	-27:42:43.2	1.29	>25.72	G	>1.11	...	*
533	3:32:13.90	-27:56:00.1	2.05	>26.10	G	>1.46	0.54	phot (0.5)
595	3:32:15.75	-27:39:53.8	1.52	25.71	S	1.18	0.36	phot (0.5)
606a	3:32:24.97	-27:50:08.2	1.58	25.26	S	1.01	1.037	spec

[a] In units of 10^{-15} erg cm^{-2} s^{-1}. [b] G = Giacconi et al. 2002, S = Szokoly et al. 2004. [c] The photo–z quality flag (QF) from Zheng et al. (2004) is reported in brackets; QF=0.3 means that the redshift is from the BPZ code; QF=0.5 means that two indipendent codes (BPZ and HyperZ) return consistent values; QF=0.6 means that HyperZ code returns the same value of COMBO-17 catalogue; QF=0.9 means that the value returned by BPZ and HyperZ is confirmed in the COMBO-17 catalogue. [d] Photometric redshift from COMBO-17 survey catalogue (Wolf et al. 2004). [e] Although QF=0.3, the detection of a Kα line (Gilli, private communication) at the best–fit photo–z makes us confident on this value. [†] The 5 sources with X/O slightly lower than 1 would have X/O > 1 if the X–ray flux quoted in Giacconi et al. (2001) is considered. [+] Sources with QF≤0.4 in Zheng et al. (2004). [++] QF=0.5 but with a large error on redshift estimate ($\Delta z \geq 1.0$). [*] The optical counterpart presented in Zheng et al. (2004) lies at > 2" from the Alexander et al. (2003) position. [**] Source 261 is not present in Zheng et al. (2004).

Table 2.2: Properties of high X/O sources in the *CDFN*.

XID	RA	DEC	f_X [a]	R	X/O	z	z type [b]
7	12:35:21.71	+62:15:01.6	2.11	27.2	1.704	...	...
9	12:35:24.92	+62:15:24.8	4.77	25.5	1.378	...	...
10	12:35:28.77	+62:14:27.8	4.58	26.2	1.640	...	...
12	12:35:29.45	+62:18:22.8	3.36	25.8	1.346	...	...
28	12:35:46.07	+62:15:59.9	2.48	27.2	1.774	1.93	phot
29	12:35:46.25	+62:17:29.8	1.93	27.1	1.625	...	...
36	12:35:50.42	+62:18:08.6	12.3	25.3	1.71	0.52	Kα
38	12:35:51.75	+62:17:57.1	15.0	26.5	2.276	...	...
42	12:35:54.11	+62:20:12.3	0.86	26.5	1.035	...	...
48	12:35:56.14	+62:12:19.2	18.8	23.7	1.25	1.13	Kα
71	12:36:05.62	+62:06:54.0	1.95	25.8	1.11	...	...
73	12:36:05.83	+62:08:38.0	2.78	26.4	1.50	...	...
91	12:36:11.40	+62:21:49.9	9.44	25.1	1.51	...	...
98	12:36:13.02	+62:12:24.1	1.97	25.6	1.03	...	...
92	12:36:11.80	+62:10:14.5	2.69	25.8	1.24	...	...
98	12:36:13.02	+62:12:24.1	1.97	25.6	1.03	...	...
100	12:36:14.14	+62:10:17.7	0.93	28.9	2.028	...	...
102	12:36:14.45	+62:10:45.0	3.54	24.9	1.00	...	...
107	12:36:15.83	+62:15:15.5	1.85	27.0	1.567	2.06	phot
108	12:36:16.03	+62:11:07.7	15.2	25.5	1.88	1.25	phot
129	12:36:21.94	+62:16:03.8	1.32	26.8	1.34	2.26	phot
134	12:36:22.65	+62:10:28.5	2.89	25.1	1.00	...	...
140	12:36:23.66	+62:10:08.7	0.47	27.3	1.09	...	...
146	12:36:25.33	+62:17:37.7	2.21	25.6	1.084	1.28	phot
151	12:36:27.53	+62:12:18.0	0.24	>27.9	>1.04	...	...
154	12:36:28.65	+62:21:39.5	14.9	25	1.673	...	...
156	12:36:28.78	+62:11:40.0	0.38	>30.8	>2.39	...	...
165	12:36:30.15	+62:26:20.1	11.1	23.7	1.025	1.46	phot
186	12:36:34.71	+62:04:37.9	2.08	25.7	1.098	...	...
195	12:36:36.85	+62:22:27.4	2.13	26.4	1.38	...	...
196	12:36:36.90	+62:13:20.0	0.38	28.1	1.32	...	...
204	12:36:38.94	+62:10:41.5	0.37	>27.9	>1.22	...	...
232	12:36:44.95	+62:26:51.0	4.91	24.7	1.07	...	...
246	12:36:47.94	+62:10:19.9	1.94	27.0	1.58	2.52	phot
250	12:36:48.28	+62:14:56.2	1.34	27.5	1.62	2.09	phot
253	12:36:48.73	+62:21:53.9	2.59	25.5	1.11	...	...
259	12:36:49.66	+62:07:38.3	21.8	23.2	1.11	1.609	spec
290	12:36:56.56	+62:15:13.1	0.75	26.8	1.09	...	...
318	12:37:01.76	+62:07:20.8	0.98	27.7	1.57	...	...
321	12:37:02.43	+62:19:26.1	3.05	25.3	1.10	...	...
334	12:37:04.87	+62:16:01.6	6.40	25.9	1.66	...	...
335	12:37:05.12	+62:16:34.8	1.03	27.1	1.35	...	...
336	12:37:05.31	+62:24:54.8	3.12	26.6	1.63	...	...
350	12:37:07.70	+62:05:34.6	1.83	26	1.16	...	...
357	12:37:09.40	+62:22:14.4	6.94	24.6	1.18	1.43	phot
374	12:37:13.84	+62:18:26.2	1.19	27.1	1.41	...	...
382	12:37:15.19	+62:02:31.0	6.76	25.8	1.64	...	...
390	12:37:16.65	+62:17:33.3	17.3	23.2	1.01	1.146	spec
400	12:37:20.26	+62:07:26.7	0.89	26.5	1.05	...	...
406	12:37:22.44	+62:05:36.1	3.37	27.8	2.14	...	...
412	12:37:24.00	+62:13:04.3	6.13	24.5	1.08	...	...
413	12:37:24.29	+62:13:59.7	5.09	24.8	1.13	0.474	spec
444	12:37:36.85	+62:14:29.2	5.16	25.9	1.57	...	...
445	12:37:37.04	+62:18:34.4	3.58	26.7	1.73	...	...
452	12:37:39.46	+62:22:39.2	3.49	>28.7	>2.52	...	...
456	12:37:41.13	+62:10:47.9	1.09	26.6	1.77	1.60	phot
463	12:37:45.02	+62:07:18.9	7.20	26.7	2.03	2.50	phot
465	12:37:46.78	+62:07:12.6	1.17	26.1	1.00	...	...
470	12:37:50.22	+62:13:59.3	2.17	26.0	1.23	0.23	spec
490	12:38:10.56	+62:17:29.6	14.8	24.2	1.35	1.02	phot
495	12:38:22.30	+62:14:16.7	34.4	22.7	1.11	0.986	spec
498	12:38:23.66	+62:09:42.4	5.03	25.2	1.28	...	...
497	12:38:23.21	+62:15:18.3	6.54	26.8	2.03	...	...
501	12:38:34.29	+62:14:40.9	13.6	25.9	1.99	...	...

[a] In units of 10^{-15} erg cm^{-2} s^{-1}. [b] Redshift type: spectroscopic, photometric or from the Kα iron line.

(nominal aim point $\alpha_{2000} = 12^h36^m49^s.4$ $\delta_{2000} = 62°12'58''$) close to the Hubble Deep Field North (HDF–N, Williams et al. 1996), the most studied region of the sky with a low Galactic neutral hydrogen column density (1.6×10^{20} cm^{-2}, Stark et al. 1992). Due to the different pointings, required to keep the HDF–N near the aim point and the *Chandra* roll angle constraints, the area covered is 447.8 arcmin^2.

The X–ray data have been retrieved from the public archive and processed with standard tools making use of the calibrations associated with the *CIAO*[1] software (version 3.0). All the observations of both fields have been registered on the deepest one and have been aligned using *align_evt*[2].

2.2.1 Stacking procedure

Since the main aim of the present work concerns the average spectral properties of relatively faint sources, the issue of co-adding spectra obtained from observations performed with different aim points and roll angles has to be treated appropriately. In principle, for each pointing and each object the source and background spectra, along with the detector position–dependent response matrix and effective area should be computed and then summed together ("standard" procedure). In practice, such an approach results to be extremely time consuming. In order to compute, from the total merged event file, all the relevant files needed for the spectral analysis, an alternative approach has been devised.

This approach is based on two *CIAO* tools (*mkwarf, mkrmf* [3]) developed to properly extract spectral data from multiple regions either from the same or different observations. Given that both the spectral response and the effective area vary with the position in the detector plane, the above mentioned tools allow us to compute weighted response and effective area files taking into account the position on the detector, the shape and area of the sources extraction regions.

In order to test whether these tools could be applied to multiple extraction regions in co-added observations, we proceeded as follows.

We considered several different samples of N sources, randomly distributed over the detector and detected in each single exposure of the *CDFN* and the *CDFS*. The extraction regions were chosen according to the number of counts of each source and to the off–axis angle of the source in each exposure and tuned to enclose the 90% of the PSF at 6.4 keV. This energy has been chosen since our sources have been selected in the hard band (§2.1). Several background spectra were extracted from a stack of regions nearby each source and varied in size and shape. The stacked spectra of N-sources have been extracted using the well suited region files, as already described, from the merged event files of the *CDFN* and the *CDFS*. Making use of *mkwarf* and *mkrmf*, the relevant matrices *ARF* and *RMF*

---

[1] http://cxc.harvard.edu/ciao/
[2] http://cxc.harvard.edu/cal/ASPECT/align_evt/
[3] see webpage for a detailed description of the tools

have beeen extracted from the merged event files too. The ancillary response file has been corrected for the well known degradation of the *ACIS* quantum efficiency using the latest version of the *ACISABS* tool [4].

In order to check the reliability of our procedure we have computed the average stacked spectrum of 30 X–ray sources in the *CDFN* and 35 in the *CDFS* spectroscopically identified as broad–line AGN by Barger et al. (2003) and Szokoly et al. (2004), respectively (see Fig. 2.2). The best–fit parameters of a single absorbed power law are: $\Gamma=1.73\pm0.03$, $N_H(z=0)=7\pm1\times10^{20}$ cm^{-2} in the *CDFN* and $\Gamma=1.82\pm0.04$, $N_H(z=0)=4.7\pm1.44\times10^{20}$ cm^{-2} in the *CDFS*, slightly flatter ($\Delta\Gamma\sim$0.1-0.2) than the "canonical" value (e.g. Γ=1.9–2.0; Nandra & Pounds 1994), but fully consistent with the fact that no reflection component has been included in the spectral fitting. Moreover, in the *CDFN* our results are in excellent agreement with those reported by Bauer et al. (2002) for a sample of broad–line AGN largely overlapping with ours. Given that the Bauer et al. results have been obtained applying a rather different (IDL based) data reduction procedure (ACIS-Extract), we are confident of the reliability of our method.

2.3 Spectral analysis

The stacked spectra have been extracted in the 0.7–7 keV band, to minimize residual calibration uncertainties of the low energy instrumental response, and rebinned to have at least 20 counts per bin. X–ray spectral fitting was performed using XSPEC (version 11.3.0; Arnaud 1996); errors are reported at the 90% confidence level for one interesting parameter ($\Delta\chi^2$=2.71). In all the fits, a "negative" edge ($\tau=-0.17$) at 2.07 keV has been included to take into account calibration uncertainties around the instrumental Iridium edge (Vikhlinin, private communication [5]).

2.3.1 Average spectra

The stacked spectra of the high X/O sources in both the *CDFN* (about 30000 net counts) and *CDFS* (about 19500 net counts) were fitted with an absorbed power–law model with absorption fixed at the Galactic value (hereinafter MODEL 1).

The resulting best–fit slopes are Γ(*CDFN*)=0.77$\pm$0.02 and Γ(*CDFS*)=0.97$\pm$0.03. Although the residuals (Fig. 2.3) indicate a more complex curved shape, these extremely hard spectra strongly suggest that high X/O sources represent the most obscured component of the X–ray background below 5–6 keV. Even more obscured, possibly Compton–thick AGN, so far undetected in deep surveys, might be responsible of the XRB at higher energies (Worsley et al. 2004). The measured values are significantly flatter than the average spectrum of the total *CDFS* sample in the 1–10 keV range ($\langle\Gamma\rangle$=1.375$\pm$0.015; Rosati et al. 2002) as well as of the average XRB slope ($\Gamma\simeq1.4$) in the same energy range.

---

[4]http://chandra.ledas.ac.uk/ciao3.0/threads/apply_acisabs/
[5]http://asc.harvard.edu/ccw/proceedings/03_proc/presentations/zhao/index.html
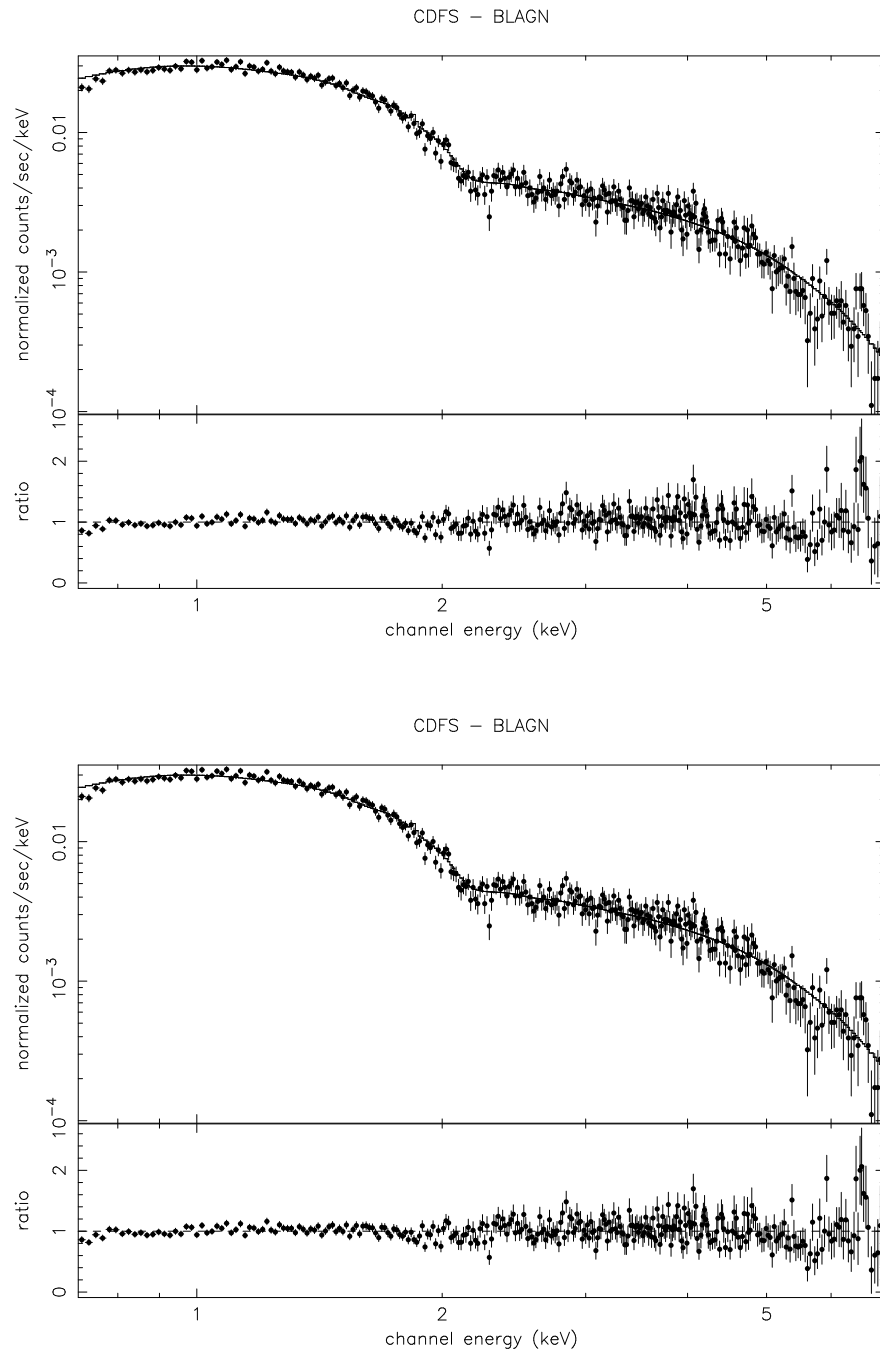
CDFS – BLAGN

CDFS – BLAGN

Figure 2.2: Stacked spectra of X–ray sources spectroscopically identified as broad–line AGN in the *CDFS* and in the *CDFN*. The best–fit parameters of a single absorbed power law are reported in the text.
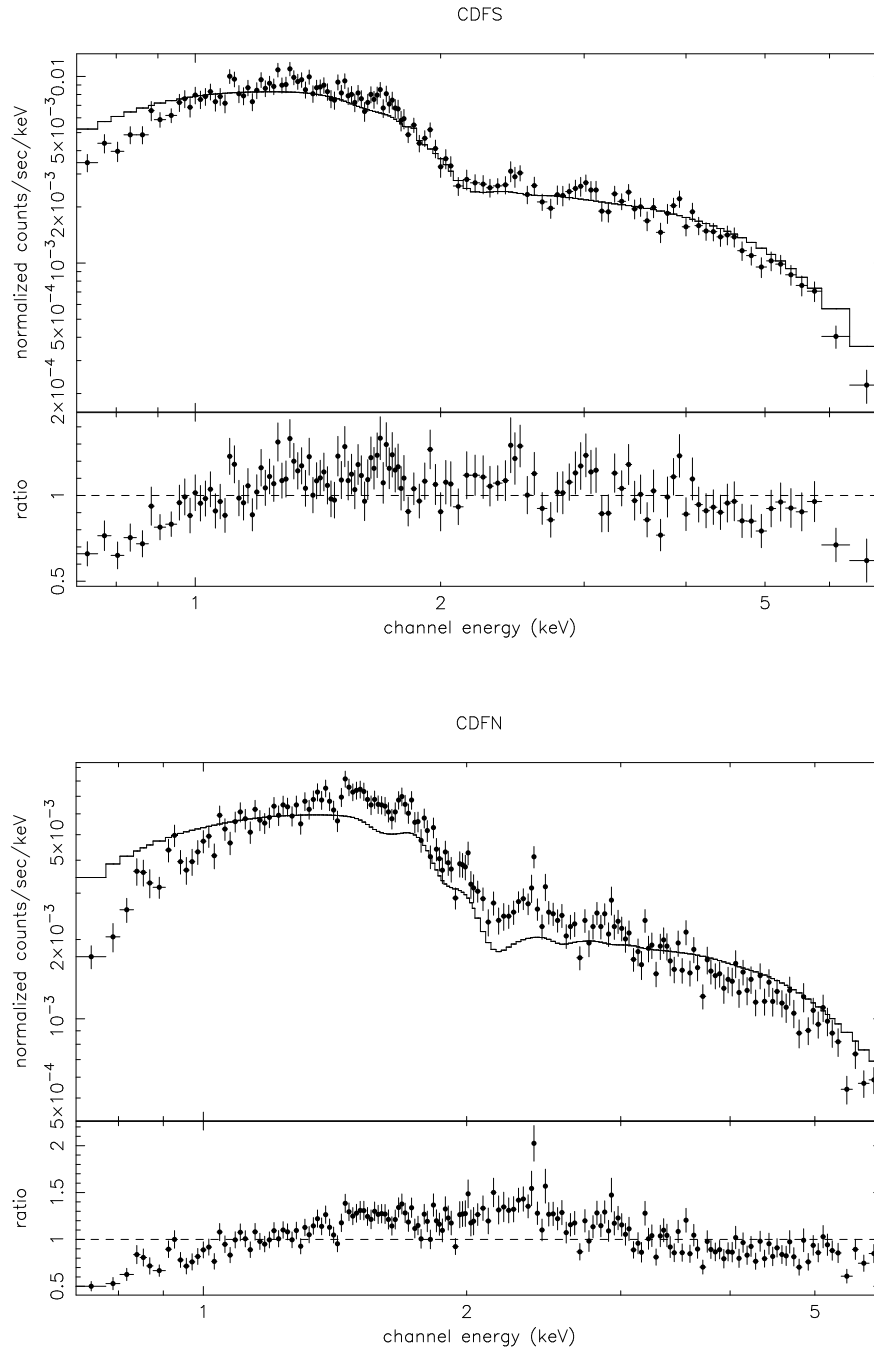
Figure 2.3: Stacked spectra of all the high X/O sources in *CDFS* (64 sources) and *CDFN* (63 sources), fitted in the 0.7-7 keV energy band with a power–law spectrum (MODEL 1). The best–fit spectral slopes are reported in Table 2.3. The solid line is the best-fit model, while the lower panel shows the data-to-model ratio.
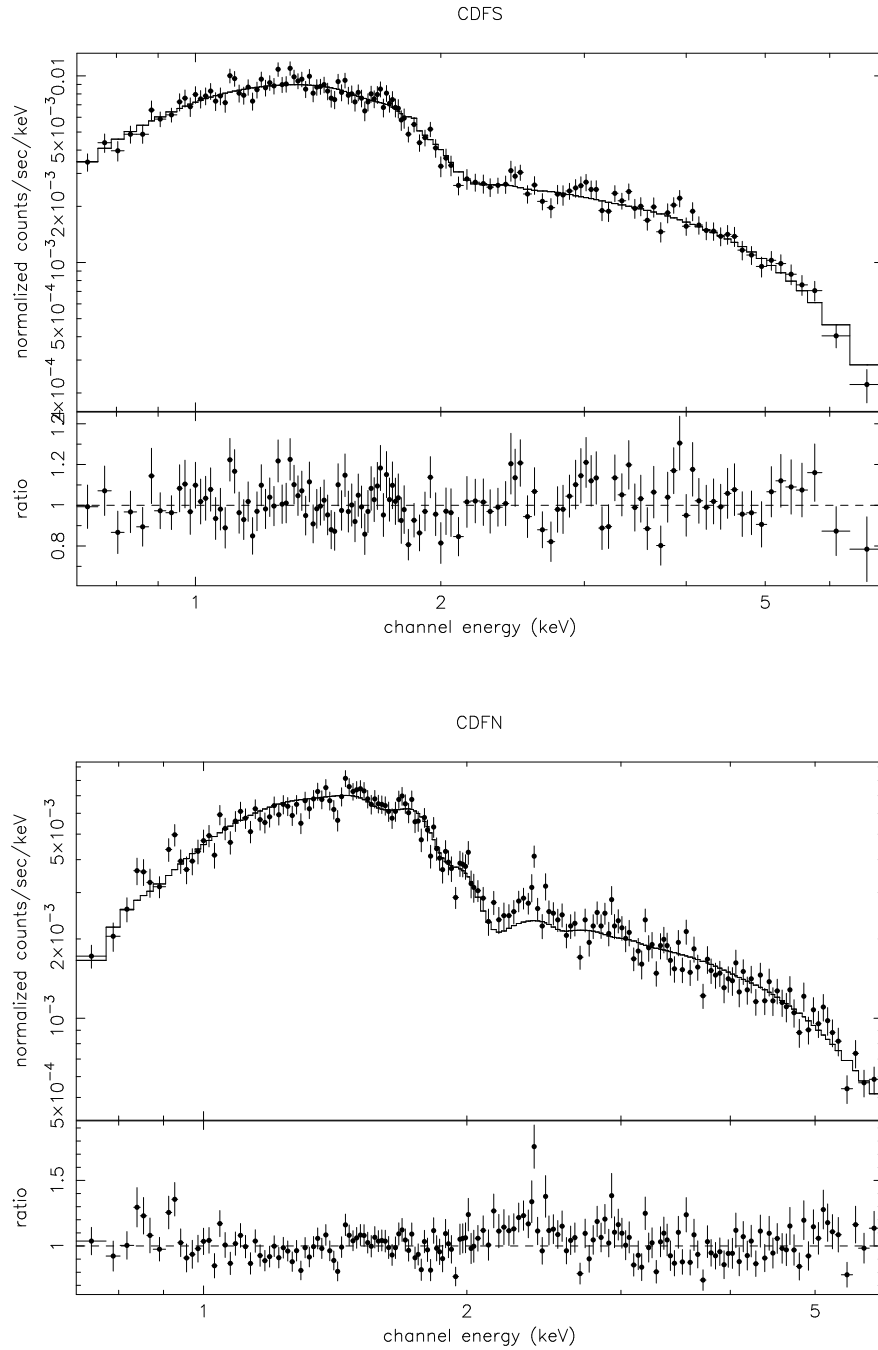
Figure 2.4: Stacked spectra of all the high X/O sources selected in *CDFS* (64 sources) and *CDFN* (63 sources), fitted in the 0.7-7 keV energy band with an absorbed power–law spectrum (MODEL 2). The best–fit column densities and spectral slopes are reported in Table 2.3. The solid line is the best-fit model , while the lower panel shows the data-to-model ratio.
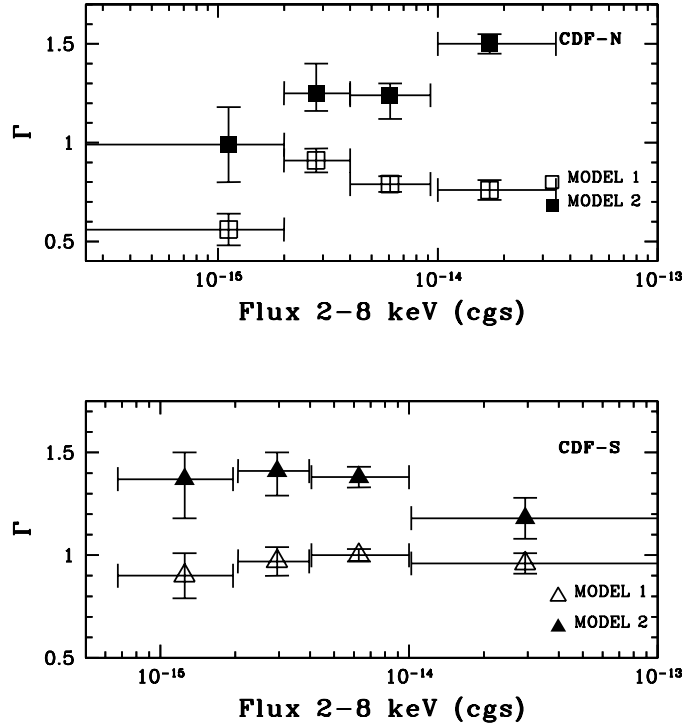
Figure 2.5: Spectral index Γ vs. hard X-ray flux obtained with MODEL 1 (open symbols) and MODEL 2 (filled symbols) for the 4 subsamples of *CDFN* (squares, top panel) and *CDFS* (triangles, bottom panel). The errors on the slope are at the 90% confidence level; the horizontal bars represent the bin width.

Leaving the absorption free to vary (hereinafter MODEL 2), the quality of the fit improves significantly (Fig. 2.4). The best–fit slopes and column densities are: $\Gamma=1.34\pm0.04$, $N_H(z=0)=4.1\pm0.3\times10^{21}$ cm^{-2} for the *CDFN* and $\Gamma=1.34\pm0.03$, $N_H(z=0)=2.4\pm0.4\times10^{21}$ cm^{-2} for the *CDFS*. Given that the stacked objects are likely to be distributed over a range of redshifts and that no redshift dependence has been considered, the N_H values have to be considered as lower limits to any absorption component. For the same reason, the intrinsic power–law slope might well be steeper, the observed value being the result of a distribution of column densities convolved with redshift.

The accumulated source counts in the stacked spectra are sufficient to further investigate the spectral properties of high X/O sources and, in particular, to search for the progressive hardening of the mean spectral slope towards faint fluxes; this hardening has been clearly established both in the *CDFS* (Rosati et al. 2002) and *CDFN* (Alexander et al. 2003) full samples.

The high X/O sources of our sample were divided in four 2–8 keV flux intervals (see Fig. 2.1). The bin width was optimized to keep the total number of counts in each bin adequate to perform spectral analysis. The flux intervals were defined as follows: bright (A, $> 10^{-14}$ erg cm^{-2} s^{-1}), medium (B, 4×10^{-15}–10^{-14} erg cm^{-2} s^{-1}), faint (C, 2×10^{-15}–4×10^{-15} erg cm^{-2} s^{-1}) and very faint (D, $<2\times10^{-15}$ erg cm^{-2} s^{-1}). Stacked
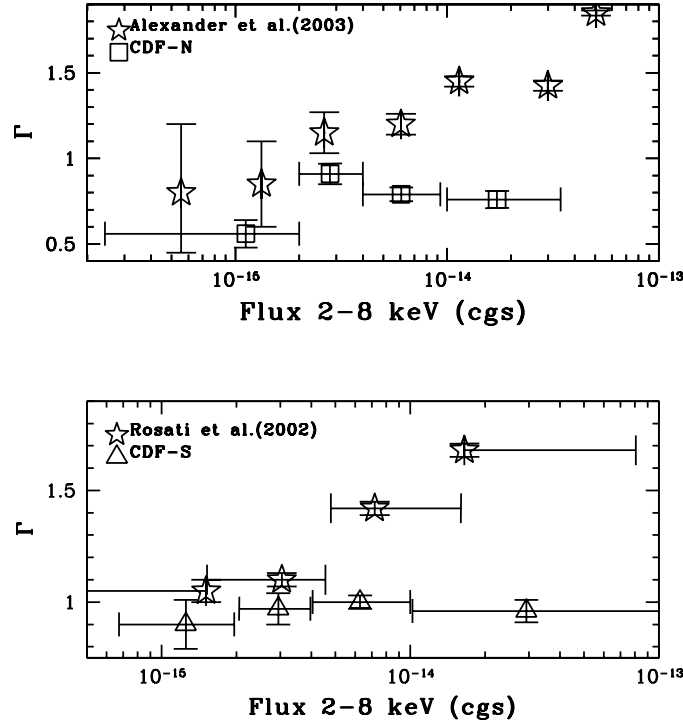
Figure 2.6: Top panel: Spectral index Γ vs. hard X-ray flux obtained with MODEL 1 for high X/O *CDFN* subsamples (squares) compared with the values of Γ as obtained from band ratios for the entire *CDFN* sample (stars, Alexander et al. 2001, 2003). Bottom panel: Spectral index Γ vs hard X-ray flux obtained with MODEL 1 for high X/O *CDFS* subsamples (triangles) compared with the values obtained for all *CDFS* hard sample (stars, Rosati et al. 2002)

spectra in each subsample were extracted following the procedure described in Sect. 2.2.1 and fitted with both MODEL 1 and MODEL 2: the best–fit parameters are reported in Table 2.3, and shown in Figure 2.5. There is no clear evidence of a spectral flattening as a function of the X–ray flux, with a possible exception for the *CDFN* sources fitted with MODEL 2. The average spectrum of high X/O sources remains constant with a very hard slope ($\Gamma \lesssim 1$) over about two decades of X–ray flux and definitely flatter than that measured for the entire *CDFS* and *CDFN* samples down to comparable limiting fluxes (see Fig. 2.6). The difference is more pronounced ($\Delta\Gamma \sim 0.7$) at fluxes brighter than $\sim 5\times 10^{-15}$ erg cm^{-2} s^{-1}, which are dominated by unobscured quasars with a soft X–ray spectrum, decreasing to $\Delta\Gamma \sim 0.15$ at fainter fluxes, where the contribution of obscured sources with X/O < 1 to the total sample is much higher.

A very flat 2–10 keV spectrum may also be the signature of a strong Compton reflection component and is expected for column densities in the Compton–thick regime ($N_H \gtrsim 2\times 10^{24}$ cm^{-2}). Spectral fits performed with a pure reflection spectrum (model *pexrav* in *XSPEC*) do not provide a statistically acceptable description of the data leaving significant residuals at low energy. The most straightforward explanation of the observed flat slope in the stacked spectra is in terms of the superposition of different photoelectric cut-offs

Table 2.3: Spectral fit parameters obtained with MODEL 1 and MODEL 2.

	Sample[a]	Model	Γ	$N_H(z=0)$[b]	χ^2/d.o.f.
CDFS	all (64)	MODEL 1	0.97 ± 0.03	Galactic[c]	429.2/261
		MODEL 2	1.34 ± 0.03	0.24 ± 0.04	255.8/260
	A (7)	MODEL 1	0.96 ± 0.05	Galactic	133.6/109
		MODEL 2	1.18 ± 0.1	0.15 ± 0.05	115.9/108
	B (25)	MODEL 1	1.00 ± 0.03	Galactic	368.3/254
		MODEL 2	1.38 ± 0.05	0.25 ± 0.04	259.1/253
	C (14)	MODEL 1	0.97 ± 0.07	Galactic	137.2/125
		MODEL 2	$1.41^{+0.09}_{-0.12}$	$0.27^{+0.09}_{-0.06}$	107.3/124
	D (18)	MODEL 1	0.90 ± 0.11	Galactic	105.9/99
		MODEL 2	$1.37^{+0.13}_{-0.19}$	$0.31^{+0.17}_{-0.11}$	92.3/98
CDFN	all (63)	MODEL 1	0.77 ± 0.02	Galactic[d]	1137.7/374
		MODEL 2	1.34 ± 0.04	0.41 ± 0.03	473.2/373
	A (11)	MODEL 1	0.76 ± 0.05	Galactic	1091.0/257
		MODEL 2	1.50 ± 0.05	0.53 ± 0.03	361.7/256 [e]
	B (13)	MODEL 1	0.79 ± 0.04	Galactic	279.0/168
		MODEL 2	$1.24^{+0.06}_{-0.12}$	0.30 ± 0.05	196.7/167
	C (17)	MODEL 1	0.91 ± 0.06	Galactic	180.2/151
		MODEL 2	$1.25^{+0.15}_{-0.09}$	$0.23^{+0.08}_{-0.04}$	146.0/150
	D (22)	MODEL 1	0.56 ± 0.08	Galactic	133.4/109
		MODEL 2	0.99 ± 0.19	$0.33^{+0.14}_{-0.10}$	113.6/108

[a] The number of sources in each bin is reported in brackets. [b] Units of 10^{22} cm^{-2}. [c] N_H(Gal)(*CDFS*) $= 8\times10^{19}$ cm^{-2}. [d] N_H(Gal)(*CDFN*) $=1.6\times10^{20}$ cm^{-2}. [e] The quality of the fit is not good due to features around 3 keV.

due to Compton–thin absorption likely spread over a broad range of redshifts.

2.3.2   The Kα iron line

The strongest emission feature in the hard X–ray spectrum of an active galactic nucleus (AGN) is the fluorescent FeKα emission line at 6.4–7 keV. The line properties – in particular the centroid energy, intensity and profile – carry important diagnostic information about the dynamics and physics of the region where the emission originates. For example, the best fit line energy is a measure of the ionization status of the gas, the line equivalent width (EW) is strongly correlated with the amount of fluorescing material, while the detection of a broad asymmetric profile, first resolved in the bright Seyfert 1 galaxy MCG–6–30–1 (Tanaka et al. 1995) , is considered the most direct evidence of the presence of an accretion disc extending down to a few gravitational radii of the central black hole. The detailed study of the iron line properties requires a large collecting area and good energy resolution. For this reason, most of the results obtained so far are limited to nearby, low luminosity Seyfert galaxies (e.g., Turner et al. 2002; Fabian et al. 2002; Dewangan, Griffiths & Schurch 2003; Miniutti et al. 2006; 2007; Jiménez-Bailón et al. 2007). The search for iron line emission at high redshift is hampered by the statistical

quality of the X–ray spectra and only a few tentative detections at the 2σ level have been reported. (e.g., Vignali et al. 1999; Reeves et al. 2001; Norman et al. 2002; Gandhi et al. 2004). Deep, sensitive X–ray observations offer the opportunity to search for the presence of iron emission line.

Redshift determination through Kα iron line

The residuals of a single power–law fit to the average spectrum of the *CDFN* bright subsample (A) are highly indicative of the presence of a line–like feature. Given that the FeKα line is the strongest emission feature, it can be used as redshift indicator. The eleven sources in subsample A have a counting statistic which is such to allow us for individual spectral analysis: spectra were extracted for these sources and fitted with MODEL 2. A clear excess suggesting the presence of an iron–line has been found in 4 of them (XID 36, 48, 259, 390). The Fe$K\alpha$ line of source 390 will be discuss in the next section. A spectroscopic redshift (z_{spec}=1.609) has been measured by Barger et al. (2003) for source 259; this value is fully consistent with that inferred from the iron $K\alpha$ line (z_{X-ray} =1.60$\pm$ 0.05).

The addition of a narrow Gaussian line due to cold iron (E_{rest} = 6.4 keV) in MODEL 2 improves the fit by $\Delta\chi^2 \simeq 9$ and $\simeq 15$ for source 36 and 48, respectively. The observed line energy corresponds to an X–ray redshift of $z = 0.52^{+0.03}_{-0.05}$ and $z = 1.13\pm0.05$, respectively. In figure 2.7 and 2.8, the spectra and the confidence contours of redshift versus line intensity are shown. The rest-frame equivalent widths are 293$\pm$204 eV and 400$^{+201}_{-195}$ eV, respectively. Assuming the redshift estimated by the iron line, the inferred column densities are $N_H = (1.20\pm0.15) \times 10^{22}$ cm^{-2} and $N_H = (3.2\pm0.3) \times 10^{23}$ cm^{-2}, respectively. The absorption corrected 2–10 keV luminosities are 1.3×10^{43} erg s^{-1} and 1.1×10^{44} erg s^{-1}, respectively. The measured values of intrinsic absorption and luminosity classify source 48 as a Type 2 quasar candidate.

A high redshift broad iron Kα line

A strong emission feature due to the Kα iron line (see Fig. 2.9) has been clearly detected in the X–ray spectrum of the relatively bright source 390. The spectroscopic redshift ($z = 1.146$) is based on a single $[OII]_{3727\AA}$ line (Barger et al. 2002). The compact optical morphology, the hard X–ray spectrum and the presence of a radio source coincident with the X–ray position (Richards 2000) leaves no doubt about the AGN nature of this object. On the basis of the available optical spectrum, it is not possible to determine whether the object is a Type 1 or a Type 2 AGN. Unfortunately, at the expected $Mg\,II_{2798\AA}$ position, the optical spectrum is contaminated by strong atmospheric bands and night-sky emission lines. The broad–band 0.6–7 keV *Chandra* spectrum is best described by a relatively hard ($\Gamma \simeq 1.5$) power law plus significant intrinsic absorption $N_H \sim 1.8\times 10^{22}$ cm^{-2}.

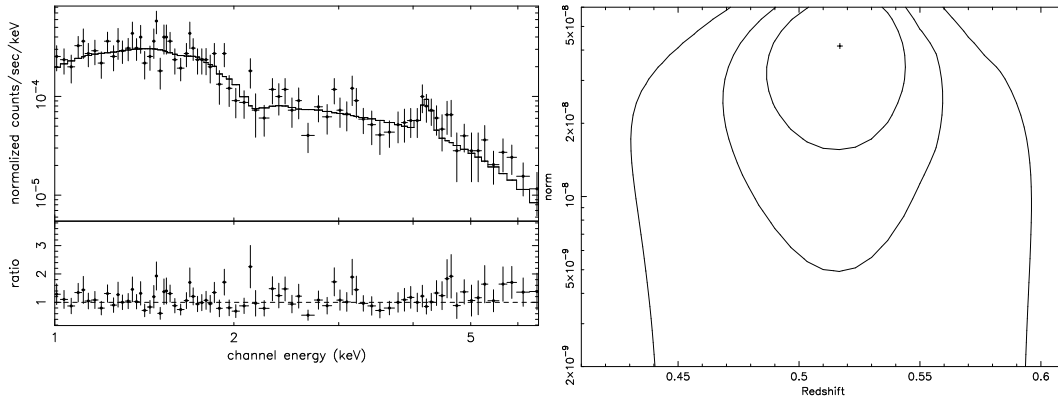The line profile is not consistent with a narrow feature, being significantly broader than

Figure 2.7: Left panel: the X–ray spectrum of source 36 (*CDFN*), fitted with an absorbed power–law plus a FeKα line (the best fit column density and spectral slope are $N_H = 1.20 \pm 0.15 \times 10^{22} \ cm^{-2}$ and $\Gamma = 1.56 \pm 0.07$) and residuals of the fit. Right panel: 68, 90, 99% confidence contours of the redshift versus line intensity.
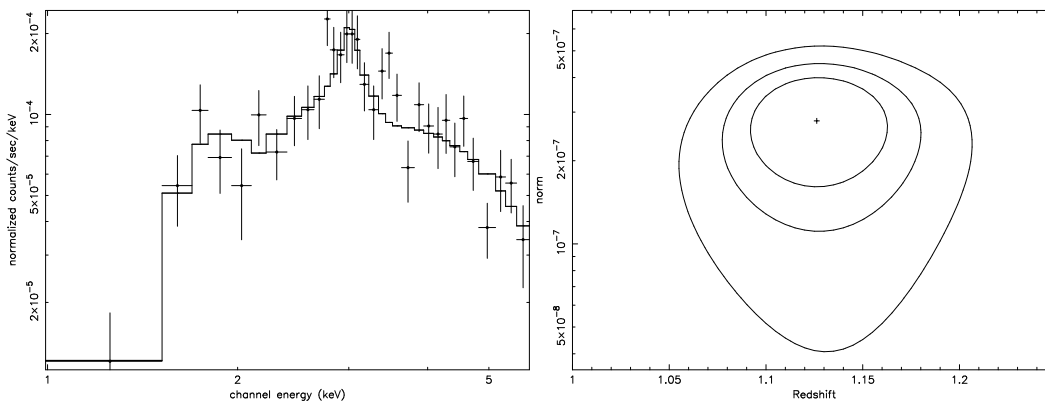

Figure 2.8: Left panel: the X–ray spectrum of source 48 (*CDFN*), fitted with an absorbed power–law plus a FeKα line (the best–fit column density and spectral slope are $N_H = 3.2 \pm 0.3 \times 10^{23} \ cm^{-2}$ and $\Gamma = 1.88 \pm 0.07$). Right panel: 68, 90, 99% confidence contours of the redshift versus the line intensity.
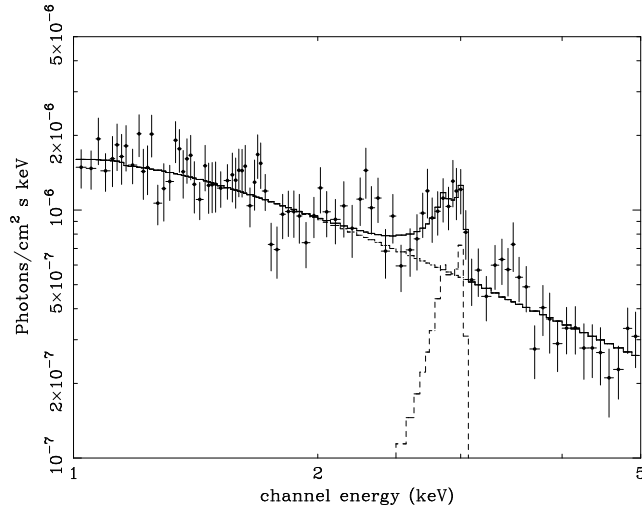
Figure 2.9: The unfolded spectrum, rebinned with at least 25 counts per channel, fitted with an absorbed power law ($\Gamma \simeq 1.5$; $N_H \simeq 1.7 \times 10^{22}$ cm^{-2}) plus a relativistic disk line.

the *ACIS-I CCD* resolution at that energy. Such a result does not depend on the adopted shape of the underlying continuum.

In order to reproduce both the observed width and the optical spectroscopic redshift, most of the line flux has to originate in a red wing. An adequate description of the overall line shape has been obtained with a relativistic line model. Although the quality of the data is not such to break the degeneracy between the various line parameters, the present observation suggests an almost face–on orientation of the accretion disk. The results of the spectral analysis are reported in Table 2.4. More details on interpretation of the line shape are reported in Comastri et al. (2004).

Table 2.4: Spectral fit parameters

Model	Γ	N_H^a	z_{line}	σ (keV)	EW (eV)	χ^2/d.o.f.
Absorbed power law	1.48±0.07	1.8±0.3	...	...	...	134.6/110
Absorbed power law + Kα line	1.50±0.08	1.7±0.3	$1.20^{+0.06}_{-0.02}$	$0.28^{+0.15}_{-0.10}$	350^{+109}_{-103}	94.8/107
Absorbed power law + Kα line	1.52±0.09	1.7±0.3	1.146(f)	$0.6^{+0.3}_{-0.4}$	434^{+179}_{-193}	104.4/108

^{a} units of 10^{22} cm^{-2}; (f) fixed parameter

2.3.3   Average spectra as a function of redshift

The hypothesis that strong obscuration is ubiquitous among high X/O sources could be quantified once a redshift estimate is available.

In the *CDFS*, after a careful check of the optical X–ray associations which were found to be discrepant between the published X-ray and optical catalogues (Giacconi et al. 2002; Alexander et al. 2003; Szokoly et al. 2004; Zheng et al. 2004), we have considered 28 photo–z, in addition to the 15 spectroscopic redshifts. Most of them (25) have been

Table 2.5: Redshift values for each redshift bin: in col. 1 the mean redshift weighted by the counts of the sources in each bin, in col. 2 and 3 the maximum and minimum redshift of the sources in each bin.

	mean z	min z	max z
CDFS	0.80	0.36	0.99
	1.15	1.016	1.32
	1.68	1.51	1.99
	2.46	2.19	2.942
	3.12	3.064	3.66
CDFN	0.49	0.474	0.52
	1.09	0.986	1.146
	1.46	1.25	1.609
	2.27	1.93	2.52

selected from the Zheng et al. (2004) compilation requiring a quality flag ≥ 0.5 [6], two from the COMBO–17 survey (Wolf et al. 2004) and for one further object, though the photo–z quality flag is 0.3, the detection of an iron line at the same redshift (Gilli, private communication) makes us confident on the redshift estimate. Five sources satisfying the quality–flag criterion have been excluded due to the extremely large errors quoted by Zheng et al. (2004). In the *CDFN* we consider all the available redshifts, 5 spectroscopic plus 12 reliable photo–z (according to Barger et al. 2003) computed with the BPZ code. Not surprisingly, the sources without a redshift measurement are, on average, optically fainter (most of them with R>25). For two sources in the *CDFN* a reliable redshift estimate has been obtained directly from the X–ray data thanks to the detection of a Kα line (see Sect. 2.3.2).

All the redshifts considered for the spectral analysis are reported in column 8 of Table 2.1 and in column 7 of Table 2.2, along with a flag in column 9 and 8, respectively (phot = photometric, spec = spectroscopic, Kα = iron line).

The 62 sources with spectroscopic (20), photometric (40) and X–ray (2) redshift were subdivided in 9 redshift bins, 5 for *CDFS* and 4 for *CDFN* (see Table 2.5 for details). Each bin is centered at the redshift value obtained by weighting the source counts for a given interval.

Stacked spectra of the sources in each redshift bin were extracted and fitted with a a

---

[6]A quality flag 0.5 means that two independent codes (the BPZ–Bayesian Photometric Redshift estimation, Benitez 2000; HyperZ, Bolzonella et al. 2000) return consistent values.

Table 2.6: Spectral fit parameters of the spectra in redshift bins obtained with a power law model plus intrinsic absorption at the mean redshift (the two entries for each bin correspond to a fit with Γ free to vary and to a fit with Γ=1.8).

	z^a	number of sources	Γ	$N_H{}^b$ (1)	χ^2/d.o.f.
CDFS	0.80	9	1.29 ± 0.09	$0.44^{+0.31}_{-0.24}$	117.0/111
			1.8	1.32 ± 0.23	144.0/112
	1.15	6	$0.90^{+0.08}_{-0.11}$	$2.56^{+1.19}_{-1.11}$	76.7/74
			1.8	8.39 ± 0.8	147.1/75
	1.68	12	1.41 ± 0.06	$1.51^{+0.58}_{-0.48}$	184.7/161
			1.8	$3.29^{+0.41}_{-0.39}$	218.3/162
	2.46	12	$1.35^{+0.11}_{-0.13}$	$12.98^{+3.23}_{-2.52}$	97.1/102
			1.8	$19.98^{+2.51}_{-2.26}$	114.1/103
	3.12	4	$1.20^{+0.12}_{-0.14}$	$8.86^{+4.93}_{-3.57}$	44.6/50
			1.8	$20.62^{+4.20}_{-3.65}$	65.0/51
CDFN	0.49	3	1.23 ± 0.12	$1.39^{+0.48}_{-0.26}$	83.6/80
			1.8	$2.48^{+0.28}_{-0.26}$	103.4/81
	1.09	4	1.18 ± 0.06	$2.74^{+0.43}_{-0.34}$	286.6/190[c]
			1.8	5.54 ± 0.36	403.4/191[c]
	1.46	6	1.58 ± 0.05	$5.62^{+0.60}_{-0.50}$	278.7/215
			1.8	$6.92^{+0.38}_{-0.39}$	295.9/216
	2.27	6	0.98 ± 0.15	$4.32^{+2.75}_{-2.00}$	72.6/63
			1.8	$12.91^{+3.06}_{-2.55}$	104.9/64

[a] Mean value weighted by the counts of the sources in each bin. [b] Units of 10^{22} cm^{-2}. [c] The statistical quality of the fit is bad due to the presence of a strong Fe kα iron line at E=2.9 keV (Comastri, Brusa & Civano 2004) and to another iron line at E$\simeq$3.0 keV.
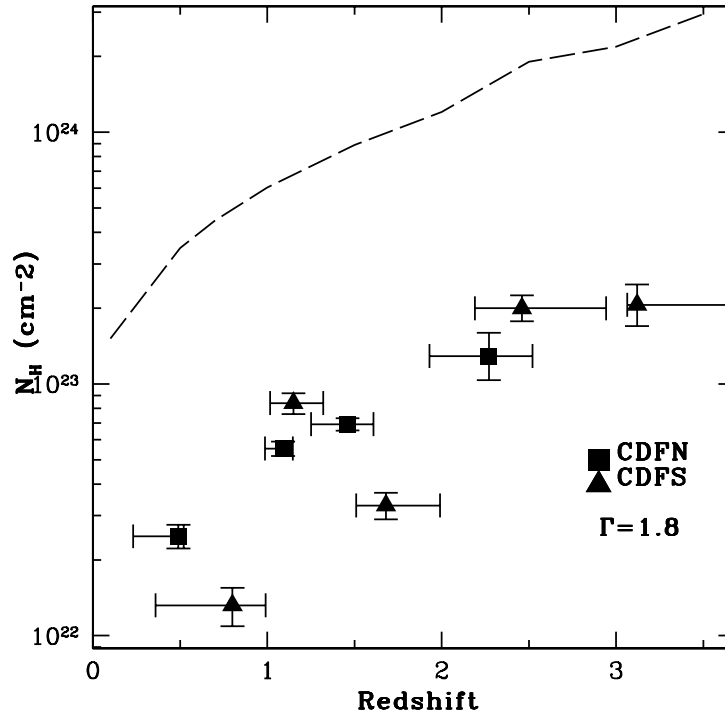
Figure 2.10: Intrinsic N_H rest frame distribution for the stacked spectra in different redshift bins. Symbols as in figure 2.5. The dashed line represents the detection limit obtained by the simulations described in Section 4.3.

power–law model plus intrinsic absorption at the mean redshift.

At first, N_H and Γ were free to vary, then the power–law slope has been fixed to Γ=1.8 in order to better constrain the intrinsic absorption column density. The 95% confidence level errors on the photo–z of eight *CDFS* sources is larger than the bin width. We have verified that excluding these sources does not significantly modify the results and thus all of them were included and assigned at the redshift bin corresponding to the best fit photo–z. The best–fit N_H values are reported in Table 2.6, and plotted in Figure 2.10.

The results in both fields unambiguously confirm that high X/O sources are highly obscured with rest–frame column densities larger than 10^{22} cm^{-2}. The average value of the column density at $z \simeq 3$ is of the order of 2×10^{23} cm^{-2}. As an independent check, the individual spectra of the brightest objects, spread over the entire redshift range and with enough counts (> 200) to perform moderate–quality spectral analysis, have been fitted with a Γ=1.8 power–law plus rest–frame absorption. In all the cases the fitted N_H is consistent with the value obtained for the stacked spectrum in the corresponding redshift bin.

A clear trend is evident in Fig. 2.10 suggesting an increase of the average column density towards high redshifts. Such a correlation might well be due to a selection effect. Obscured sources at low redshift could have been missed simply because were too faint.

At higher redshifts, the photoelectric cut–off is moved towards lower energies where the *Chandra* effective area is higher, favouring the detection of higher column densities.

In order to verify whether the observed trend is due to a selection effect, extensive Montecarlo simulations have been performed using the *fakeit* routine within *XSPEC*. A power–law spectrum with Γ=1.8, normalized to encompass the observed range of 2–8 keV fluxes, is simulated for different values of the column density ($10^{22-23.5}$ cm^{-2}) over the redshift interval z=0.1–3.5. For each redshift, the maximum N_H value for which a source could be detected at the faintest flux of our sample has been computed. The results (Fig. 2.10) indicate that obscured sources ($N_H \sim 10^{23}$ cm^{-2}) at relatively low redshift ($z \simeq 1$) would have been detected in the deep *Chandra* field. It should be noted that the dashed curve in Fig. 2.10 would be shifted towards lower N_H values, if the power law slope is left free to vary in the range $\Gamma \simeq 1$–1.4. However, also the observed N_H value, with Γ free to vary, moves to lower values (see Table), leaving almost unchanged the bias estimated with Γ=1.8.

As a further check, we have simulated the expected distribution of counts in the very hard 4–7 keV band for the range of column densities and redshifts considered here. The results indicate a change in the number of counts of $\sim$10–20% (at most) at the highest column densities and lowest redshifts. Overall, this count distribution is consistent with the one observed in the 4–7 keV energy range in the stacked spectra of different redshift bins. Although we are confident that the present findings are not strongly biased against low–redshift absorbed sources, such a possibility cannot be completely ruled out. Indeed, the simulations suggest that the sensitivity limit to absorption decreases, as expected, at low redshifts. As a result, for a given column density ($N_H \geq 10^{22}$ cm^{-2}), faint sources are more easily missed if they are at lower redshift.

2.4   Discussion

The results of spectral analysis of a large sample of high X/O sources in the *Chandra* deep fields leave no doubts about the presence of X–ray absorption. Similar results have been recently obtained for a sample of high X/O sources detected at brighter fluxes ($> 10^{-14}$ erg cm^{-2} s^{-1}) in the *HELLAS2XMM* survey (Perola et al. 2004; Comastri & Fiore 2004).

The shape of the stacked spectrum in both *CDFN* and *CDFS* and the residuals with respect to a single power–law fit are consistent with those expected by obscured sources spread over a range of redshifts. The very hard average slope $\Gamma \simeq 0.9$–1.0 in the *CDFS* and $\Gamma \simeq 0.6$–0.9 in the *CDFN* is consistent with that obtained for a sample of hard (2–7 keV) and ultrahard (4–7 keV) selected sources ($\Gamma \simeq 1.0$–1.1) in the *Chandra* Groth Strip survey (Nandra et al. 2004). Surprisingly, the fraction of the high X/O sources in the *Chandra* deep fields (about 23%) is comparable to that (about 25%) of hard spectrum objects in the Groth Strip sample. The most straightforward explanation would imply that most of the hard sources in the Groth Strip survey have high X–ray to optical flux

ratios. Such a possibility could be easily tested thanks to the multiband imaging including HST/ACS observations. It is also worth noting that the average spectrum of the sources in the Groth Strip survey has been computed with the hardness ratio technique and thus affected by larger uncertainties.

  Most interesting, the average spectral shape of our sample as a function of the hard X–ray flux is approximately constant. Such a behaviour is significantly different from the well established trend observed in the same *Chandra* fields (Rosati et al. 2002; Alexander et al. 2001, 2003) without a specific selection on the X–ray–to–optical flux ratio. Given that fainter X–ray sources are most likely at higher redshifts, the observed shape can be explained if more distant sources are, on average, more obscured. Indeed, such a trend seems to be present for those sources (about half of the sample) for which a redshift estimate has been considered. Though potentially interesting, such a correlation needs to be confirmed by a larger sample, with a larger fraction of spectroscopic identification, allowing to keep the observational biases under control. Unfortunately, the spectroscopic identification of obscured high X/O sources is already challenging the capabilities of large 8–10 m class telescopes. An alternative method to multiband optical/near–infrared photometry and Fe Kα line X–ray spectroscopy has been put forward by Fiore et al. (2003). The X/O ratio and 2–10 keV luminosity of a large sample of spectroscopically identified hard X–ray selected sources follow a linear relation :

$$\log L_{2-10} = \log f(2-10keV)/f(R) + 43.05. \qquad (2.1)$$

The correlation holds for optically obscured sources (i.e., non broad–line AGN) and has been calibrated combining the optical and X–ray data of the *HELLAS2XMM* survey with well defined subsamples of identified sources in the deep *Chandra* fields at fluxes larger than 3×10^{-15} erg cm^{-2} s^{-1}, and optical magnitudes brighter than the R≃24–25. Though characterized by a not–negligible dispersion (about 0.4 dex), this relation can be used to compute X–ray luminosities, and then redshifts of obscured sources, from the observed X/O value. The accuracy in the redshift estimate ("X–photo–z"; Fiore 2004) is fairly good [$\sigma(\Delta z/(1+z)) \simeq 0.2$].

  In order to check whether the Fiore et al. relation could be used to infer redshifts for the unidentified sources in our sample, we have plotted the X/O values and luminosities for the 61 sources[7] in our sample with redshift information. The two panels of Fig. 2.11 show the unabsorbed 2–10 keV luminosity, calculated from the published 2–8 keV counts and exposure times (Alexander et. al 2003) assuming a power–law model with Γ=1.8 plus Galactic absorption, versus the X/O ratio for sources brighter and fainter of R=25, respectively. In each panel, sources with spectroscopic, photometric and X–ray redshifts are plotted with different symbols and the Fiore et al. relation is also reported. While for the bright subsample there is a fairly good agreement, though characterized by a significant dispersion, with the correlation, at fainter magnitudes high X/O sources have

---

[7]We did not include 1 broad line AGN because the Fiore et al. correlation does not hold for Type 1 AGN.
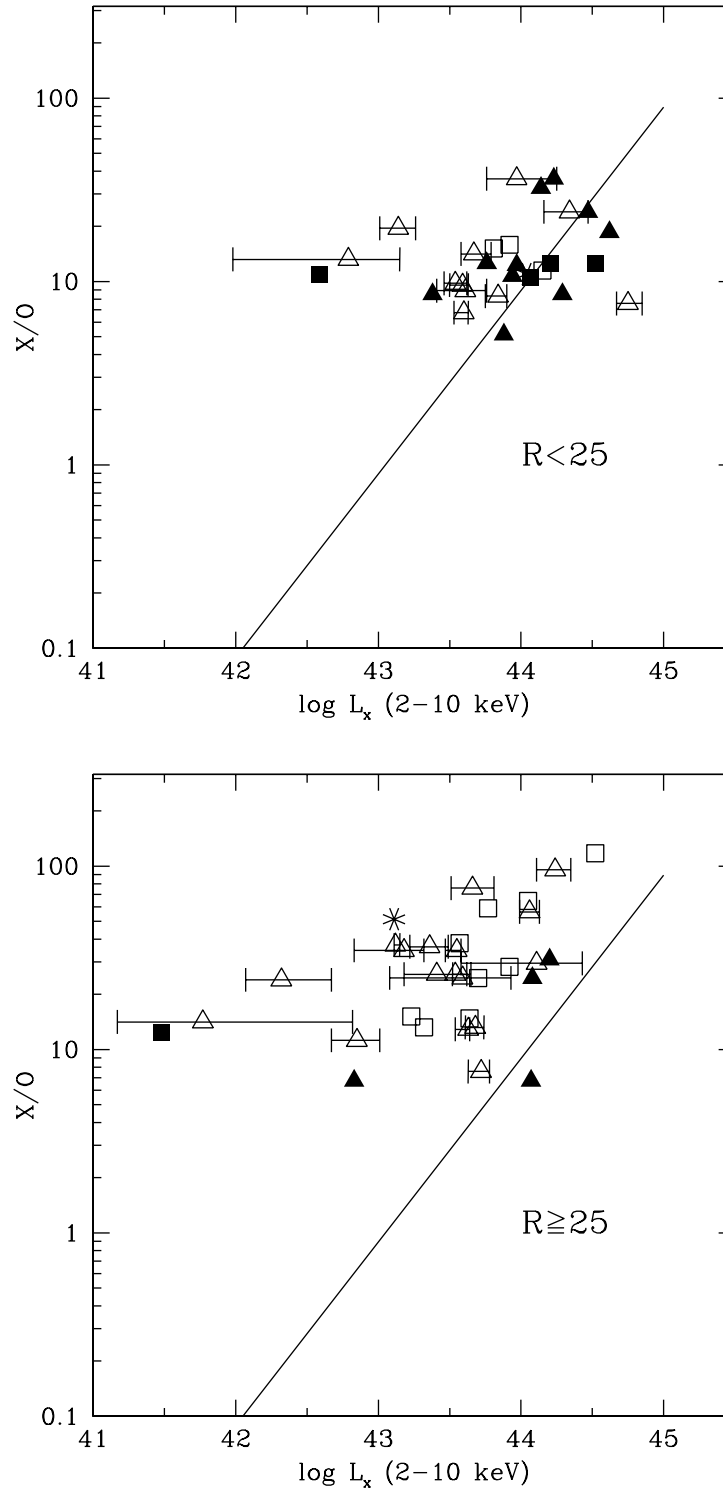
Figure 2.11: The X–ray–to–optical flux ratio as a function of the 2-10 keV deabsorbed luminosity for the 61 sources with redshift information (*CDFN* = squares, *CDFS* = triangles, filled symbols = spectroscopic redshift, open symbols = photometric redshift, stars = redshift trough iron line). The error bars corresponds to the quoted uncertainties on the photo-z. Top panel: optically "bright" sources (R<25). Bottom panel: optically faint objects (R≥25). The extrapolation of the Fiore et al. (2003) relation is also reported (continuous line).

lower luminosities than expected. Such a discrepancy, already noted by Bauer et al. (2004) and Barger et al. (2005), may indicate that the relative contribution of the host galaxy emission to the measured optical luminosity at $R > 24$–25 is different than at brighter magnitudes. As a consequence, some caution should be used when the Fiore et al. relation is extrapolated to optically faint objects.

The X/O vs. X–ray luminosity relation has been employed by Padovani et al. (2004) to search for Type 2 quasars combining deep *Chandra* exposure with HST/ACS imaging within the GOODS project. Almost by definition, a large fraction of the candidate Type 2 quasars ($N_H > 10^{22}$ cm^{-2}, $L_X > 10^{44}$ erg s^{-1}) of the Padovani et al. (2004) sample have X/O > 1. Given that most of them have faint R–band magnitudes, the high space density of Type 2 quasars obtained by Padovani et al. (2004) should be considered as an upper limit.

Although the observed trend seems to indicate that the X/O vs. luminosity relation does not hold at $R > 25$, it is important to note that at faint optical magnitudes the probability to find by chance a galaxy in the X–ray error box increases dramatically (i.e. up to about 0.25–0.30 for R=26 and an error circle radius of 2 arcsec, without considering source clustering). Furthermore, photo–z estimates often involve the determination of the magnitudes of the sources in images of very different quality (e.g., space– versus ground– based telescopes) and, as a consequence, are affected by systematic errors (see Zheng et al. 2004 for a discussion on the accuracy of redshift estimates in the *CDFS*).

2.5 Summary

The most important results obtained from the spectral analysis of a large sample of high X/O sources selected from *Chandra* deep fields can be summarized as follows:

- The average slope obtained by fitting the stacked spectra with a single power–law model in both *CDFN* and *CDFS* is extremely flat ($\Gamma \sim 1$). The shape of the residuals strongly suggests that such a hard slope may well be the result of the superpositions of sources with different intrinsic column densities over a broad range of redshifts.

- The average slope of the stacked spectrum is almost independent from the 2–8 keV flux. The high X/O sources represent the most obscured component of the X–ray background. Their spectra are harder ($\Gamma \sim 1$) than any other class of sources in the deep fields and also of the XRB spectrum.

- The redshift estimates, mainly obtained by multiband optical and near–infrared imaging, available for about half of the sample, allowed us to investigate the amount of intrinsic absorption in the stacked spectra for a few redshift ranges. A trend of increasing absorption with redshift has been uncovered ($N_H = 10^{22-23.5}$ cm^{-2}).

While observational biases could not be completely ruled out, extensive simulations suggest that the observed trend may well be real. Also, the rather constant hard spectrum over more than two orders of magnitude of X–ray flux is consistent with such a behaviour.

- Two new X–ray redshifts, obtained from the Kα iron line, have been discovered. One object satisfy the criterion of an X–ray Type 2 QSO.

- Though the X/O ratio is a fairly good estimator of the source luminosity and redshift (Fiore et al. 2003), at faint optical magnitudes (R> 25) a departure from the X/O vs. luminosity relation is emerging.

Chapter 3

Multiwavelength analysis of optically faint sources

O n the basis of the unified schemes, Type 2 quasars are expected to be optical narrow-line objects, X-ray luminous ($> 10^{44}$ erg s^{-1}) and with substantial ($N_H > 10^{22}$ cm^{-2}) absorption. Even though the optical identification of X-ray sources has been pushed to faint optical magnitudes, only a handful of "bona fide" Type 2 QSOs has been discovered so far (e.g., Norman et all. 2002; Stern et al. 2002; Fiore et al. 2003; Caccianiga et al. 2004; Gandhi et al. 2004, Perola et al. 2004, Szokoly et al. 2004; Mainieri et al. 2005; Maiolino et al. 2006; Vignali et al. 2006). A large fraction of faint X-ray sources does not show optical emission lines, suggesting that Type 2 quasars may be different in the optical band from what expected. Moreover the spectroscopic identification of these faint objects is very difficult, time consuming and challenging the capabilities of current 8-10m class ground-based telescopes. A powerful tool to detect high-luminosity, highly obscured sources is the selection on the basis of the X/O>1, as already discussed in the previous Chapter (§2). The combination of medium-deep X-ray observation with K-band imaging offers a further method to pick up this elusive population. Among hard X-ray sources, one must select those with counterparts with extremely red ($R-K$ >5, EROs) color, which is an indication of high redshift (z> 0.8) and obscuration. Brusa et al. (2005) and Severgnini et al. (2005) convincingly demonstrated that the combination of these two selection criteria is a powerful tool to select Type 2 quasar.

Thanks to the COSMOS multiwavelength database, it has became possible to build up a large and homogeneously selected sample of X-ray emitting EROs. The combination of optical, near-infrared and X-ray data of a complete sample of EROs is crucial to study the relationship between EROs, high X/O and QSO2 and to quantitatively investigate the link between the formation of massive ellipticals and the onset AGN activity.

3.1 The XMM-COSMOS sample

The XMM-COSMOS X-ray source catalogue comprises 1390 point–like sources detected over an area of $\sim 2\ deg^2$ in the the first–year of XMM–*Newton* observations of the COSMOS field (23-field catalog; Hasinger et al. 2007; Cappelluti et al. 2007). A total of 1281 sources are detected in the soft band (0.5-2 keV), 724 in the medium band (2-4.5 keV), and 186 in the hard band (4.5-10 keV), down to limiting fluxes of 7.2×10^{-16} erg cm^{-2} s^{-1}, 4.7×10^{-15} erg cm^{-2} s^{-1} and 9.7×10^{-15} erg cm^{-2} s^{-1} respectively. The minimum number of net counts for the detected sources is $\sim$21, 17 and 27 in the three bands, respectively. The number of sources detected only in the 0.5–2 keV, 2–4.5 keV, 4.5–10 keV bands are 661, 89 and 3, respectively.

Brusa et al. (2007) presented the optical identification (the 12-field catalogue) of the 695 X–ray sources detected in the first 12 fields (1.3 deg^2). The same process for the optical identification described in Brusa et al. (2007) has been applied to the 23-field sample. The identification process is based on the "likelihood ratio" technique (Sutherland & Saunders 1992; Ciliegi et al. 2003; Brusa et al. 2005; 2007). As a first step in the identification process, the I–band CFHT/Megacam catalog (Mc Cracken et al. 2007) has been used, which, although slightly shallower than other available data (e.g., the Subaru B,g,V,R,I and z photometric data, see Capak et al. 2007), has the advantage of having reliable photometry even at bright magnitudes ($I_{AB} \lesssim 19$), where the Subaru photometry starts to be significantly affected by uncertainties due to saturation. Then, the optical counterparts have been cross–correlated with the multicolor photo-z catalog (January 3rd 2006 release; Capak et al. 2007). As a second step, the likelihood has been performed using as input catalog the K-band (KPNO/CTIO) data extracted from the multicolor catalog. The main advantage of using also this near-infrared catalog is due to the fact that the X-ray-to-near-infrared correlation for AGN is much tighter than the one in the optical bands (Mainieri et al. 2002; Brusa et al. 2005). Moreover, although the available K–band data are shallower than the optical ones, their use is potentially important to find the reddest optical counterparts, which are a not negligible fraction of the identifications of faint X–ray sources (Alexander et al. 2001). As a third step, a visual inspection of the *Spitzer*/IRAC (Sanders et al. 2007) cut-outs around the X–ray sources has been performed. The identifications have been further divided in "reliable[1]" and "ambiguous": 89% have a reliable identification, 7% have an ambiguous identification, while 4% still remain unidentified.

At the time of writing, the XMM-COSMOS observations have been completed and the 53-field catalogue has been released to the XMM-COSMOS collaboration along with the optical identification of the sources. A total of 1749 pointlike sources have been detected

---

[1]In this class are included the sources with $I_{AB} < 16$, the sources for which either there is only one object with LR> LR_{th} (where LR_{th} is the chosen threshold for the maximum likelihood) or the ratio between the highest and the second highest LR value in the I or K–band is greater than 3, and the sources identified only in the K–band; see Brusa et al. (2007) for a detailed description of the identification method.
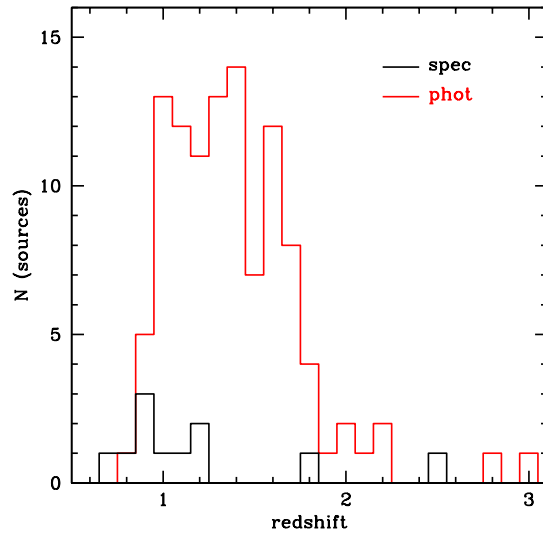
Figure 3.1: Redshift distribution of the X-ray emitting ERO sample; the red line is the distribution of the sources with photometric redshift (108), while the black line is the distribution of the sources with spectroscopic redshift (11).

in the 0.5-2 keV (1638 sources), 2-4.5 keV (1129 sources) and 4.5-10 keV (374 sources) bands. The process of optical and NIR identification found 1441 secure sources (82% of the sample), 287 ambiguous sources (16% of the sample) and 21 unidentified sources (2 % of the sample).

The results reported in the following concern samples selected in the 53-field catalogue.

3.2   XEROs sample selection

In order to study the multiwavelength properties of presumably obscured AGN, a sample of hard X–ray sources with reliable counterparts and extremely red colors ($R - K > 5$ in Vega magnitude) has been selected from the 53-field catalogue. A total of 119 hard X–ray emitting EROs (hereafter XEROs) are included in this sample with a magnitude limit $K_{Vega} \sim 19.2$; to date this is the largest sample of XEROs with homogenous multiwavelength coverage. These XEROs consitute $\sim 10\%$ of the total hard X-ray detected sample with reliable counterparts, while high X/O sources constitute the 20% of the hard sample. The multiwavelength available data include: u band photometry from the CFHT/Megacam catalogue (Mc Cracken et al. 2007), the Subaru B, g, V, R, I and z band photometry (Capak et al. 2007), the K-band photometry (KPNO/CTIO; Capak et al. 2007), the ACS catalogue and images (Leauthaud et al. 2007; Koekemoer et al. 2007) and the *Spitzer* (IRAC and MIPS) catalogues (Sanders et al. 2007).

Photometric redshifts are available for all the sources (Mobasher et al. 2007), while spectroscopic redshifts are available for 11 sources from the Magellan/IMACS observation campaign (Trump et al. 2007). The majority (98/119) of the sources are
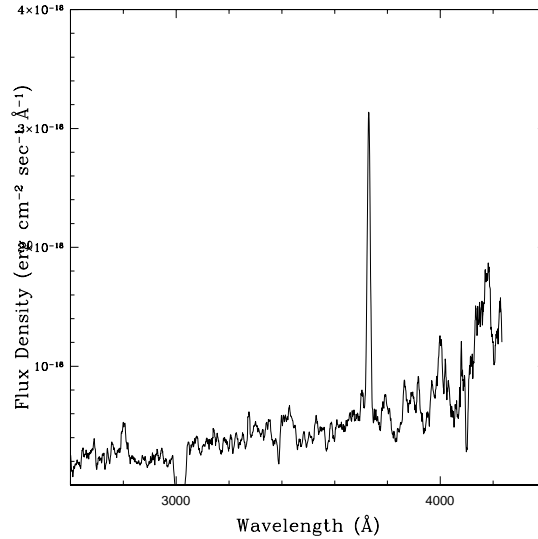
Figure 3.2: Optical spectrum of source XID 43 at $z = 1.162$ is shown in the rest frame. A strong OII line at 3727 $\mathring{A}$ is visible along with a MgII line at 2800 $\mathring{A}$.

in the range $z = 1 - 1.8$ (Fig. 3.1). The photometric redshifts, obtained through the fitting of the optical photometry using galaxy templates, provide a good estimate of the redshift of our sources, since their optical continuum is dominated by the host galaxy light. The few optical spectra available show either the presence of emission lines typical of AGN (MgII, O[III] and FeII lines) or that of a strong galaxy continuum, and confirm the reliability of the photometric redshifts. As an example, the optical spectrum of source XID 43 at $z = 1.162$ is shown in Fig. 3.2. A strong OII line at 3727 $\mathring{A}$ is visible along with a faint MgII line at 2800 $\mathring{A}$. We note, however, that the quality of the optical spectra available at present for our XEROs is much lower than that of XID 43.

The main properties of the sources are reported in Table 3.1, namely: the X-ray identification number, the X-ray right ascension and declination, the hard X-ray flux, the hardness ratio, the R band magnitude (in the AB system), the $R - K$ color (in the Vega[2] system), the X/O ratio, the hard X-ray luminosity, the redshift and final a flag on the redshift nature (photometric=1, spectroscopic=2) .

3.3   X–ray to optical properties

The R-band magnitudes versus hard X-ray fluxes of XEROs (red circles) are reported in Figure 3.3 (left panel), along with the sources of the complete hard sample (black circles). Spectroscopically identified broad-line AGN (BLAGN) are reported as blue circles. The average X-ray-to-optical ratio of XEROs ($\langle$X/O$\rangle$=1.2) is significantly higher than that of spectroscopically identified BLAGN ($\langle$X/O$\rangle$=0.06), in agreement with previous findings

---

[2]The conversion from the Vega to AB sistem are $R_{Vega} = R_{AB} - 0.2$ and $K_{Vega} = K_{AB} - 1.8$
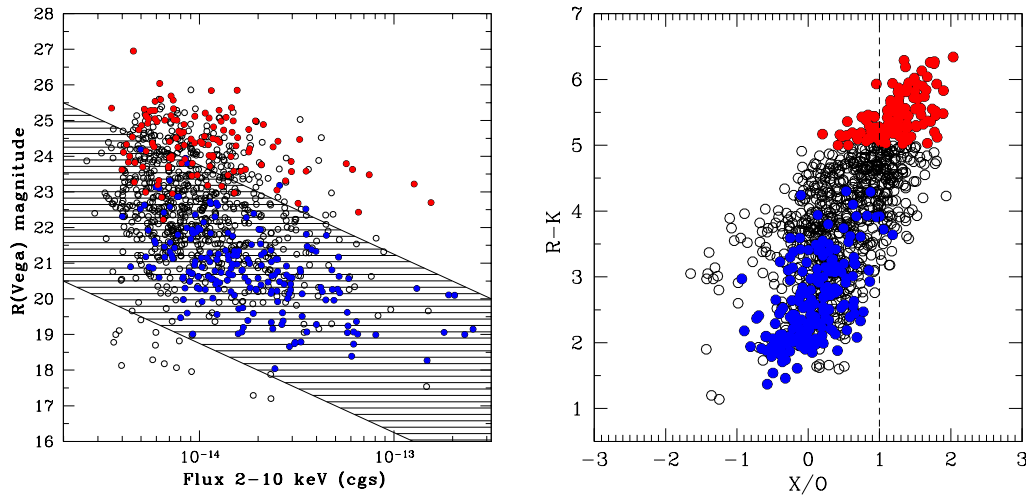
Figure 3.3: Left: R-band magnitude vs. hard X-ray flux for all the hard XMM-COSMOS sample with reliable counterparts; red circles are the XEROs; blue circles represent the spectroscopically identified BLAGN. The dashed region is that defined in the introduction, i.e., the locus occupies by optically selected AGN. Right: $R - K$ color vs. the X/O for all the hard detected XMM-COSMOS sample with reliable counterparts. Simbols are as in the left figure. The vertical dashed line represents the X/O=1 limit.

(Brusa et al. 2005; Georgantopoulos et al. 2006). Moreover, about 75% of the XEROs (88/119) belong to the high X/O population (right panel of Fig. 3.3). There is a strong correlation between the X/O and red color, in the sense that most of the reddest sources have high X/O (right panel of Fig. 3.3).

In the previous Chapter it has been shown that the high X/O is often associated with significant obscuration. Given the low counting statistic of the sources, it is impossible to perform spectral analysis on individual objects, and given the high background of the XMM–*Newton* data, the stacking analysis, similarly to that performed with the *Chandra* data in the deep fields (Chapter 2), is much more uncertain. The hardness ratio (HR) may provide a first rough indication of the shape of the sources spectrum. HR is defined as $HR = (H - S)/(H + S)$, where H is the number of counts in the hard band (2-10 keV) and S is the number of counts in the soft (0.5-2 keV) band. Mainieri et al. (2007) found a clear correlation between the hardness ratio and the intrinsic column density derived from a proper spectral analysis for a selected sub-sample of sources belonging to the XMM-COSMOS 12-field sample. They also found that HR=–0.3 is an appropriate value to separate obscured ($N_H > 10^{22}$ cm^{-2}) and unobscured sources (see their Fig. 11). Therefore, although one has to remember that the HR is a function of redshift, it is still possible to use HR for statistical studies. In Figure 3.4 (left), the HR versus the X/O of all the hard detected sample is shown (symbols as in Fig. 3.3). The average hardness ratio for XEROs is $\langle HR \rangle \sim$–0.07, significantly higher than that of BLAGN ($\langle HR \rangle \sim$–0.6) and well above the mean HR threshold defined by Mainieri et al. for obscured sources. It means that XEROs are harder than BLAGN, in agreement with the findings of the X-ray
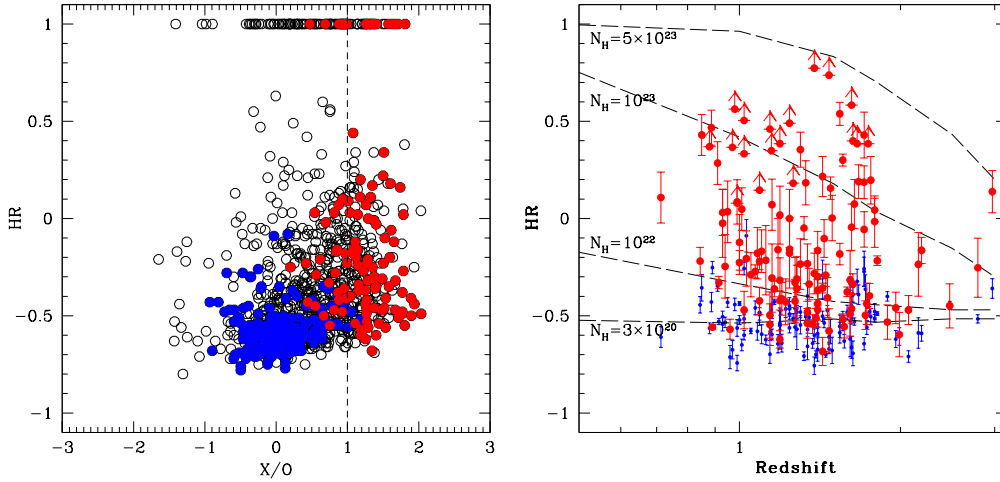
Figure 3.4: Left: Hardness ratio vs. X/O of all the hard source sample with reliable counterparts; simbols are as in Figure 3.3. The vertical dashed line represents the X/O=1 limit. Right: HR distribution as a function of redshift for all the XERO sample (red circles) along with the BLAGN sample (blue circles). The dashed lines represent different column densities ($N_H = 3 \times 10^{20}, 10^{22}, 10^{23}, 5 \times 10^{23}$ cm^{-2}), assuming a power-law spectrum with $\Gamma = 1.8$.

spectral analysis discussed in Chapter 2, and on average are obscured in the X-ray band. However, there is a conspicuous population of sources with high X/O and hard colour not belonging to the EROs sample. Indeed, as found in previous works, red color and high X/O are strongly coupled with obscuration, but not all X–ray obscured sources are extremely red.

In order to derive an estimate of the rest-frame column density for each source, we performed spectral simulations with XSPEC to convert HR into N_H taking into account the redshift. The input parameters of the simulations are a power-law spectrum with slope $\Gamma = 1.8$, column density in the range $N_H = 3 \times 10^{20} – 10^{24}$ cm^{-2} and redshift in the interval $z = 0.2 – 3$. In the right panel of Figure 3.4, XEROs and BLAGN are compared with the iso-N_H curves as a function of redshift obtained from simulations. In the figure, upwards pointing arrows represent the limits for the sources undetected in the soft band. At the face value, the inferred N_H values of XEROs are significantly higher than that of BLAGN, as expected. About 70% (84/119) of XEROs are consistent with intrinsic column densities in excess of 10^{22} cm^{-2}, and actually are heavily obscured AGN. This study statistically confirms previous works based on HR analysis (Alexander et al. 2002) and spectral analysis (Vignali et al. 2003; Willott et al. 2003; Stevens et al. 2003; Ghandi et al. 2004; Severgnini et al. 2005; Brusa et al. 2005) and unambiguously indicates that large columns of cold gas are common in X-ray emitting EROs. However, there is a non negligible fraction (30%, 35/119) of sources with negligible X-ray absorption.

For all the sources we have also estimated the 2-10 keV luminosities from the observed fluxes. The X–ray luminosities are corrected for the effect of absorption derived as
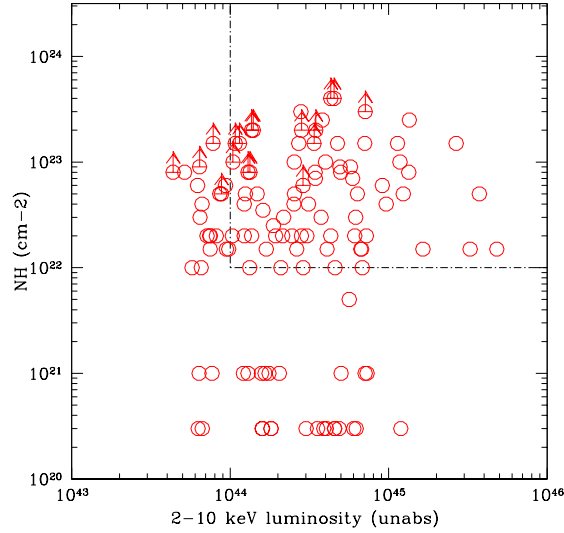
Figure 3.5: Logarithm of the absorbing rest frame column density versus the logarithm of the absorbed X–ray luminosity in the hard band. The boxy region indicates the locus of QSO2 ($N_H > 10^{22}$ cm^{-2} and $L_X > 10^{44}$ erg s^{-1}).

described above. Given the high redshift and the relatively large X–ray fluxes of the sources, it is not surprising that 78% (93/119) of the sources have high X–ray luminosity $L_X > 10^{44}$ erg s^{-1} (see Fig. 3.5) and are therefore in the quasar regime. Moreover, half (55%, 64/119) of the sources in our sample show $N_H > 10^{22}$ cm^{-2} and $L_X > 10^{44}$ erg s^{-1} and are thus classified as Type 2 quasars (Fig. 3.5).

3.4 Mid - infrared properties

While the $R - K$ colors of our objects are typical of red elliptical galaxies and dusty systems at high redshift (e.g., Cimatti et al. 2002), extending the photometric coverage to the *Spitzer* bands may give additional clues on the properties of our sources. According to Lacy et al. (2004), most of the luminous IRAC-selected AGN occupy a well defined region in a IRAC color-color plot ($f_8/f_{4.5}$ vs. $f_{5.8}/f_{3.6}$, see solid line in Fig. 3.6). A similar conclusion is reached by Stern et al. (2005), Hatziminaoglou et al. (2005) and Barmby et al. (2006) using a different combination of IRAC colors. AGN occupy preferentially this region because of their red power-law mid-IR SED, while normal galaxies lie in the blue part of the diagram, clustering around $f_8 - f_{4.5} = -0.5$ and $f_{5.8} - f_{3.6} = -0.5$. The spectroscopically identified BLAGN (blue circles) are expected to show a steep power-law spectrum and indeed occupy the AGN locus in the IRAC color-color (Fig. 3.6). XEROs occupy a transition region in between the locus of AGN and that of galaxies. For a large fraction of sources the AGN contribution is rising in the mid-IR, while for a non negligible fraction, the AGN light is still invisible or probably mixed with the host galaxy light at the IRAC wavelength (Mignoli et al. 2004; Pozzi et al. 2007).
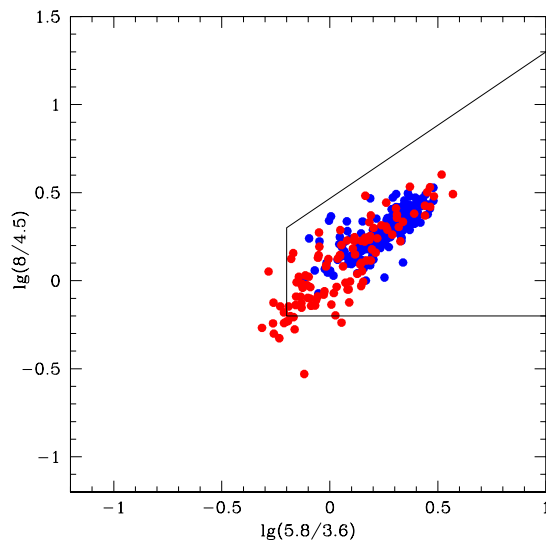
Figure 3.6: *Spitzer* IRAC color - color plot. The solid line denotes the color selection criterion used to pick out luminous AGN according to Lacy et al. (2004). XEROs are plotted as red circles, BLAGN as blue circles.

Therefore, if on one hand the mid-IR diagnostic used by Lacy et al. is efficient for the selection of luminous AGN, on the other hand X-ray selected AGN occupy both red and blue colors, because of the contamination by their host galaxies, especially for the lower luminosity AGN (Barmby et al. 2006).

3.5 Morphology of XEROs

The COSMOS survey was awarded a total of 590 orbits of HST observations to cover the COSMOS field using the Advanced Camera fo Surveys (ACS) Wide-Field Channel (WFC) detector, together with the F814W ("Broad I") filter (Koekemoer et al. 2007). This filter has been chosen in order to obtain the best possible rest-frame morphological information on galaxies at z≥1. The astrometry of all the HST images is accurate to ∼5 milliarcseconds. The images reach a point-source limiting depth AB(F814W)=27.2 (5σ). Since most of the XEROs have very faint magnitude, in the range $I_{AB} = 21 - 26.5$, it is quite difficult to perform a detailed morphological analysis. We have performed a visual inspection of HST cut-outs of all the sources (excluding 15 sources which do not have HST coverage) with the aim to derive a rough classification (i.e., point-like vs. extended). This "eyeball" classification should not be strongly biased by the redshift information, because most of the sources of the sample are within $z = 1 - 1.8$ (Fig. 3.1). The majority of the sample (90%) present extended morphology, and only 10% of the objects in the sample appears point-like. We note that the redshift distribution of the objects classified as point-like is shifted at high redshift: 4 objects are at $z > 2$ (see Fig. 3.1) therefore they could either be high-redshift AGN, or their host galaxy extended emission is very faint

and below the ACS resolution.

3.6   Broad–band Spectral Energy Distributions of XEROs

An important issue in AGN studies is the determination of the global SEDs, over the widest possible frequency range. While the average SED of optically and radio selected bright quasars is well known since more than a decade (Elvis et al. 1994; see also Richards et al. 2006 for an update based on SDSS broad-line quasars), little is still known about the SEDs of X-ray selected AGNs, especially for the obscured ones. The optical continuum in obscured AGN is heavily absorbed by dust and then re-radiated at longer wavelength. Moreover, the obscured sources are generally hosted by galaxies with significant bulge components, making more difficult the characterization of the nuclear emission at the optical and near-infrared wavelengths. Therefore, a reliable estimate of the bolometric luminosities of obscured AGN is limited by the actual capabilities of disentangling the nuclear emission from that of the host galaxy.

In this section, by exploiting the multiwavelength database of the COSMOS survey, we provide an analysis of the SEDs of the XEROs in order to derive their energy distributions cleaned by the host galaxy component, and to understand whether the red colors of XEROs are due to the host galaxy stellar emission or to the dust absorption of the nuclear light.

In the following procedure, we use optical (u, b, g, v, r, i, z, k) and IRAC (3.6, 4.5, 5.8, 8 μm) photometric data. In order to reproduce the observed photometric data, we performed a double-component (host galaxy plus nucleus) fitting parameterized by

$$f_\nu(observed) = A \times f_\nu(host) + B \times f_\nu(nucleus) \, ,$$

where A and B are the relative normalization of the host and nuclear components, that minimize the χ^2. For the latter component, we adopted a Type 1 AGN SED from Elvis et al. (1994) reddened using a suitable dust-reddening law in the form $A_\lambda/E(B-V) = 1.39\lambda^{-1.2}$ (Small Magellanic Cloud, SMC; Prevot et al. 1984) and assuming a grid of extinction values in the range $E(B-V) = 0.1 - 10$ (with steps of $\Delta_{E(B-V)}$=0.01). For the galaxy component, we collected several templates of early-type (Bruzual & Charlot 2003) and starforming (Devriendt et al. 1999) galaxies. The MIPS 24 micron flux density has not been included in the fitting as, at the time of writing, the coverage of the COSMOS field is limited to shallow fluxes. Nevertheless, the MIPS flux density has been reported in each plot with the aim to check the agreement with the extrapolation of the fit at that wavelength.

In the following, we concentrate on the subsample of 63 sources, for which the multiwavelength coverage is such to provide robust results. The global properties (colors,

Figure 3.7: (Left) Rest-frame SEDs of representative XEROs dominated in the K-band by the nuclear component, compared with the best-fit model obtained as the sum (red line) of a host galaxy (early-type or S0 or Sa, dotted line) and a nuclear component, the latter convolved with the extinction law described in the text (dashed line). The MIPS flux density is reported as a downward-pointing arrow if only an upper limit at 24 μm is available. (Middle) The 10"×10" ACS images for each source are presented. (Right) The 20"×20" 3.6μm images with overlaid the 24 μm contours (cyan; courtesy of H. Aussel) are shown. From top to bottom, the SEDs present a decreasing nuclear contribution to the total light.
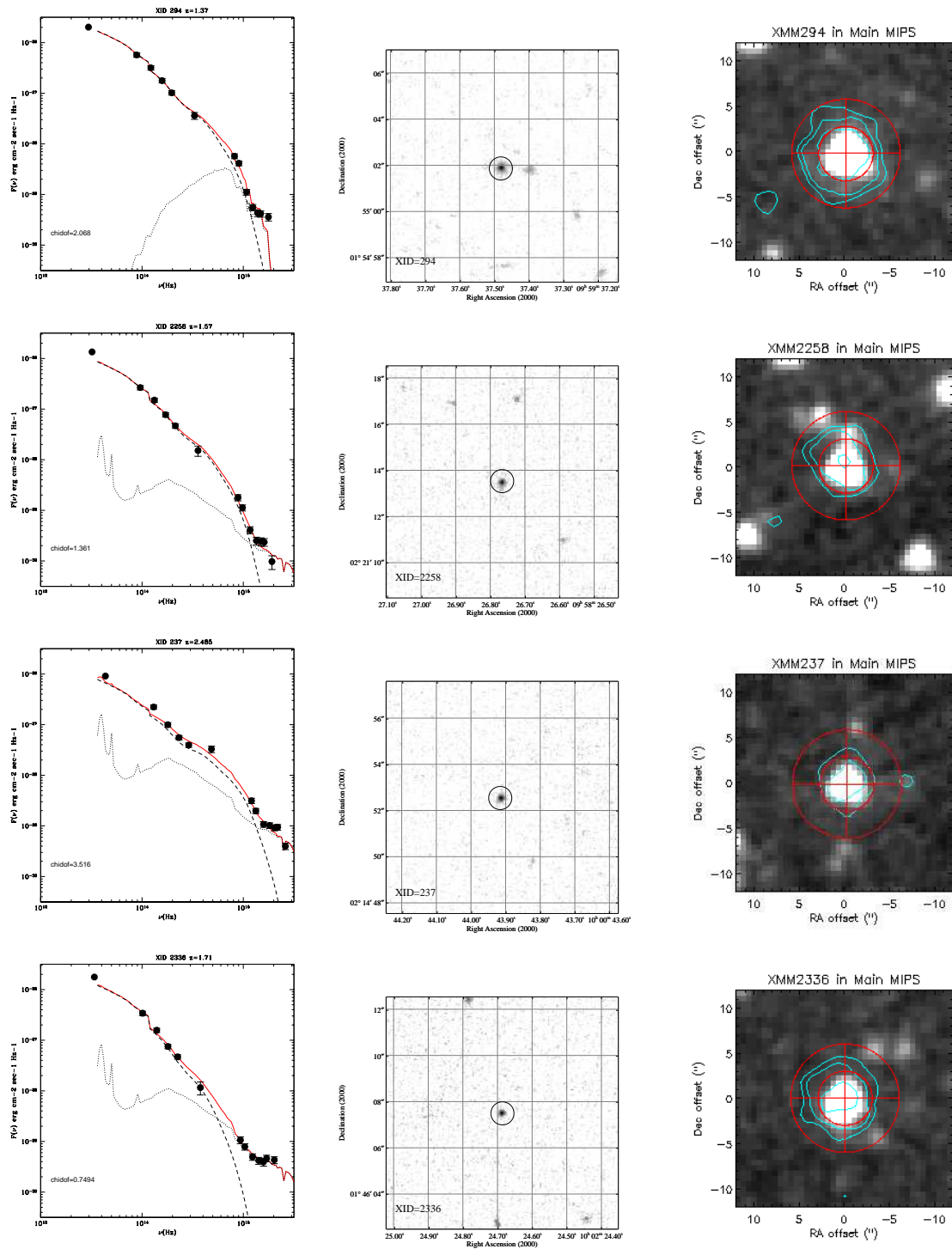
Figure 3.8: (Left) Rest-frame SEDs of representative XEROs dominated in the K-band by the host galaxy component, compared with the best-fit model obtained as the sum (red line) of a host galaxy (early-type or S0 or Sa, dotted line) and a nuclear component, the latter convolved with the extinction law described in the text (dashed line). The MIPS flux density is reported as a downward-pointing arrow if only an upper limit at 24 μm is available. (Middle) The 10"×10" ACS images for each source are presented. (Right) The 20"×20" 3.6μm images with overlaid the 24 μm contours (cyan; courtesy of H. Aussel) are shown.
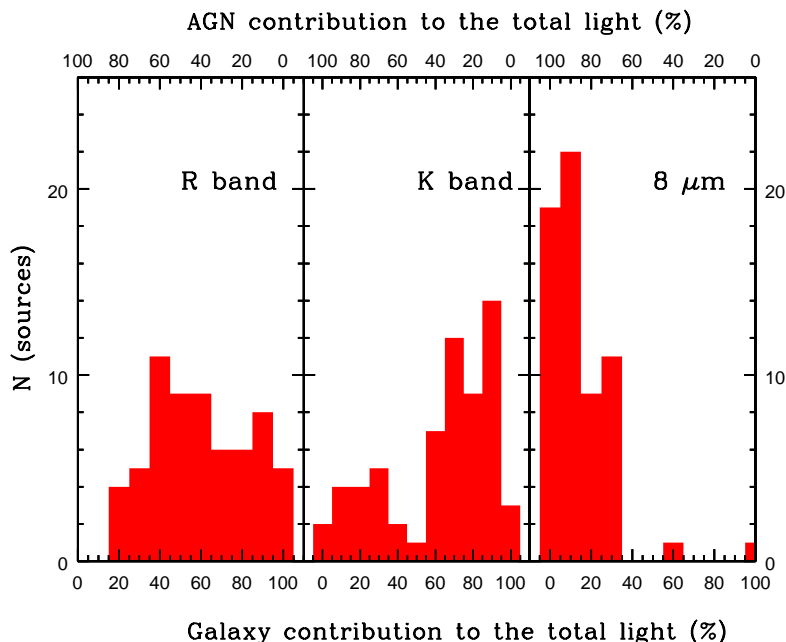
Figure 3.9: Contribution of the nuclear component (upper axis) and of the host galaxy (lower axis) light in three rest frame band (R, K, 8 μm) to the total emission.

redshift distribution, X-ray luminosity, absorption column density) of this subsample reflect the properties of the entire XEROs sample.

The SEDs of a few sources in a f_ν (erg cm^{-2} s^{-1} Hz^{-1}) vs. ν (Hz, rest frame) plot along with 10"×10" postage-stamp ACS and 20"×20" IRAC (3.6μm) images are shown in Figures 3.7 and 3.8. The 24 μm contours from the shallow MIPS observations are overlaid on the IRAC 3.6 μm images (courtesy of H. Aussel). In the left-most panel, the dotted line represents the best-fit galaxy template, the dashed line is the best-fit nuclear template folded with the extinction law and the thick red line is the sum of the two components. In each plot the χ^2_{dof} is reported. The fitting procedure described above provides a good representation of the observed data. The best fit galaxy templates are mostly S0 or Sa, while the average extinction obtained for the nuclear component is $\langle E(B-V) \rangle \sim 0.8$.

Thanks to the procedure described above based on a two-component fitting of the observed SEDs, we were able to estimate the relative contribution of the host galaxy and nuclear component as a function of wavelength. The distribution of percentage contribution to the total light due to the nuclear (upper axis) and host (lower axis) emission is shown in Fig. 3.9 in three rest-frame bands (R, K, 8 μm). Given the relatively narrow redshift range, we are looking at almost the same part of the SED for all the sources. The distribution of the host galaxy contribution in the R band (left panel) is spread over
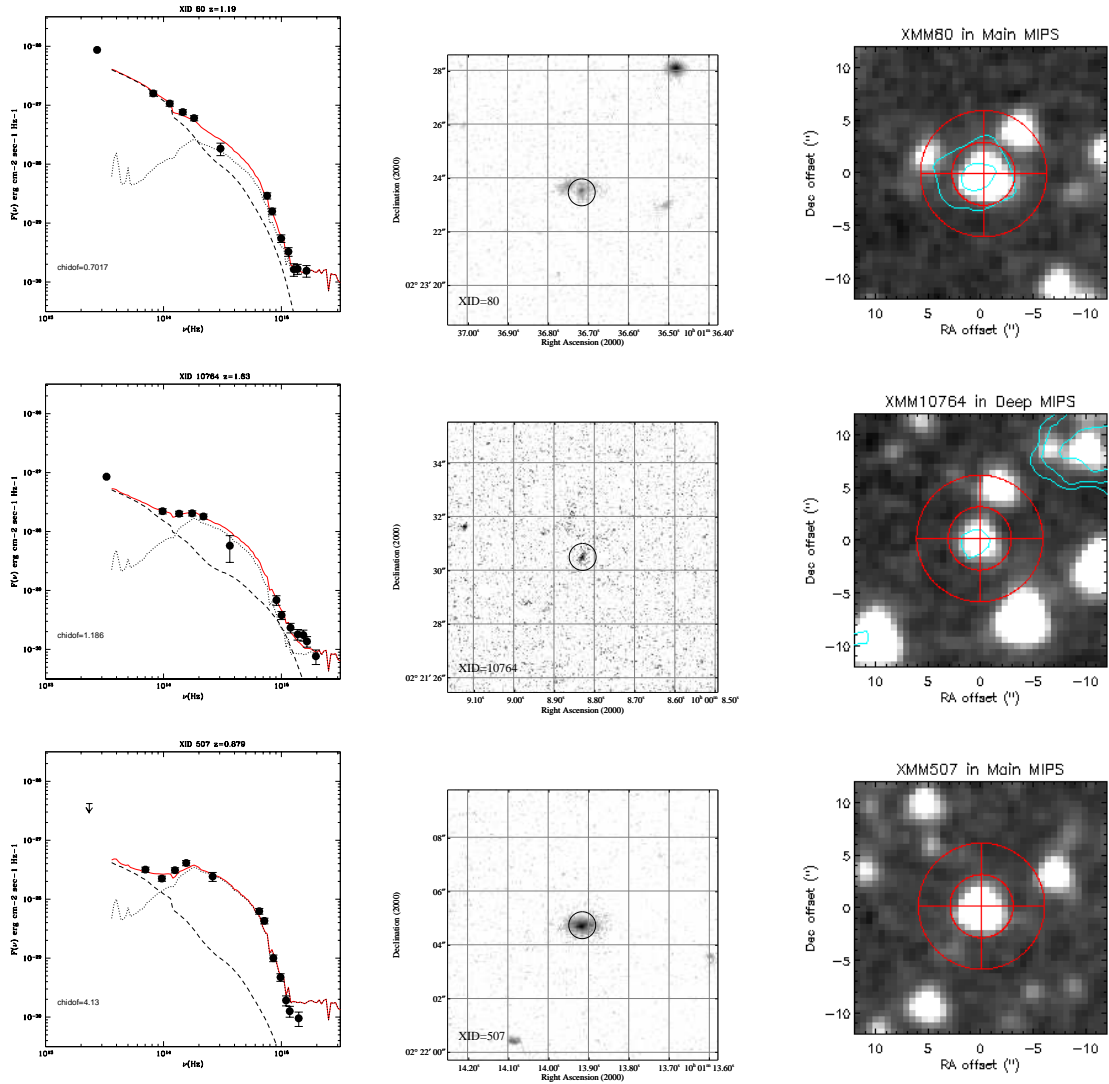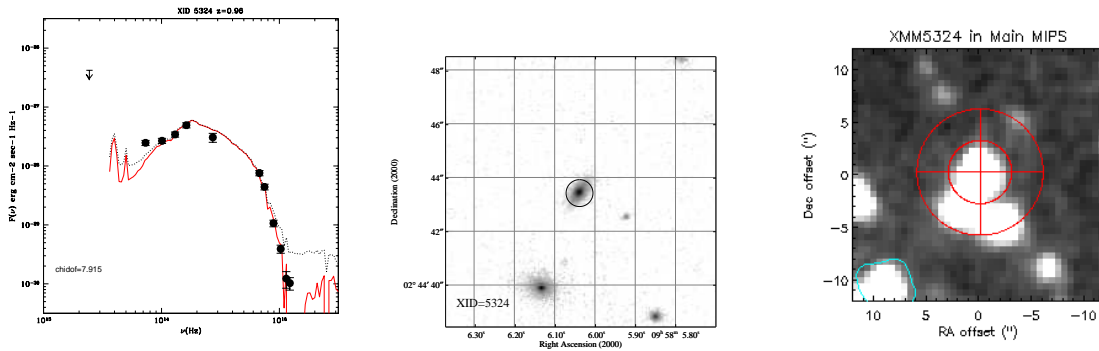
Figure 3.10: (Left) Rest-frame SED of a XERO dominated at all wavelengths by the host-galaxy component, compared with the best-fit model obtained as the sum (red line) of a host galaxy (early type or S0 or Sa, dotted line) and a nuclear component, the latter convolved with the extinction law described in the text (dashed line). The MIPS flux is reported as a downward pointing arrow. (Middle) The 10"×10" ACS image is presented. We note the clearly extended morphology in the ACS image. (Right) The 20"×20" 3.6μm image with overlaid the 24 μm contours (cyan; courtesy of H. Aussel) is shown.

a large range, however, in 60% of the sources the galaxy contribution is >45%. In the K band (middle panel), the AGN contribution to the observed total light for about 70% of the sources is <50% of the observed total flux (i.e., $f_K(AGN) < 0.5 \times f_K(tot)$). Therefore, the $R - K$ colors of a large fraction (70%) of the XEROs are mostly due to the superposition of the host galaxy light to the nuclear continuum. Only 18/63 sources (30% of the sample) are completely dominated in the K band by the nuclear light, showing a power-law infrared SED (i.e., $f_K(AGN) \sim 0.9 \times f_K(tot)$); 5 of them have also compact morphology. Several examples of the sources completely dominated in the K band by the nuclear component are shown in Fig. 3.7 (ordered from top to bottom by a decreasing percentage of the nuclear component). As evident in the IRAC cut-outs, the sources are clearly detected at both 3.6 and 24 μm wavelengths. Moving towards longer wavelengths (IRAC bands), the contribution of the galaxy light to the total emission slowly decreases and at 8μm (right panel) the nuclear component is responsible for the total emission in all but two sources. A few examples of sources in which the nuclear component dominates only at IRAC wavelengths are shown in Fig. 3.8. The first source shows a power-law SED and the 24 μm flux is fully in agreement with the SED extrapolation; the second source presents a red and fainter nuclear component that arises only at longer wavelengths and also a fainter MIPS counterpart; the third source, with a clear extended morphology, is more extreme than the previous one and is undetected at 24μm. The best-fitting SED obtained for source XID 5324 does not require any nuclear contribution (Fig. 3.10). The results obtained from the SED deconvolution reflect and confirm those obtained with the Lacy et al. (2004) diagram. As shown in Fig. 3.11, only a few objects (filled circles), that occupy the reddest part of the Lacy et al. region, are completely dominated at all infrared wavelengths by the nuclear component showing a power-law SED, while for most of objects (open circles) the infrared SED is due to the mixed contribution of nuclear and
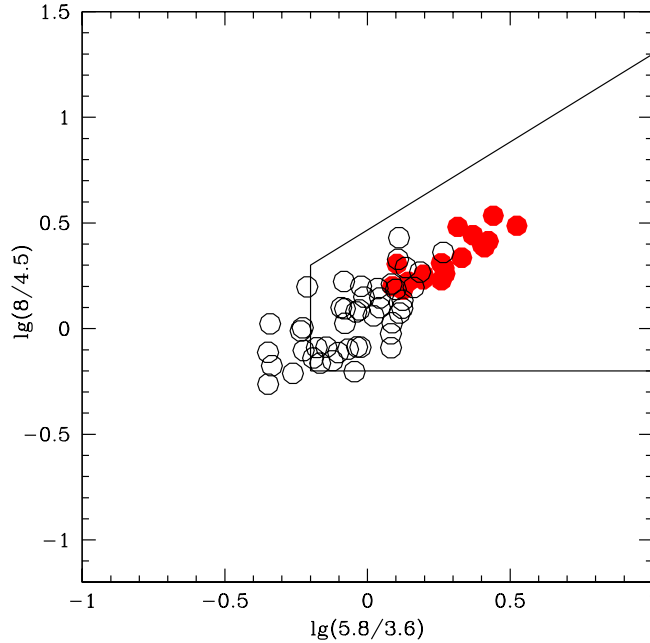
Figure 3.11: *Spitzer* IRAC color - color plot as in Fig. 3.6. The solid line denotes the color selection criterion used to pick out luminous AGN according to Lacy et al. (2004). XEROs dominates in the K band by the galaxy light are reported as open circles; conversely, sources dominated by the nuclear component in the K band are plotted as filled circles.

galaxy light. When the galaxy light contribution is higher, the sources move towards the blue part of the diagram.

3.6.1   Dust to gas ratio

The gas absorption column density can be determined from the X-ray spectrum, while the the dust extinction can be obtained from the ratio of the emission line fluxes (typically the Balmer lines), if visible. An output of the double-component SED fitting is the nuclear extinction in the optical. Therefore, for each source we have an estimate of the $E(B-V)$; the best-fit extinctions found are in the range $E(B-V) = 0.25$–1.60. By comparing the reddening of the nuclear optical continuum and the X-ray absorbing column density, we find that the $E(B-V)/N_H$ ratio is always lower (except for a few cases) than the Galactic standard value ($E(B-V)/N_H = 1.7 \times 10^{-22}$; Bohlin et al. 1978), in agreement with previous findings (Maiolino et al. 2001a,b; Georgakakis et al. 2006; Frank et al. 2007). This is shown in Fig. 3.12 where the $E(B-V)/N_H$ ratio relative to the Galactic value is plotted as a function of the 2-10 keV luminosity. Objects with luminosities and absorption column densities in the QSO 2 regime ($L_X > 10^{44}$ erg s^{-1} and $N_H > 10^{22}$ cm^{-2}) are plotted as encircled dots. In the same figure, the Maiolino et al. (2001a) sample, that includes different types of local Seyfert galaxies with X-ray luminosities lower than in our sample, is also plotted. Our sample extends to higher luminosity the
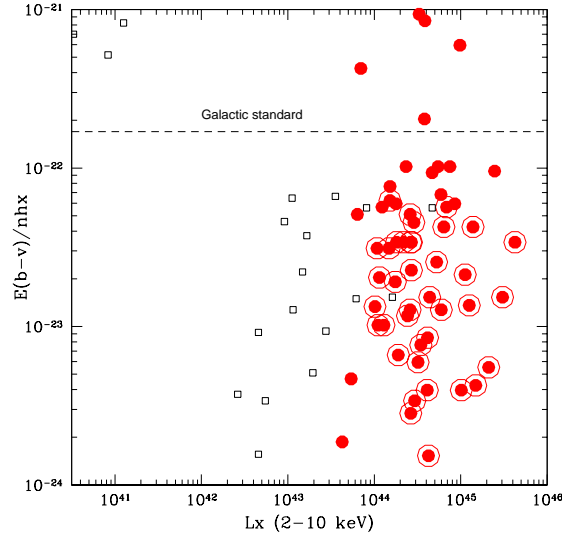
Figure 3.12: E(B-V)/N_H ratio as a function of the 2-10 keV luminosity for the objects in our sample (red filled circles) compared with the Maiolino et al. (2001) sample (black squares). Objects with luminosities and absorption column densities in the QSO 2 regime ($L_X > 10^{44}$ erg s^{-1} and $N_H > 10^{22}$ cm^{-2}) are plotted as encircled dots. The Galactic standard ratio is reported as dashed line.

previous findings: there is a large spread which is apparently not related to other obvious properties. A physical explanation for this discrepancy may be referred to the fact that the properties of dust grains in the circumnuclear region of AGNs, given the intense radiation field, are different in location and composition from the diffuse interstellar medium of our Galaxy (Maiolino et al. 2001b). In other words, larger dust grains can produce the effect observed in our objects.

3.7   Black hole masses

The BH masses of obscured AGN at high redshift are not accessible with direct measurement methods. In obscured sources, the host galaxy light overwhelms the nuclear emission and thus can be used to estimate the BH mass, assuming the relation derived locally between the host galaxy luminosity and the BH mass (e.g., Marconi & Hunt 2003). This relation has not been tested at high redshift and its behaviour at earlier epochs is still poorly known (see the Introduction and the references therein). Given that the fitting procedure performed in this Chapter allows us to determine the flux, and thus the luminosity, of the host galaxy at each frequency, we can convert the host galaxy luminosity into BH mass. To do this, we take advantage of the Marconi & Hunt (2003) relation. Given the uncertainties on the evolution of the M_{BH}-L_K relation, we have estimated the BH masses under two different hypotheses: first, the relation is higher than local one by a factor two in the redshift range of our sources (0.9<z<2), in agreement with the finding of Peng et al. (2006); secondly, the relation does not evolve with redshift.
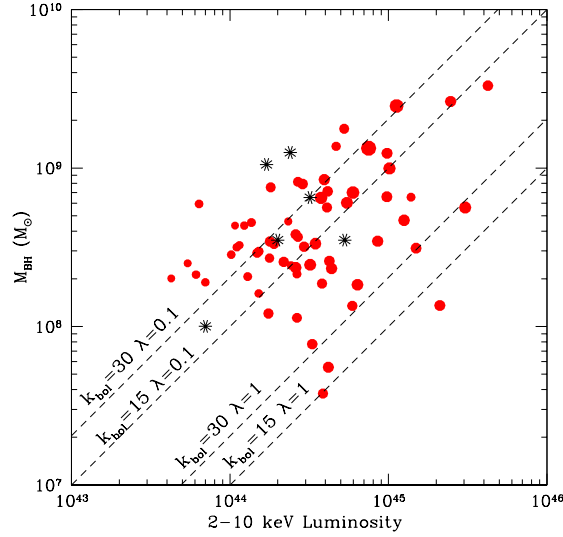
Figure 3.13: Black hole masses vs. hard X-ray luminosities for the XEROs (red circles) of our sample; starred symbols represent a sample of highly-obscured, high-redshift objects from Pozzi et al. (2007). The dimension of the red circles increases with the redshift of the sources. The two dashed lines represent the expected correlation between the two plotted quantities for two different assumptions on the bolometric correction and for λ=0.1 - 1.

In both cases, the results imply very massive BHs, with masses in the range $\sim 4 \times 10^7$–3×10^9 M$_\odot$ under the assumption of no evolution with redshift (Fig. 3.13, red circles). Our estimated M$_{BH}$ are consistent with the results derived by Pozzi et al. (2007) for a sample of sources (starred symbols in Fig. 3.13) sharing the same properties (colors, redshift and luminosities) of our sources and whose masses were estimated using a similar approach. The Pozzi et al. values reported in the figure are those computed assuming no evolution of the M$_{BH}$-L$_K$ relation. Similar results have been found by Brusa et al. (2005) computing the BHs masses for a sample of X-ray emitting EROs detected in the "Daddi Field".

The absorption-corrected X-ray luminosity could be translated into a bolometric luminosity assuming a bolometric correction factor $L_{bol} = k_{bol} \times L_X$. From the bolometric luminosity, it is possible to estimate the Eddington ratio ($\lambda = L_{bol}/L_{Edd}$). A bolometric correction in the range k$_{bol,2-10keV}$=15–30 is consistent with the model of Marconi et al. (2004), with the widely adopted value of Elvis et al. (1994), and also with the findings of Pozzi et al. (2007; k$_{bol,2-10keV}$=35±9). In Fig. 3.13, the dashed lines represent the relation between the BH mass and X-ray luminosity computed for Eddington-limited accretion (λ =1) and sub-Eddington accretion (λ =0.1) and assuming two bolometric corrections (k$_{bol,2-10keV}$=15, 30). There is a spread in the Eddington ratios of our sources in the range $\lambda = 0.08 - 1$, with a median value of $\lambda = 0.16$ with k$_{bol,2-10keV}$=30 and a factor two lower ($\lambda = 0.08$) if we consider k$_{bol,2-10keV}$=15. Both the BH masses and the Eddington ratios derived above are consistent with a scenario in which XEROs are obscured luminous quasars emitting at relatively high Eddington ratios.

3.8 Summary

Thanks to the multiwavelength database offered by the COSMOS survey, it has been possible to collect a large sample of X-ray emitting extremely red objects with homogeneous and good multiwavelength coverage. The main results are reported in the following.

- The analysis of their global properties (X-ray to optical and near-infrared colors) has confirmed previous results on the basis of which the selection of hard X-ray sources (namely sources with high X/O) with extremely red colors is efficient in picking up high-luminosity, highly obscured sources. It should be noted that not all X-ray obscured QSOs are EROs. Among the XEROs of our sample, the 55% have the properties of Type 2 QSOs.

- A rough morphological classification, obtained by the visual inspection of the HST/ACS images, suggests that most of the XEROs (90%) present an extended morphology due to a prominent host galaxy. Although it is expected, it has not been previously proven as it requires very good optical imaging. Further morphological analyses will be performed on the brightest sources.

- Thanks to the *Spitzer* coverage, additional clues on the nature of these sources can be provided by their mid-IR properties. The mid-IR color - color plot suggests that most of our sources are contaminated by the host galaxy light up to the infrared bands.

- Thanks to the multiwavelength fitting performed in the optical and near-infrared for a representative subsample of the XEROs population, we can argue that the red colors of the majority (70%) of the sources can be explained by the host galaxy stellar emission significantly contributing to the total continuum, with the AGN emission is most likely blocked by the obscuring screen of gas and dust. Moving towards longer wavelengths, the host galaxy contribution slowly decreases, favouring the arising of the nuclear light. Nuclear extinctions, black hole masses and Eddington ratios are provided as output of the SED approach.

- A comparison between the effective hydrogen column densities derived by the X-ray hardness ratio and the nuclear extinction derived by fitting the broad-band optical and infrared continuum reveals that there is no a standard relation between the two quantities, i.e., the $E(B-V)/N_H$ ratio is always lower than the Galactic one.

- Thanks to the independent estimates of the galaxy and nuclear light, the masses of the central BHs have been estimated using the M_{BH}-L_K relation. Under the hypothesis of no evolution with redshift for this relation, our XEROs have masses in the range $\sim 4 \times 10^7$–3×10^9 $M_\odot$ and are characterized by relatively high Eddington

ratios ($\lambda = 0.08 - 1$, with a median value λ=0.16 if a bolometric correction $k_{bol,2-10keV}$=30 is assumed).

Table 3.1: Properties of XEROs.

XID	RA	DEC	f_X [a] 2-10 keV	HR	R AB	R-K Vega	X/O	Lx [b] 2-10 keV	z	z type [c]
18	150.1330279	2.3032356	5.68e-14	-0.38	23.99	5.20	1.77	45.56	1.810	1
43	149.8341836	2.3086705	2.77e-14	-0.46	23.51	5.66	1.27	44.66	1.162	2
55	150.0850192	2.1536439	1.79e-14	-0.35	24.32	5.08	1.40	44.38	1.090	1
80	150.4029812	2.3900175	1.03e-14	-0.62	24.55	5.46	1.25	44.26	1.190	1
81	150.2731798	1.9340075	3.53e-14	-0.47	23.78	5.72	1.48	44.45	0.915	2
106	150.1584952	2.4154924	1.57e-14	-0.23	24.72	5.72	1.50	43.78	0.710	2
108	150.1221429	1.9130143	1.33e-14	-0.46	24.93	5.28	1.52	44.63	1.450	1
145	150.0199831	2.3493176	1.79e-14	-0.12	24.95	5.84	1.65	45.04	1.790	1
155	150.4467058	2.7495897	2.50e-14	-0.20	23.25	5.31	1.12	44.78	1.320	1
175	149.7207740	2.3490901	2.97e-14	-0.60	23.77	5.28	1.40	45.08	1.560	1
181	150.2674805	2.0555416	1.26e-14	-0.51	25.49	5.36	1.72	44.55	1.390	1
223	150.2118511	2.1865278	5.36e-15	-0.53	25.30	5.64	1.27	44.59	1.890	1
237	150.1825281	2.2474814	3.99e-15	-0.45	23.82	5.36	0.55	44.83	2.472	2
240	150.0030587	2.1569762	6.10e-15	-0.29	23.39	5.00	0.56	43.87	1.050	1
266	150.2521018	2.5258517	1.18e-14	0.22	25.02	5.55	1.50	44.56	1.430	1
280	150.4722099	2.3249136	1.17e-14	1.00	24.69	6.19	1.36	44.59	1.470	1
291	150.0593471	2.1122085	9.74e-15	0.07	23.67	5.26	0.88	44.66	1.640	1
294	149.9063062	1.9172077	1.50e-14	-0.54	23.78	5.42	1.11	44.61	1.370	1
348	149.8422877	2.3239684	1.01e-14	1.00	24.61	5.87	1.27	44.00	0.980	1
371	150.1988567	2.5975452	7.25e-15	0.03	23.15	5.15	0.54	43.76	0.910	1
380	150.4606715	2.3589955	5.73e-15	-0.23	24.54	5.28	0.99	43.79	1.010	1
390	149.9918428	2.5899649	9.46e-15	-0.10	25.32	5.93	1.52	44.47	1.440	1
393	150.2434117	2.0774925	1.06e-14	0.17	24.76	5.46	1.35	44.39	1.300	1
400	149.8182715	2.0527178	9.04e-15	-0.37	24.68	5.17	1.25	44.42	1.400	1
428	150.2421154	1.8591031	7.35e-15	-0.47	25.53	5.82	1.50	44.85	2.070	1
442	150.3787361	2.7345663	7.00e-15	-0.12	24.61	5.53	1.11	43.86	1.000	1
472	150.3498860	2.8268949	6.50e-15	-0.25	22.42	5.17	0.20	43.75	0.940	1
480	150.4261133	2.6089709	4.06e-15	-0.55	24.31	5.43	0.75	43.80	1.140	1
492	150.3425217	2.3926921	6.31e-15	-0.41	25.79	5.71	1.54	44.32	1.460	1
507	150.3074579	2.3681264	5.10e-15	1.00	23.90	5.11	0.69	43.56	0.879	2
2028	150.5470301	1.6186942	7.46e-14	-0.49	23.68	6.24	1.76	45.51	1.590	1
2050	150.0641291	1.5294941	1.27e-13	-0.41	23.42	5.48	1.89	45.21	1.070	1
2208	150.4746579	2.0939209	6.12e-14	0.16	23.83	5.55	1.74	45.39	1.560	1
2226	150.6066231	1.9352445	1.51e-14	-0.38	23.17	5.10	0.87	43.98	0.844	2
2253	150.5056379	2.2258002	6.57e-14	-0.56	22.63	5.13	1.29	44.69	0.890	1
2258	149.6116364	2.3537292	1.47e-14	-0.56	24.87	5.57	1.54	44.78	1.570	1
2318	150.7576442	1.7856554	2.13e-14	0.02	25.09	5.52	1.78	45.02	1.670	1
2336	150.6022876	1.7689283	1.23e-14	-0.01	24.66	5.07	1.37	44.82	1.710	1
2382	150.4599660	1.9769763	1.11e-14	-0.46	24.52	5.48	1.27	44.70	1.620	1
2440	150.6717461	1.7608536	6.92e-15	-0.47	23.88	5.38	0.81	43.88	1.020	1
2464	150.5401256	2.1676988	1.13e-14	-0.40	23.92	5.15	1.04	44.82	1.750	2
2465	150.6945874	1.8873349	1.29e-14	0.18	25.18	5.90	1.60	44.50	1.330	1
2480	150.7562136	1.8069437	1.40e-14	0.03	23.67	5.10	1.03	44.07	0.930	1
2543	150.3435868	2.1404188	8.32e-15	-0.46	25.09	5.25	1.38	44.83	1.960	1
2594	149.6882260	2.4780705	4.31e-15	-0.50	24.03	5.16	0.67	43.82	1.140	1
2668	150.2475256	1.5425366	2.96e-14	0.34	24.05	5.30	1.51	44.33	0.886	2
2772	150.6543577	1.5354332	1.03e-14	-0.49	24.58	5.37	1.26	44.66	1.610	1
5006	149.7412679	2.5849184	7.57e-15	0.20	24.71	5.94	1.18	44.64	1.760	1
5009	149.8326074	2.1333117	5.84e-15	1.00	24.46	5.10	0.97	43.75	0.970	1
5039	150.4871763	2.0157803	5.47e-15	-0.44	25.24	5.23	1.25	44.20	1.400	1
5053	150.3708983	1.9531653	1.49e-14	1.00	25.19	6.04	1.67	44.61	1.380	1
5056	149.6722220	1.9413358	1.27e-14	-0.31	24.59	5.56	1.36	44.44	1.280	1
5070	149.8762007	2.5687332	1.54e-14	-0.03	24.49	5.45	1.40	44.72	1.480	1
5084	149.5742439	2.8832552	7.37e-15	-0.30	25.22	5.81	1.38	44.33	1.400	1
5124	150.6448633	2.3506722	1.17e-14	-0.34	24.17	5.68	1.16	44.48	1.350	1
5153	149.5865469	1.7692322	3.21e-14	0.44	22.88	5.25	1.08	45.09	1.540	1
5178	149.8240028	2.3849568	5.90e-15	0.00	25.25	5.82	1.29	44.07	1.240	1
5205	150.4911023	1.7940780	8.34e-15	-0.16	24.51	5.38	1.15	44.38	1.400	1
5231	150.5382012	2.7156869	6.04e-15	-0.42	25.17	5.42	1.27	44.11	1.270	1
5263	149.8266392	1.9408160	8.41e-15	1.00	24.12	5.10	0.99	43.97	1.020	1
5283	149.7653162	2.6484907	1.07e-14	-0.06	25.41	5.32	1.61	44.76	1.710	1
5288	149.5705340	1.9904480	1.30e-14	-0.42	23.36	5.14	0.88	44.24	1.090	1
5294	149.5059033	2.6422235	3.53e-15	-0.60	25.55	5.18	1.19	44.48	1.990	1
5321	150.7869826	2.1510475	1.55e-13	-0.48	22.90	6.27	1.77	45.68	1.430	1
5324	149.5251398	2.7448496	1.72e-14	-0.57	23.83	5.29	1.19	44.20	0.960	1
5357	149.5384170	2.7213310	6.63e-15	0.11	25.21	5.02	1.33	44.55	1.710	1
5368	149.8917052	2.5786874	8.09e-15	-0.48	24.00	5.44	0.93	44.31	1.340	1
5408	150.5341251	1.9525828	6.17e-15	-0.21	23.52	5.19	0.62	43.85	1.030	1
5412	150.5403743	1.9695623	6.38e-15	-0.43	23.05	5.16	0.44	44.08	1.220	1
5414	150.5960050	2.3358836	9.18e-15	-0.41	24.00	5.11	0.98	44.22	1.200	1

Table 3.1: Properties of XEROs (continued).

XID	RA	DEC	f_X [a] 2-10 keV	HR	R AB	R-K Vega	X/O	lg(Lx) [b] 2-10 keV	z	z type [c]
5430	150.0978401	2.8021366	5.41e-15	-0.58	25.12	5.56	1.20	44.26	1.470	1
5438	150.7437507	2.2011513	2.53e-14	-0.47	24.62	5.03	1.67	44.86	1.400	1
5441	150.3690292	1.7922443	6.94e-15	-0.28	23.92	5.10	0.83	44.28	1.380	1
5467	150.6430892	2.5293023	7.74e-15	-0.18	24.45	5.03	1.09	44.01	1.080	1
5469	150.4496595	2.3193975	4.37e-15	-0.33	24.20	5.19	0.74	43.97	1.270	1
5487	149.5977808	2.8030775	5.20e-15	-0.68	25.52	6.29	1.34	44.20	1.430	1
5511	149.6207450	2.6145431	7.18e-15	0.10	24.13	5.27	0.93	43.67	0.850	1
5530	149.5173383	1.8636898	1.15e-14	-0.50	26.04	5.83	1.90	44.80	1.720	1
5533	149.5940248	2.6145721	1.12e-14	-0.37	24.22	5.64	1.16	45.11	2.190	1
5549	149.6839912	1.9328868	1.56e-14	-0.49	26.05	6.34	2.03	44.86	1.630	1
5569	150.7904589	2.5504768	1.94e-14	-0.27	25.19	5.45	1.78	44.94	1.620	1
5573	149.5298775	1.7856366	2.39e-14	-0.35	24.46	5.46	1.58	44.96	1.540	1
10184	149.4905063	2.8684680	1.46e-14	1.00	25.56	5.12	1.81	44.82	1.620	1
10498	150.4966988	2.0890306	5.28e-15	-0.23	23.19	5.00	0.42	44.08	1.300	1
10597	150.6806496	2.8369197	7.65e-15	-0.36	25.21	5.88	1.39	44.67	1.790	1
10662	149.5500075	2.4786970	9.42e-15	-0.27	24.57	5.57	1.22	44.52	1.490	1
10747	149.4226065	2.4456759	1.37e-14	-0.32	25.29	5.37	1.67	44.78	1.610	1
10764	150.0369857	2.3581252	5.65e-15	1.00	25.48	5.13	1.36	44.41	1.630	1
30342	150.5501210	2.5258689	4.87e-15	-0.16	24.94	5.14	1.08	44.33	1.180	1
30361	150.4371453	2.7208718	5.03e-15	-0.24	25.06	5.21	1.15	45.08	2.160	1
31313	149.8884228	2.8437660	3.27e-14	-0.55	24.67	5.93	1.80	44.75	1.190	1
31340	150.4336615	2.2255135	5.29e-15	-0.32	25.35	5.28	1.28	44.61	1.190	1
31357	150.3958540	2.6352743	8.02e-15	0.07	24.84	5.81	1.26	44.14	1.150	1
53565	150.7660085	1.7931335	7.18e-15	-0.36	24.20	5.93	0.96	44.12	1.280	1
54020	150.0643982	2.4175678	7.81e-15	-0.23	24.90	5.72	1.27	44.13	1.340	1
54055	149.8992188	2.6941535	9.13e-15	-0.17	23.65	5.46	0.84	44.27	1.100	1
54279	149.4643204	1.5952553	1.81e-14	-0.54	24.41	5.13	1.44	44.66	1.340	1
54461	150.7642207	2.4658377	2.08e-14	1.00	23.96	5.52	1.32	44.48	1.190	1
54464	150.7234012	2.4087660	1.12e-14	1.00	25.27	5.56	1.58	44.51	1.660	1
54466	150.6059254	2.4366181	7.00e-15	1.00	24.16	5.43	0.93	44.06	1.020	1
54480	150.2070346	1.6798477	1.17e-14	0.11	24.22	5.64	1.18	44.56	0.713	2
54486	150.1567529	2.0893113	5.88e-15	1.00	25.48	5.33	1.38	43.84	1.140	1
54540	149.4211432	1.8562607	1.63e-14	0.02	23.78	5.50	1.14	43.91	1.190	1
60023	150.4831504	2.8287263	1.10e-14	0.03	23.38	5.06	0.81	44.19	0.950	1
60024	150.2983545	2.2133297	5.31e-15	1.00	24.34	5.20	0.88	43.96	1.147	2
60031	150.7255228	2.8271887	8.27e-15	-0.21	24.87	5.79	1.29	43.91	1.120	1
60044	150.6455567	2.2940700	4.51e-15	-0.18	24.74	5.19	0.97	43.87	1.240	1
60049	150.2756408	2.4769144	4.65e-15	-0.02	24.02	5.70	0.70	43.79	0.930	1
60084	150.7708507	2.4094437	1.45e-14	1.00	24.19	5.23	1.26	44.43	1.090	1
60133	150.2964289	1.8918033	5.54e-15	-0.25	25.47	5.14	1.35	43.96	2.790	1
60144	150.6605614	1.8340781	7.14e-15	1.00	25.34	5.95	1.41	44.10	1.740	1
60174	150.2798858	2.1835692	4.21e-15	-0.16	24.53	5.24	0.86	44.79	1.241	2
60206	150.4298759	1.9883259	5.73e-15	0.09	24.58	5.05	1.01	44.37	0.990	1
60261	149.8552445	2.7674143	6.24e-15	1.00	26.24	6.26	1.71	44.10	1.240	1
60312	149.4640825	2.7761522	5.91e-15	-0.31	25.74	6.02	1.49	43.81	1.150	1
60335	149.5728865	2.7103444	4.62e-15	1.00	23.47	5.13	0.47	43.91	0.990	1
60452	149.5121372	1.7635162	7.14e-15	1.00	25.89	5.74	1.63	44.08	1.260	1
332	150.2854990	2.3094721	4.57e-15	-0.44	27.15	7.17	1.94	43.80	1.730	1
2814	150.3838225	2.0667613	7.32e-15	-0.20	25.77	6.13	1.59	44.43	2.970	1

[a] In units of 10^{-15} erg cm^{-2} s^{-1}; [b] In units of erg s^{-1}; [c] 1=photometric redshift, 2= spectroscopic redshift

Chapter 4

Unveiling the nature of XBONGs

While a unique solution may not necessarily hold for all the *XBONGs* observed in different surveys and thus they may constitute a mixed population, they represent a useful benchmark for a better understanding of the AGN activity and, as such, deserve further studies. Ideally, one would need sensitive, high-spatial resolution, multiwavelength observations from radio to X-rays. As a first step, in the following we use good-quality photometric near-infrared data obtained with ISAAC at VLT of four low-redshift *XBONGs*, selected in the HELLAS2XMM survey to search for the presence of a putative nucleus which has escaped detection in the optical spectroscopy. The rather obvious advantage of near-infrared data is that the effects of dust reddening are minimized. At the same time, the excellent quality of the near-IR images make possible to apply a surface brightness decomposition technique to search for weak unresolved nuclear emission down to faint magnitudes.

4.1 Multiwavelength data analysis

The four *XBONGs* were serendipitously detected in the HELLAS2XMM 1 square degree field (1dF) sample (see Baldi et al. 2002 for a description of the X-ray data and Fiore et al. 2003 for the optical identification process). The multiwavelength analysis of the *XBONG* prototype PKS 03120018 (also known as P3) is presented in Comastri et al. (2002). All four sources have hard (2-10 keV) X-ray luminosities larger than $\sim 10^{42}$ erg s^{-1}, while the optical spectra are characterized by a red continuum with stellar absorption lines (Fig. 4.1).

 The spectroscopic observations were obtained at the ESO 3.6m telescope equipped with EFOSC2 during different observing runs in 2001. While the relatively large slit width (2 arcsec) used in the spectroscopic observations do not preserve us from a galaxy light contamination (and consequent line dilution), the good signal-to-noise ratio
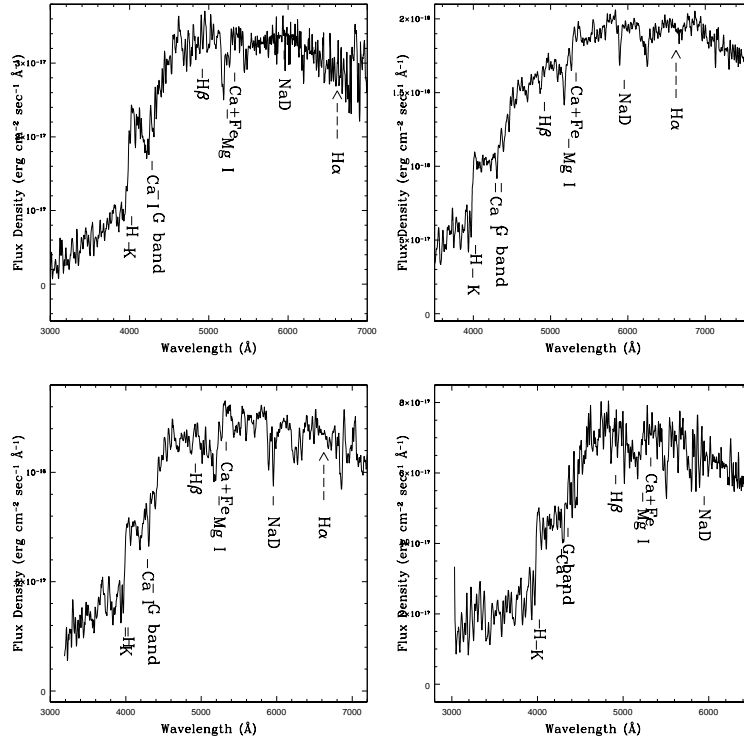
Figure 4.1: Rest frame optical spectra of the sources PKS 03120017, PKS 03120018 (top), Abell 2690013 and Abell 1835140 (bottom) taken with the ESO 3.6m telescope.

(S/N$_{6000Å}$ >13–20) and the well suited spectral range (including the expected position of the $[OIII]_{5007Å}$ and $H\alpha_{6563Å}$ lines, with the exception of Abell 1835140) allow us to place firm constraints on the line fluxes. The corresponding luminosity upper limit for the O[III] line of the four *XBONGs* is in the range 10^{39}-10^{40} erg s^{-1}, about one order of magnitude fainter than that measured in the optical spectra of HELLAS2XMM broad-line (BLAGN) and narrow-line (NLAGN) AGN with comparable X-ray luminosity (see Fig. 4.2 and Cocchia et al. 2007). The redshifts obtained from the position of the principal absorption lines are $z = 0.319, 0.159, 0.154, 0.251$ for PKS 03120017, PKS 03120018, Abell 2690013 and Abell 1835140, respectively. Radio observations at 5 and 8.7 GHz are available for the two objects in the PKS 0312-77 field. Source PKS 03120017 was detected with a flux density of 1.3 mJy at 5 GHz and of 0.5 mJy at 8.7 GHz, while source PKS 03120018 remains undetected (F$_{5GHz}$ < 0.15 mJy at 3 sigma).

4.1.1 X-ray spectral analysis

The results of the spectral analysis of the X-ray sources in the 1dF sample are presented in Perola et al. (2004) with particular emphasis towards the statistical properties of the sample. The X-ray spectra of the four *XBONGs* discussed here were re-analyzed including an additional observation of the Abell 18350140 field (not included in the Perola et al.
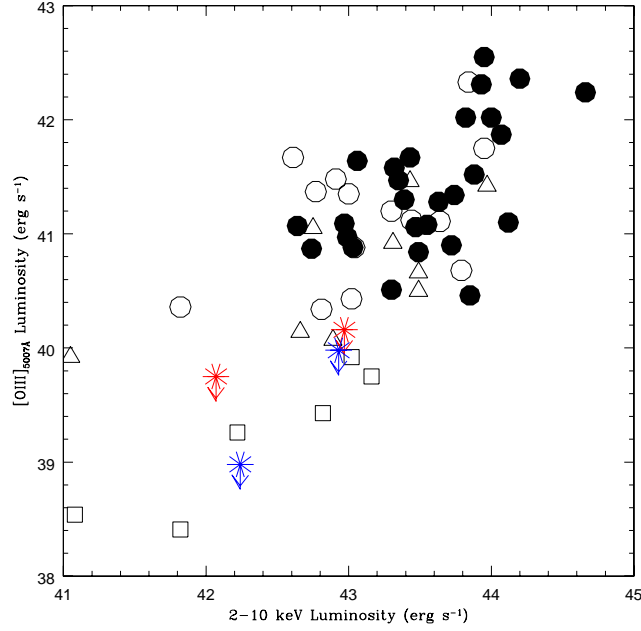
Figure 4.2: The $[OIII]_{5007\text{Å}}$ luminosity versus the 2-10 keV luminosity for 59 sources of the HELLAS2XMM sample as presented in Cocchia et al. (2007). Starred symbols mark the four *XBONGs* discussed in this paper; filled circles = narrow-line AGN; open circles = broad-line AGN; open triangles and open squares = emission-line and early-type galaxies, respectively.

paper) using the most recent calibrations. The data were processed using standard SAS[1] v6.1.0 and FTOOLS tasks.

The pn spectra were grouped with a minimum of 10 counts per bin (for PKS 03120018 and PKS 03120017) and 15 counts per bin (for Abell 26900013 and Abell 18350140) using the task GRPPHA, and fitted with XSPEC v11.3.0 (Arnaud 1996), while MOS1 and MOS2 data, having much lower counting statistics, were left unbinned and fitted with the C-statistic (Cash 1979). We checked and found the consistency between the pn and MOS data, although the X-ray spectral results (Table 4.1) and the best-fitting spectra (Fig. 4.3) are referred to the pn data alone.

In the following we summarize the main X-ray spectral results.

----

[1]XMM–*Newton* Science Analysis System; see http://xmm.vilspa.esa.es/external/xmm_sw_cal/sas_frame.shtml.

Table 4.1: X-ray spectral analysis parameters.

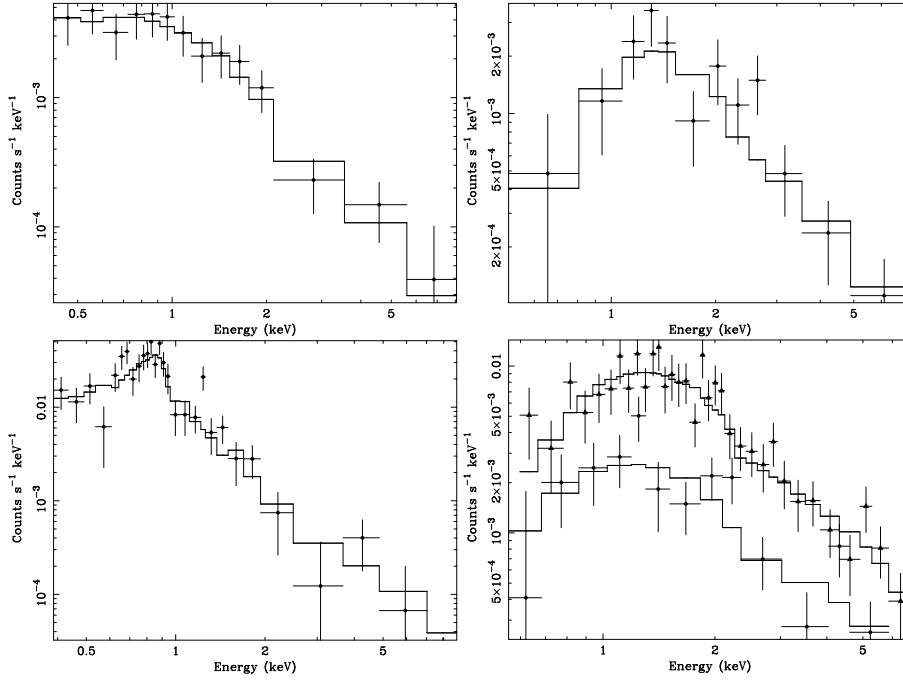| Src. ID	kT (keV)	Γ	N_H (cm^{-2})	χ^2/d.o.f	$F_{2-10\,keV}$ (erg cm^{-2} s^{-1})	$L_{2-10\,keV}$ (erg s^{-1})
PKS 03120017		$2.40^{+0.62}_{-0.40}$	$< 2.11 \times 10^{21}$	3.7/11	1.4×10^{-14}	5.0×10^{42}
PKS 03120018		$2.11^{+0.82}_{-0.36}$	$6.86^{+7.94}_{-4.58} \times 10^{21}$	9.6/9	1.5×10^{-14}	1.1×10^{42}
Abell 26900013	0.73 ± 0.06	$1.64^{+0.63}_{-0.87}$		34.4/25	1.5×10^{-14}	9.6×10^{41}
Abell 18350140		$1.50^{+0.61}_{-0.51}$	$4.25^{+4.99}_{-2.36} \times 10^{21}$	14.0/12	5.3×10^{-14}	9.0×10^{42}
		$1.71^{+0.31}_{-0.27}$	$6.46^{+2.91}_{-2.20} \times 10^{21}$	32.9/35	1.8×10^{-13}	3.3×10^{43}

Figure 4.3: XMM-Newton (pn) spectra of the sources PKS 03120017, PKS 03120018, Abell 2690013 and Abell 1835140 (from top-left to bottom-right), fitted in the 0.5-8 keV range. The solid line represents the best-fitting model. The spectral parameters are reported in Table 4.1. For source Abell 1835140, the spectra of the two available observations are reported.

Two sources, PKS 03120018 and Abell 18350140, are best fitted by an absorbed power law with photon index in the range $\Gamma \approx$ 1.5-2.1 and column densities ($N_H \approx 4 - 7 \times 10^{21}$ cm^{-2}), typical of a mildly obscured AGN. Despite the relatively large errors in the determination of the X-ray spectral parameters, this analysis seems to rule out Compton-thick absorption, at least in the energy range covered by XMM–*Newton*. The radio-loud source PKS 03120017 is best fitted by a relatively steep $\Gamma \simeq 2.4$ spectrum (but consistent with $\Gamma \sim 2$) and no absorption in excess to the Galactic value (see Table 4.1).

Abell 26900013 is well fitted using a thermal (MEKAL) model at soft energies and a weakly constrained power-law tail at higher ($\gtrsim 2$ keV) energies. The thermal spectrum is consistent with the extended appearance of the X-ray emission, as shown by the overlay of the X-ray contours on the K_s-band image (see Fig. 4.4).

Significant X-ray flux variability (a factor about 3) is present between the two XMM–*Newton* observations of Abell 18350140. This object was also observed twice and detected by *Chandra* (in 1999 and 2000, for ≈ 20 and 10 ks, respectively). Unfortunately, it was at very large off-axis radii, making it impossible to deconvolve the X-ray emission from the two optical close nuclei (less than 1 arcsec, see below). Nevertheless, *Chandra* data (especially the data of the first and longer observation) confirmed the XMM–*Newton* spectral results and allowed for a long-term variability study of this source. Over ≈ 3
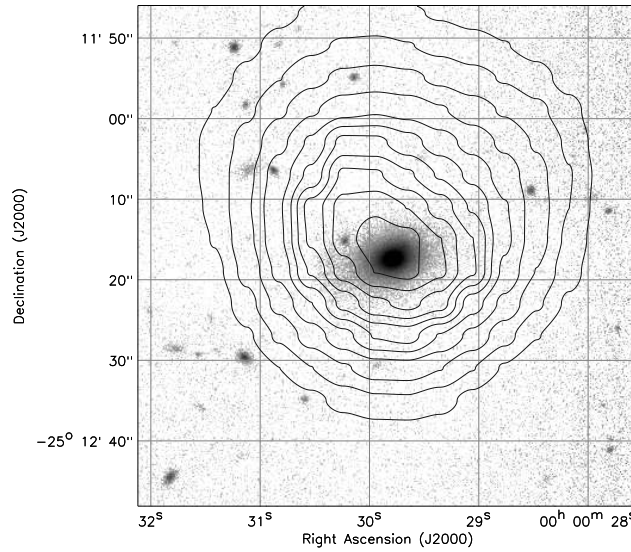
Figure 4.4: X-ray contours obtained from the 0.5-10 keV adaptively smoothed pn image of source Abell 2690013 overlaid on the K_s-band image. The image is ≈ 60"$\times 60$".

and half years, Abell 18350140 was found to be variable by a factor of ≈ 7.5, with its 2-10 keV flux increasing from the value of $\approx 2.4 \times 10^{-14}$erg cm^{-2} s^{-1} in 1999 to $\approx 1.8 \times 10^{-13}$erg cm^{-2} s^{-1} in 2003, with no evidence for significant changes in the X-ray spectral parameters.

4.2   Near-Infrared data analysis

4.2.1   Near-Infrared imaging observations

Deep near-infrared observations have been carried out using the Infrared Spectrometer and Array Camera (*ISAAC*) mounted on the ESO VLT (Very Large Telescope). *ISAAC* is equipped with a Rockwell Hawaii 1024$\times$1024 HgCdTe array, with a pixel scale of 0.147"/pixel and a field of view of 2$'$.5 $\times$ 2$'$.5. The observations have been collected in service mode over several nights during September 2002 under good seeing conditions (<0".8). The ISAAC images were taken in two near-IR bands (the *J* and K_s[2] filters) and were reduced using the DIMSUM[3] package, following standard procedures. A detailed discussion on the data reduction of similar images taken for other sources revealed in the HELLLAS2XMM 1dF is reported in Mignoli et al. (2004). The total exposure times for each galaxy is 600 sec in *J* and 1800 sec in K_s band. The effective seeing on final frames ranges between 0.5 and 0.8 arcsec (FWHM). The magnitude limits for point-like sources are about *J*(lim)=22 and K_s(lim)=21.5 in all the images. The K_s- band images of all the four sources are shown in Figure 4.5.

---

[2]The K_s (K-short) filter is centered at shorter wavelenght than the standard *K* filter in order to reduce thermal background.
[3]Deep Infrared Mosaicing Software, developed by P.Eisenhardt, M.Dickinson, A.Stanford and J.Ward., and available at the site `ftp://iraf.noao.edu/contrib/dimsumV2`.
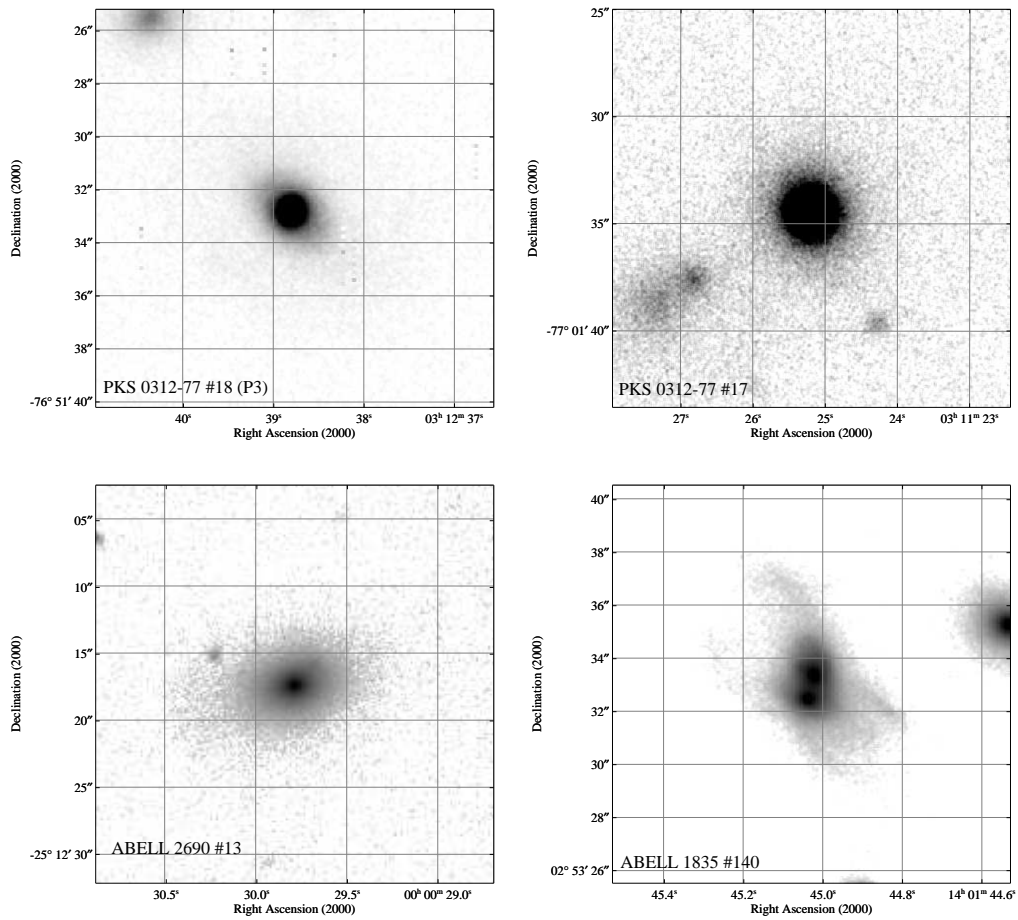
Figure 4.5: K$_s$-band images: PKS 03120018, PKS 03120017, Abell 2690013 and Abell 1835140, from top left to bottom right; the size of the images is 15"×15", 20"×20", 30"×30", 15"×15", respectively.

4.2.2   The fitting procedure

The surface brightness decomposition has been performed with GALFIT (Version 2.0.3b, Peng et al. 2002), a two-dimensional algorithm designed to extract structural parameters directly from galaxy images combining several analytical models and by convolving them with the image Point Spread Function (PSF). The PSF has been modeled adopting several field stars in each ISAAC image.

 The fitting procedure was performed separately in both J and K_s bands, allowing us to cross-check the results and test for a possible color trend. In order to better constrain the galaxy structural parameters (magnitude and effective radius), first we fitted each object in the J band where the AGN contribution to the total light was expected to be lower, as actually found in our analysis. Then we applied GALFIT to the K_s-band images, using the galaxy parameters obtained in the J band as start-up values for the nuclear decomposition.

 As a first guess of the profile of the host galaxy, we applied a Sérsic model (Sérsic 1968) of the form:

$$\mu(r) = \mu_e \, e^{-\kappa\left[\left(\frac{r}{r_e}\right)^{1/n} - 1\right]} \tag{4.1}$$

 where μ_e is the effective surface brightness, r_e the effective radius, n the Sérsic index, and κ a constant determined from n in order to have half of the integrated flux within r_e. The Sérsic index assume value ~ 1 in case of exponential profile and value $n = 4$ in case of a de Vaucouleurs profile (de Vaucouleurs 1948). Since the index was found to be $n \gtrsim 4$ for all the sources, in the second step of the fitting we adopted a de Vaucouleurs profile, hereafter referred to as MODEL 1.

 If residual emission in the innermost region was still present after fitting the galaxy with MODEL 1, the contribution of a point-like source (MODEL 2) was added. The latter contribution is modeled using the PSF profile obtained from several field stars. The centroid of the unresolved component and that of the host galaxy have been linked with each other in the fitting procedure. We considered the unresolved component detected if the χ^2 improves with the inclusion of the nuclear component and if it is brighter than the image magnitude limit for point-like sources.

 In order to check the GALFIT capabilities to detect a faint unresolved source at the center of a bright galaxy, accurate simulations were performed using the IRAF task *mkobject*. We started with a bulge ($r^{1/4}$) profile and then has been added a point-like source. In the simulations we adopted a grid of magnitudes in the range K_s=14 – 22 for the host galaxy and K_s=17 – 22 for the point-like component; different effective radii (from 30 to 120 pixels) for the host component have been used. The input parameters have been chosen in an appropriate range to reproduce the observed data and also to span a wider but realistic parameter space. The simulated images have been convolved with the seeing and the noise of our images; the PSF has been modeled with the parameters determined from the field stars. We ran GALFIT on the simulated sources first applying a de Vaucouleurs profile and

Table 4.2: Results of the fits performed with Galfit in the J and in the K_s band; the two entries for each source in each band correspond to the fitting with MODEL 1 and with MODEL 2, respectively.

id	band	Model	m_{host}	r_{eff} (kpc)	$m_{nucleus}$	$\chi^2_{d.o.f}$
PKS03120017	J	1	16.94±0.03	4.79±0.51		0.94
	J	2	16.92±0.05	5.64±0.86	20.75±0.29	0.93
	K_s	1	15.24±0.01	4.96±0.17		1.1
	K_s	2	15.21±0.01	6.50±0.10	18.39±0.24	1.0
PKS03120018	J	1	16.51±0.02	3.73±0.30		1.50
	J	2	16.52±0.01	4.03±0.40	20.30±0.35	1.40
	K_s	1	15.25±0.01	3.30±0.05		1.7
	K_s	2	15.20±0.01	5.04±0.20	18.09±0.10	1.4
Abell2690013	J	1	15.41±0.01	7.84±0.10		1.05
	K_s	1	14.29±0.01	6.86±0.20		2.15

then adding a central unresolved component, as performed for the *XBONGs*. The fitting results are fully consistent with the input parameters. Uncertainties ($\Delta\,mag \sim 0.02$) on the determination of the nuclear magnitude have been found in the case of a very faint ($K_s \gtrsim 22.5$) unresolved source hosted by a bright ($K_s \simeq 15$) galaxy. We conclude that at the magnitude limit of our images for point-like sources, the errors on the parameters due to the GALFIT detection capabilities are not affecting our results.

4.2.3   The fitting results

The best-fitting parameters (m_{host}, radius[4], $m_{nucleus}$) obtained in each band for MODEL 1 and MODEL 2 are reported in Table 4.2. Since the uncertainties quoted by GALFIT are very small (see Peng et al. 2002), the errors reported in Table 4.2 have been estimated comparing the best-fitting results obtained adopting different stars to model the PSF in the fitting; therefore, the errors quoted in the Table are mainly due to the uncertainties on the PSF shape.

• In two out of the four sources we found clear evidence of a further unresolved component on top of the elliptical galaxy profile. The K_s-band residual images of PKS 03120018 and PKS 03120017, obtained by subtracting the fitted models from the original images, are shown in Fig. 4.6; the residuals obtained with MODEL 1 are shown in the left panels, while those obtained with MODEL 2 in the right panels. Introducing an unresolved component improves the quality of the fit, mostly in the K_s band, as evident from the residual images and the χ^2 in the Table. The excess with respect to the bulge profile in the innermost region increases towards longer wavelengths. The host galaxy parameters obtained with MODEL 2 are cleaned by the nuclear component.

• The fitting procedure found no evidence for a central component in Abell 2690013. The residual images obtained with MODEL 1 in both J and K_s bands show no need for a central unresolved source in the fitting model; the residuals in the K_s band are shown in Fig. 4.7. If a nuclear component is present, its magnitude is fainter than the limits of our observations. The absence of a central unresolved component is also supported by the

---

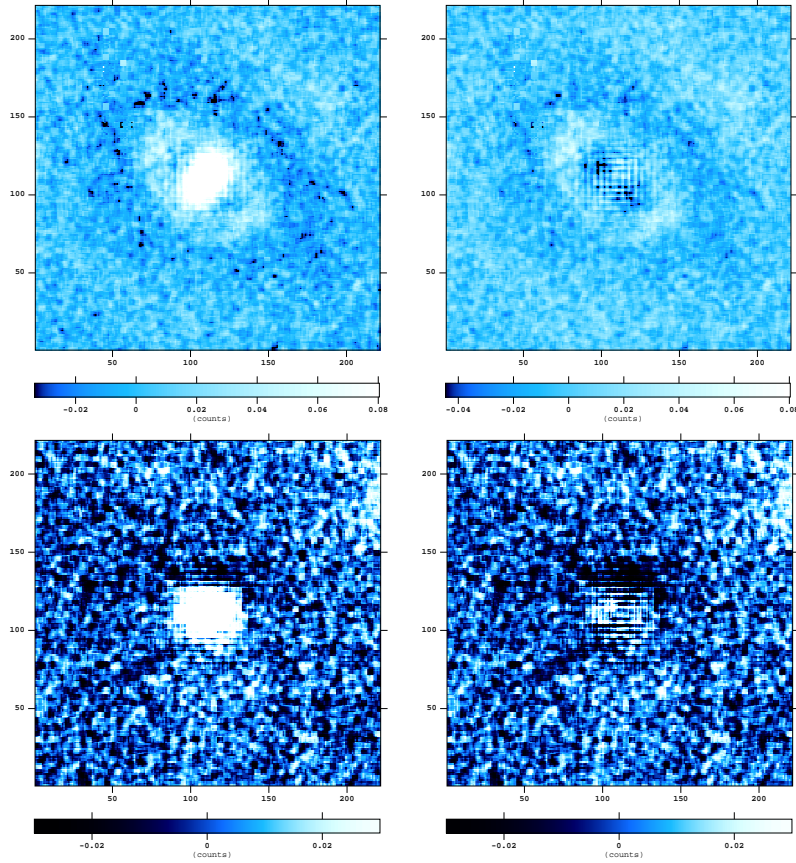[4]The radius reported in Table 4.2 is the effective radius.

Figure 4.6: Residual images (galaxy - model) of PKS 03120018 (top) and PKS 03120017 (bottom) obtained applying a model without (on the left) and with (on the right) a central unresolved component.

X-ray analysis: the X-ray emission is well fitted by a thermal model consistent with the extended appearance, as shown in Figure 4.4.

• Thanks to the high quality of the ISAAC images with sub-arcsec seeing, it has been possible to unveil the complex morphology of source Abell 1835140. It is a close interacting system, composed by two nearby bulges embedded in a common envelope. The angular separation of the two nuclei is ~ 0.9 arcsec. The high X-ray variability (a factor of ~ 7.5 in almost 3 years) could be connect with this morphology. The morphological fitting was performed including simultaneously the two components despite the small angular separation. We fitted a Sersic model for both galaxies: in the J band the fit did not provide a statistically reasonable solution (i.e., by means of χ^2), while in the K_s band we obtained a steep profile for the northern nucleus and a flatter profile for the southern one. Therefore we performed a new fit, adding an unresolved component only to the northern source and a de Vaucouleurs profile to both the bulges, as performed for the other *XBONGs*. The results are suggestive of the presence of a point-like component in the northern source of the double system. Since the fitting does not provide a statistically acceptable description of the two sources, leaving significant residuals because of their low spatial separation, this result should be considered as just
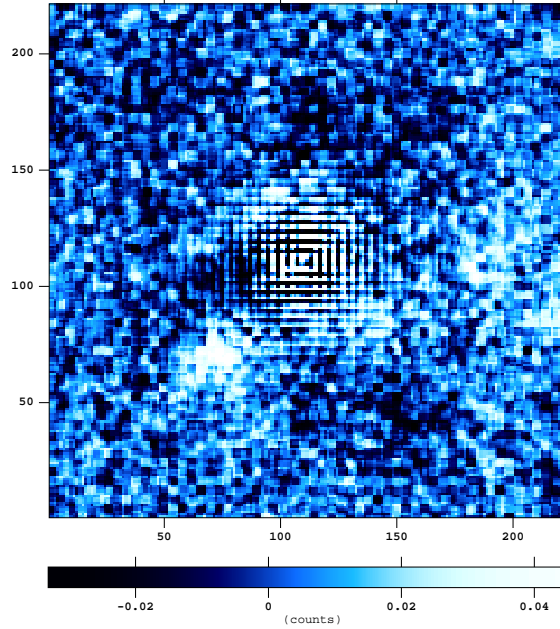
Figure 4.7: Residual image of source Abell2690013 obtained applying MODEL 1.

qualitative. Observations with, e.g., Integral Field Unit (IFU) could provide further clues on the nature and properties of this source.

4.2.4   Near-Infrared color

The surface brightness decomposition technique allowed us to separate the galaxy from the unresolved nuclear contribution in two out of four *XBONGs*. The host galaxy parameters (m_{host}, r_e) and the J–K_s colors are in good agreement with the K_s-band luminosity vs. radius relation (Pahre 1999) and the color typical of elliptical galaxies (Cutri et al. 2000), respectively, lending further support to the morphological analysis.

   The nuclear near-infrared colors of PKS 03120018 (J–K_s=2.21 $\pm$ 0.36) and PKS 03120017 (J–K_s=2.36 $\pm$ 0.37) are reported in Figure 4.8 along with literature data. Red triangles represent the optically selected quasars with near-infrared counterparts in the 2MASS (Barkhouse et al. 2001), while the open black squares are the 2MASS selected red quasars from Hutchings et al. (2003) in a redshift range ($0.1 < z < 0.3$) similar to that of our sources. Even if affected by large uncertainties, mainly due to the extremely faint J-band magnitudes, the J–K_s colors of the two *XBONGs* are consistent with those of 2MASS red quasars at the same redshift. The tracks plotted in Fig. 4.8 represent the color-redshift relations for a composite quasar template from the Large Bright Quasar Survey (Francis et al. 1991) extended to the near-IR using the mean radio-quiet quasar energy distribution (SED) by Elvis et al. 1994 (see also Maiolino et al. 2000). We have included the effect of internal dust attenuation on the LBQS template using a dust screen model and the SMC extinction law (Pei at al. 1992). The curves represent different extinction values
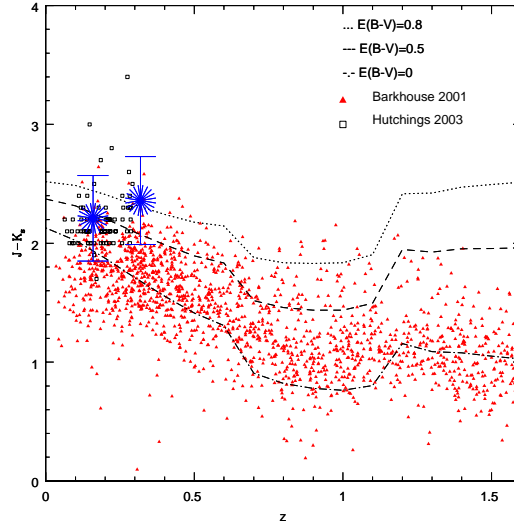
Figure 4.8: Near-infrared color obtained for the AGNs hosted in PKS 03120017 and PKS 03120018 compared with literature data. Red triangles are the optically selected quasars with near-infrared counterparts in the 2MASS (Barkhouse et al. 2001), while the open black squares are the 2MASS selected red quasars from Hutchings et al. (2003). The tracks plotted represent the color-redshift relations for a composite quasar template with different extinction values ($E(B-V)$=0, 0.5, 0.8, from bottom to top).

($E(B-V)$=0, 0.5, 0.8 from bottom to top). At the face value, the best-fit J–K_s color of the nuclei implies $E(B-V) \simeq 0.5 - 0.8$ which corresponds to $N_H \simeq 3 - 5 \times 10^{21}$ cm^{-2} if we use a standard Galactic dust-to-gas ratio[5] as a conversion factor. The comparison of the extinction with the gas absorption obtained from the X-ray analysis will be discussed in section 4.4.

4.3 Simulated optical spectra

In order to check whether the extinction values, estimated from the nuclear near-infrared colors (J–K_s), could explain the lack of the optical emission lines, we compared the observed optical spectra of our *XBONGs* with simulated optical spectra. We adopted the LBQS quasar average spectra extended to the near infrared (see previous section) to reproduce the nuclear component.

The approach we used is as follows:

1. using the IRAF task *deredden*, the quasar template was reddened with different extinction values: $E(B-V)$=0, 0.2, 0.4, 0.6, 0.8;

2. the templates were redshifted to the redshift of the sources using the IRAF task *dopcor*;

---

[5]$E(B-V) = 1.7 \times 10^{-22} \times N_H$ cm^{-2} (Bohlin et al. 1978).

3. the spectra were normalized to the K_s band on the basis of the estimated magnitude for the unresolved central source;

4. the nuclear simulated spectra were summed to the observed *XBONG* optical spectra.

We performed simulated spectra for both sources PKS 03120017 and PKS 03120018. In spite of the good signal-to-noise ratio of the observed spectra, the $[OIII]_{5007\text{\AA}}$ emission line is not visible in all the summed spectra, even in the case without reddening. On the contrary, it is possible to reveal the presence of an emission line at the expected wavelength of the redshifted $H\alpha_{6563\text{\AA}}$ in the spectra with $E(B-V)$=0.

In order to quantify the emission-line detection limits as a function of $E(B-V)$, we measured the equivalent width (EW) of the $H\alpha$ in the simulated spectra. Since the EW is defined as the ratio between the line flux and the continuum flux at the line wavelength, its value does not change applying the extinction in the nuclear simulated spectra. On the contrary, the EW in the total spectra depends from both the nuclear and the steady host galaxy continuum, thus decreasing at growing extinction. Figure 4.9 shows the equivalent width measured in the summed spectra as a function of the $E(B-V)$ along with the 3σ level of detectability (dot-dashed line) for both the sources. The EW detection limit has been estimated following the relation presented in Mignoli et al. 2005:

$$EW(detection\ limit) = \frac{SL * \Delta}{(S/N)_{cont}} \tag{4.2}$$

where Δ is the resolution element (in Å) of our spectra, SL is the significance level of the detectable line, expressed in terms of sigma above the continuum noise, and S/N is the signal-to-noise ratio of the continuum in the total spectra. The extinction values for which the $H\alpha$ equivalent width is lower than the estimated detection limit is $E(B-V) \sim 0.5$, in fair agreement with the values found with the near-infrared morphological analysis. In the next section we will compare all the extinction values found so far.

4.4   Discussion

The surface brightness decomposition technique allowed us to deconvolve the nuclear from the galaxy contribution in two (PKS 03120018 and PKS 03120017) out of the four *XBONGs*.

There is no evidence for the presence of a significant nuclear component in Abell 2690013; the magnitude and the effective radius of the galaxy are in good agreement with the Kormendy relation extended to the K_s band (Pahre 1999). Moreover, the presence of an active nucleus could be also ruled out thanks to a more careful analysis of the X-ray image. The X-ray source is clearly extended (Fig. 4.4) and the X-ray spectrum is well fitted by a thermal model.

The presence of two close (d <0.9 arcsec) galaxies embedded in a common halo with disturbed morphology in source Abell 1835140 prevented us from a detailed analysis
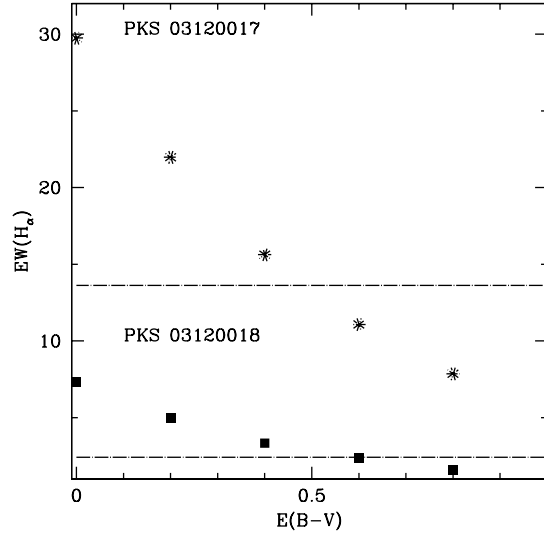
Figure 4.9: The observed equivalent width of the $H\alpha$ line plotted against the $E(B-V)$ of the simulated spectra; stars represent PKS 03120017 and filled squares PKS 03120018. The dot-dashed lines represent the EW detection limit curves as estimated following Mignoli et al. (2005).

with GALFIT. A qualitative analysis reveals the presence of a nuclear component in the northern source of the system, possibly associated with the X-ray emission.

The estimated nuclear J–K_s colors, even affected by large errors due to the uncertainties on the nuclear J-band magnitudes, are consistent, at the face value, with extinction values of $E(B-V)$= 0.5 and 0.8 for PKS 03120018 and PKS 03120017, respectively. For both of them, the lower limit computed with the procedure explained in Section 4.3 is $E(B-V) \sim 0.5$. These values are in agreement with the gas absorption column densities found with the X-ray spectral analysis, assuming a Galactic dust-to-gas ratio (Bohlin et al. 1978).

The SEDs of PKS 03120017 and PKS 03120018 are reported in figure 4.10 and 4.11. Open circles represent the host galaxy and the filled squares the nuclear emission. The X-ray spectra are the same as Figure 4.3, taking into account the errors on the X-ray flux. We note that source PKS 03120017 has been detected at 5 and 8.7 GHz with fluxes of 1.29 and 0.55 mJy, respectively. In the left panels the data are compared with the Type 1 AGN template from Elvis et al. (1994), normalized to match the 5 keV rest-frame luminosity for both sources as well as the 5 GHz rest frame luminosity for PKS 03120017. The X-ray to near-infrared ratio of both sources is consistent with that of a Type 1 AGN. The radio spectral index of source PKS 03120017 is very steep ($\alpha \sim 1.7$), at variance with the value expected for an active nucleus ($\alpha \leqslant 0.5$). However the radio observations are not simultaneous and thus the variability may affect the above estimates.

Whether the observed broad band SEDs are consistent with one or more of the alternative possibilities on the nature of *XBONGs* presented in the Introduction (Section 1.4.3) it is discussed in the following.
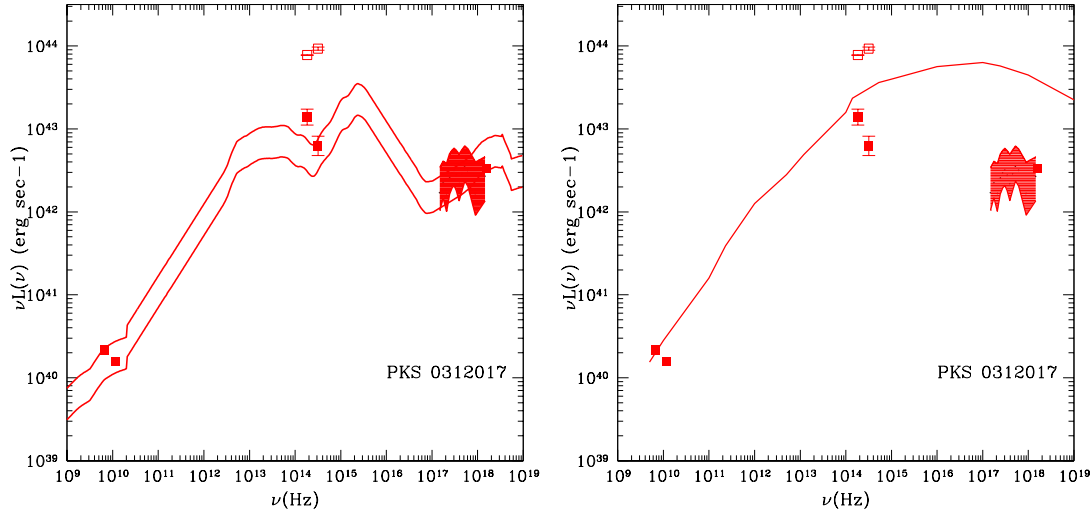
Figure 4.10: The broad-band spectral energy distribution of source PKS 03120017compared with the Type 1 AGN SED (Elvis et al. 1994; left panel) and with a blazar SED with radio luminosity consistent with that of our object (Fossati et al. 1998; right panel). The AGN SED is normalized both to the radio and the X-ray data (rest frame 5 GHz and 5 keV, respectively).

The detection of PKS 03120017 in the radio band suggests (Brusa et al. 2003) that it could be an example of a high-energy-peaked BL Lac (the so called HBL). To shed light on the nature of the broad-band emission of PKS 03120017, we report in Fig. 4.10 (right panel) the SED with the lowest radio luminosity belonging to the "blazar sequence" (Fossati et al. 1998), roughly matching the observed 5 GHz flux density of our source. The X-ray-to-radio luminosity ratio of PKS 03120017 is one order of magnitude lower than that expected for HBL. The HBL SED does not adequately fit the nuclear data of PKS 03120017 suggesting that either the Blazar sequence break down at low luminosities or "more likely" that PKS 03120017 is not a BL Lac object.

The presence of Compton-thick absorption for source PKS 03120018 was favoured by Comastri et al. (2002), on the basis of the comparison of the source SED (including the host galaxy) with that of NGC 6240, the prototype of this class of objects (see their Fig. 5). The near-infrared nuclear fluxes obtained with the present analysis along with a re-analysis of the X-ray spectrum, consistent with Compton-thin obscuration ($N_H \sim 5 \times 10^{21}$ cm^{-2}), make the Compton-thick hypothesis no more tenable (Fig. 4.11, left panel).

A multiwavelength spectral fit to the total emission of source PKS 03120018 with a RIAF plus thin-disk model was presented by Yuan & Narayan (2004). Even if a detailed analysis of ADAF model is beyond the scope of this paper, their model is reported in Fig. 4.11 (right panel). We note that the solution proposed by Yuan & Narayan (2004) does not provide a good fit to the nuclear data; however, given the large number of free parameters in RIAF models, we cannot rule out that inefficient accretion may explain the PKS 03120018 SED.
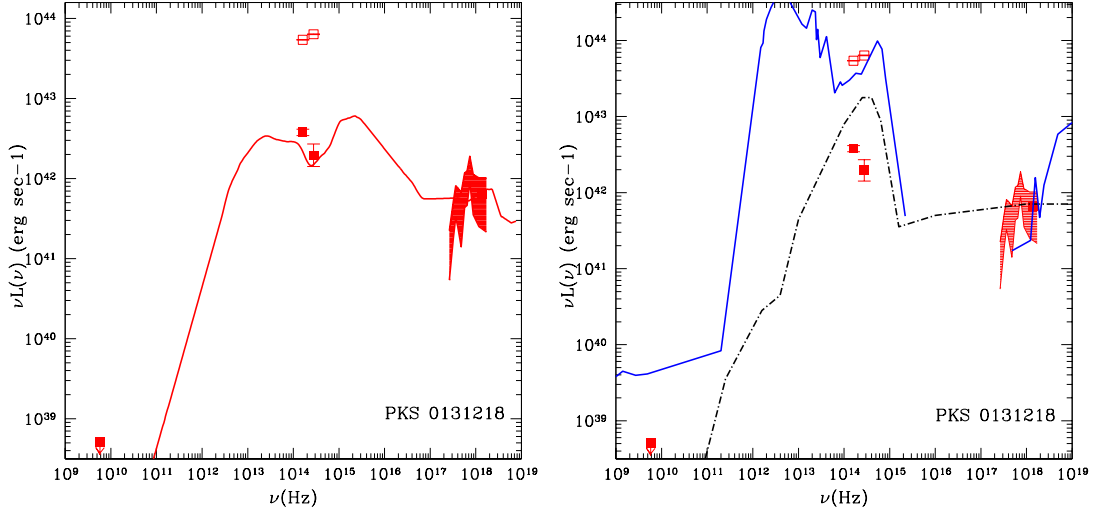
Figure 4.11: The broad-band spectral energy distribution of source PKS 03120018 is compared with the Type 1 AGN SED (Elvis et al. 1994) normalized to the X-ray data (left panel) and with that of the highly obscured Seyfert 2 galaxy NGC 6240 (continuous line) and with the RIAF model (dot-dashed line; Yuan and Narayan 2004; right panel).

To explain the properties of more than half of the *XBONGs* selected in the *Chandra* deep fields at high redshift, Rigby et al. (2006) proposed the presence of extranuclear dust and gas distributed on large scales (i.e., kpc dust lanes). Dust lanes have been observed in HST images of nearby galaxies hosting a Seyfert 2 nucleus (Malkan et al. 1998) and seem also to be ubiquitous in nearby early-type active galaxies, from the Ho et al. (1995) sample, analyzed by Lopes et al. (2007). X-ray observations of galaxies belonging to the Malkan et al. sample suggest a strong correlation between the presence of dust lanes and X-ray absorption (Guainazzi et al. 2001, 2005). In those objects, the presence of extranuclear dust lanes is always associated with optical emission lines at variance with the *XBONG* definition. If dust lanes are responsible of the *XBONG* classification as proposed by Rigby et al. they should be visible in the optical in our sources which are much brighter. We have retrieved from the HST archive two ACS/HRC images of source PKS 03120018 taken in the F475W and F625W filters. The optical images do not show any obvious large-scale dust structure.

Having ruled out heavy nuclear absorption and absorption related to the presence of dust lanes, the lack of optical emission lines in PKS 03120017 and PKS 03120018 requires an alternative explanation. One possibility is that the ionizing flux does not reach the narrow line region either because absorbed by intervening dust and gas, with E(B-V)=0.5 and $N_H \sim 10^{21}$cm^{-2}, covering 4π at the central engine, or simply because the central source is weak and not enough UV photons are produced, or a combination of both.

Having estimated the host galaxy magnitude, it is possible to compute the black hole mass adopting the Marconi & Hunt (2003) relation, safely assuming that it remains
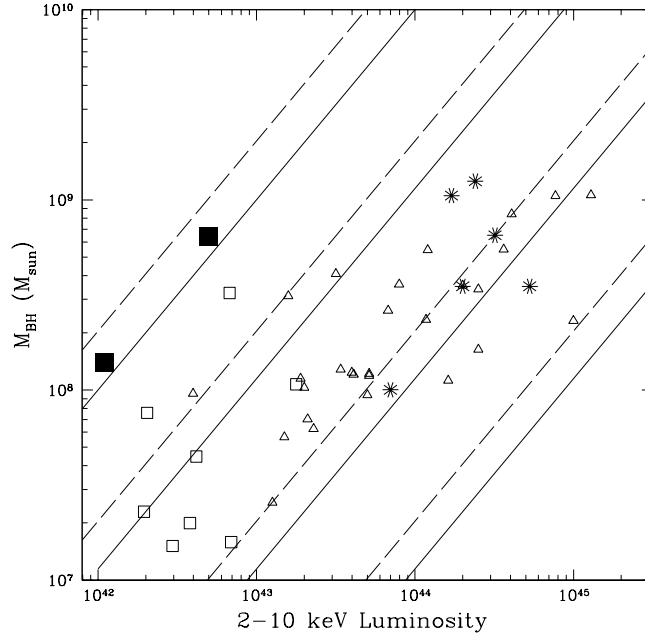
Figure 4.12: Black Hole masses (in units of solar mass) versus the 2-10 keV luminosity. The continuous lines represents the expected correlation between the two plotted quantities for two different assumptions on the bolometric correction ($k_{bol} = 15$ and $k_{bol} = 30$, solid and dashed line, respectively) and L/L$_{Edd}$=1.0-10^{-3}.

constant up to the low redshift of the sources (see the discussion in section 3.7). The rest frame K$_s$-band luminosity has been computed using an evolving elliptical galaxy template (Bruzual & Charlot 2003) to properly account for the K-corrections. The black hole masses obtained are $6.5 \times 10^8 M_\odot$ and $1.4 \times 10^8 M_\odot$ for PKS 03120017 and PKS 03120018, respectively. Assuming a bolometric correction value appropriate for the X-ray luminosity of *XBONG* nuclei $(1 - 5 \times 10^{42}$ erg sec$^{-1})$, it is possible to derive the bolometric luminosity and, therefore, to estimate the Eddington ratio (L_{bol}/L_{Edd}) of the two sources. For a bolometric correction in the range 15-30 (Elvis et al. 1994; Marconi et al. 2004), the resulting Eddington ratio is close to $L_{bol}/L_{Edd} \sim 10^{-3}$.

In Fig. 4.12 the black hole masses as a function of the X-ray luminosity (filled squares) are reported along with literature data. Open triangles are the X-ray emitting EROs from Brusa et al. (2005), starred symbols are the highly obscured quasars at high redshift from Pozzi et al. (2007) and open squares are the low-luminosity AGN (LLAGN) from Panessa et al. (2006). Keeping in mind the uncertainties on our estimates, even if at the same X-ray luminosity, the black holes that reside in our objects are more massive than those of the LLAGN of Panessa et al (2006). The two *XBONGs* appear to be characterized by a rather low Eddington ratio, much lower than in the comparison samples. Thus, the lack of optical emission lines may be explained by an intrinsically weak nucleus that, at this low Eddington ratio, is not able to produce enough UV luminosity to ionize the narrow

line regions.

4.5   Conclusion

We presented a multiwavelength analysis of four *XBONGs*. For these sources, deep near-infrared images taken with ISAAC at VLT, good-quality optical spectra and XMM–*Newton* data are available. Applying the morphological decomposition technique, we were able to detect in two out of the four sources the presence of a nuclear component (PKS 03120017 and PKS 03120018). Source Abell 2690013 presents no nuclear emission and X-ray appearance consistent with an extended source. For source Abell 1835140, the near-infrared images reveal a complex morphology where two sources are embedded in a common envelope. The main issue about the *XBONG* nature is whether they represent a truly distinct class or, rather, they are a mixed bag of sources. Our results point towards the latter hypothesis.

The results regarding the nature of the nuclear *XBONGs* and the lack of optical emission lines can be summarized as follows.

- Source PKS 03120017 and PKS 03120018 are well described by a mildly obscured ($E(B-V) = 0.5-0.8$) optically weak nucleus responsible for the X-ray emission hosted by a bright galaxy ($\mathrm{mag}_{K_s}^{nucl}$–$\mathrm{mag}_{K_s}^{host} \sim 4$).

- The lack of optical emission lines cannot be attributed to observational effects as suggested by several authors, at least as far as the high-signal-to-noise ratio of our spectra are concerned.

- The exotic hypotheses that were proposed to explain the lack of emission lines have been discussed. We can safely discard for the two objects both a Compton-thick scenario and an important blazar contribution. The inefficient accretion could not be completely ruled out, because of the high number of free parameters in the model that can be tuned in order to reproduce the broad band SED of *XBONGs*. Moreover a nuclear source which is not efficient in the production of UV photons would be consistent with the lack of optical emission lines.

- The presence of a thin nuclear gas and dust structure (as argued by Cocchia et al. 2007) covering 4π at the nuclear source, combined with the low level of activity of the BH, could prevent the ionization of the narrow line regions and produce also the extinction we measured.

- Upcoming observations with VLT/VIMOS-IFU (Integral Field Unit) could help in the detection of the typical AGN emission lines down to a very faint flux limit and in the study of the kinematics of the interacting system.

Conclusions

The most important results obtained in this PhD Thesis concern the multiwavelength properties of elusive, obscured hard X-ray selected AGN and of their host galaxies. The attention has been focused on the high X-ray-to-optical flux ratio sources, X-ray emitting extremely-red objects and X-ray bright optically normal galaxies. In order to characterize their broad-band properties, the multiwavelength databases of several deep and large-area surveys have been exploited.

- A high X-ray-to-optical flux ratio (X/O) is often a signature of significant X-ray obscuration or high redshift or both. At the flux limits of the *Chandra* Deep Fields, the high X/O sources are typically characterized by extremely faint optical magnitudes and are therefore challenging targets for optical spectroscopy. In this framework, a detailed investigation of their X-ray properties may provides further clues on the nature of this important component accounting for about 20% of the X-ray background. A sample of 127 X/O sources have been selected in the deep fields.

  - Given the low-counting statistics of most of the sources, a suitable procedure to appropriately extract average spectra and relative response matrices, from observations performed with different aim points and roll-angles, has been developed and tested.

  - The average spectrum of the high X/O sources selected in the deep fields is very flat ($\Gamma \simeq 1$). The measured value is significantly flatter than the average total spectrum of the X-ray sources detected in the *Chandra* deep fields, as well as of the average XRB slope in the 0.5-8 keV range, strongly suggesting that high X/O sources represent the most obscured component of the XRB below 6 keV.

  - To search for a trend of the spectral slope as a function of flux, stacked spectra in different flux intervals have been analyzed. The spectral slope remains constant and very hard over about two decades of X-ray flux (10^{-16}–10^{-14} erg cm^{-2} s^{-1}), definitely flatter than that measured for the entire *CDFN* and *CDFS* samples. The most straightforward explanation of the observed spectral

slope is in terms of superposition of different photoelectric cut-offs due to Compton-thin absorption, most likely spread over a range of redshifts.

– With the aim to quantify the amount of obscuration, we stacked the observed X-ray spectra in relatively narrow redshift bins, using both spectroscopic (20) and photometric (40) redshifts. The results unambiguously confirm that high X/O have rest-frame column densities larger than 10^{22} cm^{-2} at z$\simeq$1 and of the order of 2×10^{23} cm^{-2} at z$\simeq$3.

The main conclusion is that obscuration is ubiquitous among X/O sources; although it is somewhat expected, it has not been previously proven as it requires very good quality X-ray data.

- Originally selected in K-band imaging surveys, extremely red objects (EROs, $R-K >$5) are now identified as the counterparts of hard X-ray sources. In particular, it has been shown that the combined selection of extremely red colors and high X/O is highly efficient in picking up luminous ($> 10^{44}$ erg s^{-1}) and obscured (N$_H >$ 10^{22} cm^{-2}) sources at high redshifts ($z > 0.8$), i.e., Type 2 QSO. The database of the COSMOS survey offers the possibility to characterize the multiwavelength (from infrared to X-rays) properties of a statistically significant sample of more than 100 X-ray emitting EROs (XEROs) in the redshift range $z \approx 0.8 - 2$.

  – There is a strong correlation between red colors and high X/O, in the sense that most of the reddest sources have high X/O ratios. At variance, spectroscopically confirmed BLAGN have lower X/O and blue colors.

  – Based upon the hardness ratio, we have estimated the X-ray absorbing column density, using both spectroscopic and photometric redshift. At the face value, 70% of XEROs are consistent with absorption in excess of 10^{22} cm^{-2}. Moreover, half of the sample (55%) have properties similar to those expected for Type 2 QSO.

  – Thanks to the multiwavelength fitting performed in the optical and infrared bands for a representative subsample of the XEROs population it was possible to deconvolve the nuclear emission from that associated to the host galaxy. We can argue that the red colors of the majority (70%) of the sources can be explained by the host galaxy stellar emission significantly contributing to the total continuum, while the AGN emission is most likely blocked by the obscuring screen of gas and dust. Moving towards longer wavelengths, the host galaxy contribution slowly decreases, favouring the arising of the nuclear light, reprocessed in the infrared band by the torus postulated in the AGN Unified Model.

  – A comparison between the effective hydrogen column densities and the nuclear optical extinction reveals that there is no correlation between the two quantities,

but rather the $E(B-V)/N_H$ ratio is always lower than the Galactic one. A possible explanation for this discrepancy ma be ascribed to the presence of dust grains in the circumnuclear region of AGNs larger than those in the diffuse interstellar medium of our Galaxy.

– Thanks to the independent estimates of the galaxy and nuclear light, the masses of the central BHs have been estimated using the M_{BH}-L_K relation. Under the hypothesis of no evolution with redshift for this relation, our XEROs have masses in the range $\sim 4 \times 10^7$–3×10^9 $M_\odot$ and are characterized by Eddington ratios in the range $\lambda = 0.08 - 1$ (with a median value of ≈ 0.16 if a X-ray bolometric correction of 30 is assumed), consistent with a scenario in which XEROs are obscured quasars emitting at relatively high Eddington ratio.

- X-ray bright optically normal galaxies are characterized by the lack of evident AGN signatures in high-quality spectra, although X-ray observations provide indications for the presence of moderately luminous ($L_X = 10^{42} - 10^{43}$ erg s^{-1}), not necessarily obscured AGN. Even though several interpretations have been proposed to explain the observed properties of *XBONGs*, their nature is still matter of debate. In the hypothesis that an active nucleus is powering *XBONG*, we searched for its emission in the near-infrared by applying to deep ISAAC/VLT images a 2-dimensional modeling technique (GALFIT).

On an admittedly small sample of sources (4 *XBONGs* from the HELLAS2XMM survey), we were able to detect the presence of a putative nucleus responsible for the X-ray emission in 2 out of 4 sources.

– The two nuclear *XBONGs* (PKS 03120017 and PKS 03120018) are characterized by the presence of a bright bulge-dominated galaxy and a faint nuclear component moderately obscured, both in terms of X-ray obscuration ($N_H \approx 10^{21}$ cm^{-2}) and optical extinction ($E(B-V)$=0.5–0.8).

– Among the several hypotheses proposed in the literature to explain the nature of *XBONGs* we were able, on the basis of the broad-band properties of the two nuclear sources, to rule out Compton-thick absorption and blazar contribution.

– We argue that the presence of a thin nuclear gas and dust structure fully covering (4π) the nuclear source, combined with a low level of activity of the massive BHs ($M_{BH} \simeq 1.4 \times 10^8 - 6.5 \times 10^8$ $M_\odot$), could prevent the ionization of the narrow line regions and produce also the extinction we measured. Alternatively, a weak nucleus inefficient in the UV-photons production would be consistent with the lack of optical emission lines.

– There is no evidence of a nuclear component in the source Abell 2690013; this is supported by the extended appearance in the X-ray band and by the X-ray

emission well fitted by a thermal model.

– The presence of two close nuclei (d <0.9 arcsec) in source Abell 1835140 embedded in a common envelope, revealed thanks the deep near-infrared images, prevents us from performing a detailed decomposition analysis. A qualitative analysis revealed the possible presence of a nuclear component in one of the two sources, possibly associated to the variability of the X-ray emission.

Future Perspectives

This thesis has been successful in studying the multiwavelength properties of elusive sources. However, the work to understand these objects has only just begun. For what concern obscured hard X-ray sources (X/O and XEROs), their infrared, especially at $24\mu m$, and radio properties will be investigated in more detail. Further clues on the host galaxies of these objects, will be provided by a more detailed morphological analysis combined with the results obtained with the SED deconvolution approach. Upcoming deep near-infrared spectroscopic observations (MOIRCS) for a subsample of XEROs will provide a complete redshift coverage and will allow us to study more distant objects and, in turn, to obtain a more detailed picture of the galaxy-AGN relation in the obscured phase.

 In the COSMOS survey, a larger sample of *XBONGs* will be collected and the radio to X-ray properties will be investigated on a statistically meaningful sample of *XBONGs* thus making possible to better test the nature of this population. The analysis of VLT/VIMOS-IFU (Integral Field Unit) observations obtained for the *XBONG* sample discussed above will allow to search for extremely faint AGN emission lines and to study the gas kinematics.

Related Publications

Refereed Papers:

- Comastri, A., Brusa, M., **Civano, F.**,
  A broad iron Kalpha line at z= 1.146
  2004, MNRAS 351, L9

- **Civano, F.**, Comastri, A., Brusa, M.,
  X–ray spectral analysis of optically faint sources in the *Chandra* Deep Fields,
  2005, MNRAS 358, 693

- Brusa, M., Zamorani, G., Comastri, A., Hasinger, G., Cappelluti, N., **Civano, F.**, Finoguenov, A., Mainieri, V., Salvato, M., Vignali, C., Elvis, M., Fiore, F., Gilli, R., Impey, C.D., Lilly, S.J., Mignoli, M., Silverman, J., Trump, J., Urry, C.M., Bender, R., Capak, P., Huchra, J.P., Kneib, J.P., Koekemoer, A., Lehmann, I., Matute, I., McCarthy, P.J., McCracken, H.J., Scoville, N.Z., Taniguchi, Y., Thompson, D.,
  The XMM–Newton wide–field survey in the COSMOS field III: optical identification and multiwavelenght properties of a large sample of X–ray selected sources,
  2007, accepted by ApJS for the COSMOS special issue, astro–ph/0612358

- Mainieri, V., Hasinger, G., Cappelluti, N., Brusa, M., Brunner, H., **Civano, F.**, Comastri, A., Elvis, M., Finoguenov, A., Fiore, F., Gilli, R., Lehmann, I., Silverman, J., Tasca, L., Vignali, C., Zamorani, G., Schinnerer, E., Impey, C.D., Trump, J., Lilly, S.J., Maier, C., Griffiths, R.E., Miyaji, T., Capak, P., Koekemoer, A., Scoville, N.Z., Shopbell, P., Taniguchi, Y.,
  The XMM–Newton wide–field survey in the COSMOS field IV: X–ray spectral properties of Active Galactic Nuclei,
  2007, accepted by ApJS for the COSMOS special issue, astro–ph/0612361

- Rodighiero, G., Guppioni, C., **Civano, F.**, Comastri, A., Franceschini, A., Mignoli, M., Fritz, J., Vignali, C., Treu, T.,
  Hidden activity in high redshift spheroidal galaxies from mid–infrared and X–ray observations in the GOODS north field,
  2007, accepted by MNRAS, astro-ph/0701178

- Cappelluti, N., Hasinger, G., Brusa, M., Comastri, A., Zamorani, G., Bohringer, H., Brunner, H., **Civano, F.**, Finoguenov, A., Fiore, F., Gilli, R., Griffiths, R.E., Mainieri, V., Matute, I., Miyaji, T., Silverman, J.,
  The XMM–Newton wide–field survey in the COSMOS field II: X–ray data and the logN–logS,
  2007, to appear in the ApJS for the COSMOS special issue, astro-ph/0701196

- Pozzi, F., Vignali, C., Comastri, A., Pozzetti, L., Mignoli, M., Gruppioni, C., Zamorani, G., Lari, C., **Civano, F.**, Brusa, M., Fiore, F., Maiolino, R., La Franca, F.
  The HELLAS2XMM survey X. The bolometric output of luminous obscured quasars: the Spitzer perspective
  2007, submitted to A&A

- **Civano, F.**, Mignoli, M., Comastri, A., Vignali, C., et al.
  The HELLAS2XMM survey:XI. Unveiling the nature of XBONGs,
  2007, submitted to A&A

Unrefereed papers (Conference Proceedings):

- **Civano, F.**, Comastri, A., Brusa, M.,
  Extremely faint hard X–ray sources in the Chandra Deep Fields
  2004, 6th Italian Conference on AGNs (Volterra, Italy), on–line pubblication http://www.arcetri.astro.it/agn6

- Comastri, A., Fiore, F., Vignali, C., Brusa, M., **Civano, F.**,
  Obscured accreting black holes at high redshift
  2005, Proceedings of the Conference "Growing Black Holes" held in Garching, Germany, June 21-25, 2004, edited by A. Merloni, S. Nayakshin and R. Sunyaev, Springer-Verlag series of "ESO Astrophysics Symposia"

- **Civano, F.**, Comastri, A., Mignoli, M., Vignali, C., Fiore, F. , Cocchia, F.,
  Unveiling the active nucleus of XBONGs
  2005, Proceedings of the Conference "The X–ray Universe", held in El Escorial, Spain, September 2005, ESA publication

- **Civano, F.** on behalf of the XMM–COSMOS TEAM,
  Obscured QSOs in the COSMOS survey
  2006, 7th Italian Conference on AGNs (Montagnana (PD), Italy) on–line pubblication http://web.pd.astro.it/agn7/

- Brusa, M., **Civano, F.**, Comastri, A., Gilli, R.,
  The power of stacking X–ray spectroscopy in deep Chandra Fields
  2007, Proceedings of the Conference "At the Edge of the Universe: latest results from the deepest astronomical surveys", held in Sintra, Portugal, October 2006, ASP Conference Series

Bibliography

Akiyama, M., et al. 2000, ApJ, 532, 700

Alexander, D. M., Brandt, W. N., Hornschemeier, A. E., Garmire, G. P., Schneider, D. P., Bauer, F. E., & Griffiths, R. E. 2001, AJ, 122, 2156

Alexander, D. M., Vignali, C., Bauer, F. E., Brandt, W. N., Hornschemeier, A. E., Garmire, G. P., & Schneider, D. P. 2002, AJ, 123, 1149

Alexander, D. M., et al. 2003, AJ, 126, 539

Antonucci, R. 1993, ARA&A, 31, 473

Arnaud, K. A. 1996, ASP Conf. Ser. 101: Astronomical Data Analysis Software and Systems V, 101, 17

Baldi, A., Molendi, S., Comastri, A., Fiore, F., Matt, G., & Vignali, C. 2002, ApJ, 564, 190

Barger, A. J., et al. 2003, AJ, 126, 632

Barger, A. J., Cowie, L. L., Mushotzky, R. F., Yang, Y., Wang, W.-H., Steffen, A. T., & Capak, P. 2005, AJ, 129, 578

Barkhouse, W. A., & Hall, P. B. 2001, AJ, 122, 496

Barmby, P., et al. 2006, ApJ, 642, 126

Bauer, F. E., Alexander, D. M., Brandt, W. N., Schneider, D. P., Treister, E., Hornschemeier, A. E., & Garmire, G. P. 2004, AJ, 128, 2048

Bauer, F. E., et al. 2004, Advances in Space Research, 34, 2555

Benítez, N. 2000, ApJ, 536, 571

Bohlin, R. C., Savage, B. D., & Drake, J. F. 1978, ApJ, 224, 132

Bolzonella, M., Miralles, J.-M., & Pelló, R. 2000, A&A, 363, 476

Brandt, W. N., & Hasinger, G. 2005, ARA&A, 43, 827

Brusa, M., et al. 2003, A&A, 409, 65

Brusa, M. 2004, ArXiv Astrophysics e-prints, arXiv:astro-ph/0406435

Brusa, M., et al. 2005, A&A, 432, 69

Brusa, M., et al. 2007, ApJS in press, astro-ph/0612358

Bruzual A., G., & Charlot, S. 1993, ApJ, 405, 538

Bruzual, G., & Charlot, S. 2003, MNRAS, 344, 1000

Caccianiga, A., et al. 2004, A&A, 416, 901

Capak, P. L., et al. 2007, ApJS in press

Cappelluti, N., et al. 2007, ApJS in press, astro-ph/0701196

Cash, W. 1979, ApJ, 228, 939

Ciliegi, P., Zamorani, G., Hasinger, G., Lehmann, I., Szokoly, G., & Wilson, G. 2003, A&A, 398, 901

Cimatti, A., et al. 2002, A&A, 381, L68

Civano, F., Comastri, A., & Brusa, M. 2005, MNRAS, 358, 693

Cocchia, F., et al. 2007, A&A in press, astro-ph/0612023

Comastri, A., Setti, G., Zamorani, G., & Hasinger, G. 1995, A&A, 296, 1

Comastri, A., Fiore, F., Vignali, C., Matt, G., Perola, G. C., & La Franca, F. 2001, MNRAS, 327, 781

Comastri, A., et al. 2002a, ApJ, 571, 771

Comastri, A., Vignali, C., Brusa, M., The Hellas, & Hellas2XMM Consortia 2002b, ASP Conf. Ser. 284: IAU Colloq. 184: AGN Surveys, 284, 235

Comastri, A., Brusa, M., Mignoli, M., & the HELLAS2XMM team 2003, Astronomische Nachrichten, 324, 28

Comastri, A., Brusa, M., & Civano, F. 2004, MNRAS, 351, L9

Comastri, A., & Fiore, F. 2004, Ap&SS, 294, 63

Cutri, R. M., Nelson, B. O., Huchra, J. P., & Smith, P. S. 2000, Bulletin of the American Astronomical Society, 32, 1520

De Luca, A., & Molendi, S. 2004, A&A, 419, 837

de Vaucouleurs, G. 1948, Annales d'Astrophysique, 11, 247

Devriendt, J. E. G., Guiderdoni, B., & Sadat, R. 1999, A&A, 350, 381

Dewangan, G. C., Griffiths, R. E., & Schurch, N. J. 2003, ApJ, 592, 52

Di Matteo, T., Springel, V., & Hernquist, L. 2005, Nature, 433, 604

Elston, R., Rieke, G. H., & Rieke, M. J. 1988, ApJ, 331, L77

Elvis, M., Schreier, E. J., Tonry, J., Davis, M., & Huchra, J. P. 1981, ApJ, 246, 20

Elvis, M., et al. 1994, ApJS, 95, 1

Fabian, A. C., et al. 2002, MNRAS, 335, L1

Ferrarese, L., & Merritt, D. 2000, ApJ, 539, L9

Fiore, F., et al. 2000, New Astronomy, 5, 143

Fiore, F., et al. 2003, A&A, 409, 79

Fiore, F. 2004, Multiwavelength AGN Surveys, 11

Fossati, G., Maraschi, L., Celotti, A., Comastri, A., & Ghisellini, G. 1998, MNRAS, 299, 433

Francis, P. J., Hewett, P. C., Foltz, C. B., Chaffee, F. H., Weymann, R. J., & Morris, S. L. 1991, ApJ, 373, 465

Frank, S., Osmer, P. S., & Mathur, S. 2006, astro-ph/0612352

Fukada, Y., Hayakawa, S., Kasahara, I., Makino, F., Tanaka, Y., & Sreekantan, B. V. 1975, Nature, 254, 398

Gandhi, P., Crawford, C. S., Fabian, A. C., & Johnstone, R. M. 2004, MNRAS, 348, 529

Gebhardt, K., Bender, R., Bower, G., et al. 2000, ApJ, 539, L13

Gendreau, K. C., et al. 1995, PASJ, 47, L5

Georgakakis, A. E., Georgantopoulos, I., & Akylas, A. 2006, MNRAS, 366, 171

Georgantopoulos, I., Stewart, G. C., Shanks, T., Boyle, B. J., & Griffiths, R. E. 1996, MNRAS, 280, 276

Georgantopoulos, I., & Georgakakis, A. 2005, MNRAS, 358, 131

Georgantopoulos, I., Georgakakis, A., & Akylas, A. 2006, ArXiv Astrophysics e-prints, arXiv:astro-ph/0610828

Gezari, S., et al. 2006, ApJ, 653, L25

Giacconi, R., Gursky, H., Paolini, F.R., Rossi, B.B. 1962, Phys.Rev.Lett., 9, 439

Giacconi, R., et al. 2001, ApJ, 551, 624

Giacconi, R., et al. 2002, ApJS, 139, 369

Gilli, R., Salvati, M., & Hasinger, G. 2001, A&A, 366, 407

Gilli, R., Comastri, A., & Hasinger, G. 2007, A&A, 463, 79

Gruber, D.E. 1992, In: Barcons X., Fabian, A.C., (eds.) The Proceedings of : The X-ray background. Cambridge Univ. Press, Cambridge, p. 44

Gruber, D. E., Matteson, J. L., Peterson, L. E., & Jung, G. V. 1999, ApJ, 520, 124

Guainazzi, M., Fiore, F., Matt, G., & Perola, G. C. 2001, MNRAS, 327, 323

Guainazzi, M., Matt, G., & Perola, G. C. 2005, A&A, 444, 119

Hasinger, G., Burg, R., Giacconi, R., Schmidt, M., Trumper, J., & Zamorani, G. 1998, A&A, 329, 482

Hasinger, G., et al. 2001, A&A, 365, L45

Hasinger, G., et al. 2007, ApJS in press, astro-ph/0612311

Hatziminaoglou, E., et al. 2005, AJ, 129, 1198

Hickox, R. C., & Markevitch, M. 2006, ApJ, 645, 95

Ho, L. C., Filippenko, A. V., & Sargent, W. L. 1995, ApJS, 98, 477

Hopkins, P. F., Hernquist, L., Cox, T. J., Di Matteo, T., Robertson, B., & Springel, V. 2006, ApJS, 163, 1

Hornschemeier, A. E., Bauer, F. E., Alexander, D. M., Brandt, W. N., Sargent, W. L. W., Vignali, C., Garmire, G. P., & Schneider, D. P. 2003, Astronomische Nachrichten, 324, 12

Hutchings, J. B., Maddox, N., Cutri, R. M., & Nelson, B. O. 2003, AJ, 126, 63

Impey, C., et al. 2007, ApJS in press

Jahnke, K., Kuhlbrodt, B., & Wisotzki, L. 2004, MNRAS, 352, 399

Jiménez-Bailón, E., Santos-Lleó, M., Piconcelli, E., Matt, G., Guainazzi, M., & Rodríguez-Pascual, P. 2007, A&A, 461, 917

Kinzer, R. L., Jung, G. V., Gruber, D. E., Matteson, J. L., & Peterson, L. E. 1997, ApJ, 475, 361

Koekemoer, A. M., et al. 2004, ApJ, 600, L123

Koekemoer, A. M., et al. 2007, ApJS in press, astro-ph/0703095

Komossa, S., Halpern, J., Schartel, N., Hasinger, G., Santos-Lleo, M., & Predehl, P. 2004, ApJ, 603, L17

Kormendy, J. & Richstone, D. 1995, ARA&A, 33, 581

Kormendy, J. & Gebhardt, K. 2001, in AIP Conf. Proc. 586: 20th Texas Symposium on Relativistic Astrophysics, 363

Kushino, A., Ishisaki, Y., Morita, U., Yamasaki, N. Y., Ishida, M., Ohashi, T., & Ueda, Y. 2002, PASJ, 54, 327

Lacy, M., et al. 2004, ApJS, 154, 166

La Franca, F., et al. 2005, ApJ, 635, 864

Leauthaud, A., et al. 2007, ApJS in press, astro-ph/0702359

Lehmann, I., et al. 2001, A&A, 371, 833

Lilly, S. J., et al. 2006, ApJS in press, astro-ph/0612291

Simões Lopes, R. D., Storchi-Bergmann, T., de Fátima Saraiva, M., & Martini, P. 2007, ApJ, 655, 718

Lumb, D. H., Warwick, R. S., Page, M., & De Luca, A. 2002, A&A, 389, 93

Maccacaro, T., Gioia, I. M., Wolter, A., Zamorani, G., & Stocke, J. T. 1988, ApJ, 326, 680

Madau, P., Ghisellini, G., & Fabian, A. C. 1994, MNRAS, 270, L17

Magorrian, J. et al. 1998, AJ, 115, 2285

Mainieri, V., Bergeron, J., Hasinger, G., Lehmann, I., Rosati, P., Schmidt, M., Szokoly, G., & Della Ceca, R. 2002, A&A, 393, 425

Mainieri, V., et al. 2005, A&A, 437, 805

Mainieri, V., et al. 2007, ApJS in press, astro-ph/0612361

Maiolino, R., Salvati, M., Antonelli, L.A., et al., 2000, A&A, 335, L47

Maiolino, R., Marconi, A., Salvati, M., Risaliti, G., Severgnini, P., Oliva, E., La Franca, F., & Vanzi, L. 2001a, A&A, 365, 28

Maiolino, R., Marconi, A., & Oliva, E. 2001b, A&A, 365, 37

Maiolino, R., et al. 2006, A&A, 445, 457

Malkan, M. A., Gorjian, V., & Tam, R. 1998, ApJS, 117, 25

Marconi, A., & Hunt, L.K. 2003, ApJ, 589, L21

Marconi, A., Risaliti, G., Gilli, R., Hunt, L. K., Maiolino, R., & Salvati, M. 2004, MNRAS, 351, 169

Marshall, F. E., Boldt, E. A., Holt, S. S., Miller, R. B., Mushotzky, R. F., Rose, L. A., Rothschild, R. E., & Serlemitsos, P. J. 1980, ApJ, 235, 4

Mather, J. C., et al. 1990, ApJ, 354, L37

Mc Cracken, E., et al. 2007, ApJS in press

McLure, R. J., & Dunlop, J. S. 2002, MNRAS, 331, 795

Menci, N., Fiore, F., Perola, G. C., & Cavaliere, A. 2004, ApJ, 606, 58

Menci, N., Fontana, A., Giallongo, E., Grazian, A., & Salimbeni, S. 2006, ApJ, 647, 753

Mignoli, M., et al. 2004, A&A, 418, 827

Mignoli, M., et al. 2005, A&A, 437, 883

Miniutti, G., Ballantyne, D. R., Allen, S. W., Fabian, A. C., & Ross, R. R. 2006, MNRAS, 371, 283

Miniutti, G., Ponti, G., Dadina, M., Cappi, M., & Malaguti, G. 2007, MNRAS, 375, 227

Moran, E. C., Filippenko, A. V., & Chornock, R. 2002, ApJ, 579, L71

Moretti, A., Campana, S., Lazzati, D., & Tagliaferri, G. 2003, ApJ, 588, 696

Mushotzky, R. F., Cowie, L. L., Barger, A. J., & Arnaud, K. A. 2000, Nature, 404, 459

Nandra, K., et al. 2005, MNRAS, 356, 568

Nandra, K., & Pounds, K. A. 1994, MNRAS, 268, 405

Norman, C., et al. 2002, ApJ, 571, 218

Padovani, P., Allen, M. G., Rosati, P., & Walton, N. A. 2004, A&A, 424, 545

Pahre, M. A. 1999, ApJS, 124, 127

Panessa, F., Bassani, L., Cappi, M., Dadina, M., Barcons, X., Carrera, F. J., Ho, L. C., & Iwasawa, K. 2006, A&A, 455, 173

Pei, Y. C. 1992, ApJ, 395, 130

Peng, C. Y., Ho, L. C., Impey, C. D., & Rix, H.-W. 2002, AJ, 124, 266

Peng, C. Y., Impey, C. D., Rix, H.-W., Kochanek, C. S., Keeton, C. R., Falco, E. E., Lehár, J., & McLeod, B. A. 2006, ApJ, 649, 616

Perola, G. C., et al. 2004, A&A, 421, 491

Pierre, M., et al. 2001, A&A, 372, L45

Pozzi, F., et al. 2007, A&A in press

Prevot, M. L., Lequeux, J., Prevot, L., Maurice, E., & Rocca-Volmerange, B. 1984, A&A, 132, 389

Richards, E. A. 2000, ApJ, 533, 611

Richards, G. T., et al. 2006, ApJS, 166, 470

Richstone, D. et al. 1998, Nature, 395, A14

Rigby, J. R., Rieke, G. H., Donley, J. L., Alonso-Herrero, A., & Pérez-González, P. G. 2006, ApJ, 645, 115

Reeves, J. N., et al. 2001, A&A, 365, L116

Revnivtsev, M., Gilfanov, M., Sunyaev, R., Jahoda, K., & Markwardt, C. 2003, A&A, 411, 329

Revnivtsev, M., et al. 2005, A&A, 2005, 444, 381

Rosati, P., et al. 2002, ApJ, 566, 667

Sánchez, S. F., et al. 2004, ApJ, 614, 586

Sanders, D.B., et al. 2007, ApJS in press

Scoville, N. Z., et al. 2007, ApJS in press

Sersic, J. L. 1968, Cordoba, Argentina: Observatorio Astronomico, 1968,

Setti, G., & Woltjer, L. 1989, A&A, 224, L21

Severgnini, P., et al. 2003, A&A, 406, 483

Severgnini, P., et al. 2005, A&A, 431, 87

Severgnini, P., et al. 2006, A&A, 451, 859

Shields, G. A., Salviander, S., & Bonning, E. W. 2006, New Astronomy Review, 50, 809

Stark, A. A., Gammie, C. F., Wilson, R. W., Bally, J., Linke, R. A., Heiles, C., & Hurwitz, M. 1992, ApJS, 79, 77

Stern, D., et al. 2002, ApJ, 568, 71

Stern, D., et al. 2005, ApJ, 631, 163

Stevens, J. A., Page, M. J., Ivison, R. J., Smail, I., Lehmann, I., Hasinger, G., & Szokoly, G. 2003, MNRAS, 342, 249

Sutherland, W., & Saunders, W. 1992, MNRAS, 259, 413

Szokoly, G. P., et al. 2004, ApJS, 155, 271

Tanaka, Y., et al. 1995, Nature, 375, 659

Tozzi, P., et al. 2001, ApJ, 562, 42

Treister, E., et al. 2004, ApJ, 616, 123

Tremaine, S., et al. 2002, ApJ, 574, 740

Trump, J. R., et al. 2007, ApJS in press, astro-ph/0606016

Turner, T. J., et al. 2002, ApJ, 574, L123

Vanzella, E., et al. 2004, A&A, 423, 761

Vecchi, A., Molendi, S., Guainazzi, M., Fiore, F., & Parmar, A. N. 1999, A&A, 349, L73

Vestergaard, M. 2002, ApJ, 571, 733

Vestergaard, M., & Peterson, B. M. 2006, ApJ, 641, 689

Vignali, C., Comastri, A., Cappi, M., Palumbo, G. G. C., Matsuoka, M., & Kubo, H. 1999, ApJ, 516, 582

Vignali, C., Brandt, W. N., Schneider, D. P., Garmire, G. P., & Kaspi, S. 2003, AJ, 125, 418

Vignali, C., Alexander, D. M., & Comastri, A. 2006, MNRAS, 373, 321

Vikhlinin, A., Markevitch, M., Murray, S. S., Jones, C., Forman, W., & Van Speybroeck, L. 2005, ApJ, 628, 655

Warwick, R. S., & Roberts, T. P. 1998, Astronomische Nachrichten, 319, 59

Watanabe, K., Hartmann, D. H., Leising, M. D., The, L.-S., Share, G. H., & Kinzer, R. L. 1997, AIP Conf. Proc. 410: Proceedings of the Fourth Compton Symposium, 410, 1223

Williams, R. E., et al. 1996, AJ, 112, 1335

Willott, C. J., et al. 2003, MNRAS, 339, 397

Wolf, C., et al. 2004, A&A, 421, 913

Woo, J.-H., Treu, T., Malkan, M. A., & Blandford, R. D. 2006, ApJ, 645, 900

Worsley, M. A., Fabian, A. C., Barcons, X., Mateos, S., Hasinger, G., & Brunner, H. 2004, MNRAS, 352, L28

Worsley, M. A., et al. 2005, MNRAS, 357, 1281

Yuan, F., & Narayan, R. 2004, ApJ, 612, 724

Zheng, W., et al. 2004, ApJS, 155, 73

Zombeck, M. V. 1990, Cambridge: University Press, 1990, 2nd ed.,